Three-dimensional general relativistic radiation magnetohydrodynamical simulation of super-Eddington accretion, using a new code HARMRAD with M1 closure

Mon. Not. R. Astron. Soc. **000**, 1–36 (2013) Printed 24 December 2013 (MN LATEX style file v2.2)

Three-Dimensional General Relativistic Radiation Magnetohydrodynamical Simulation of Super-Eddington Accretion, using a new code HARMRAD with M1 Closure

Jonathan C. McKinney[1⋆], Alexander Tchekhovskoy[2], Aleksander Sadowski[3], Ramesh Narayan[3]
[1]*University of Maryland at College Park, Dept. of Physics, Joint Space-Science Institute, 1117 John S. Toll Building #082, College Park, MD 20742, USA*
[2]*Astronomy Department and Theoretical Astrophysics Center, University of California, Berkeley, 601 Campbell Hall, Berkeley, CA 94720, USA; Einstein Fellow*
[3]*Harvard-Smithsonian Center for Astrophysics, 60 Garden St., Cambridge, MA 02134, USA*

Accepted 2014. Received 2013; in original form 2013.

ABSTRACT

Black hole (BH) accretion flows and jets are dynamic hot relativistic magnetized plasma flows whose radiative opacity can significantly affect flow structure and behavior. We describe a numerical scheme, tests, and an astrophysically relevant application using the M1 radiation closure within a new three-dimensional (3D) general relativistic (GR) radiation (R) magnetohydrodynamics (MHD) massively parallel code called HARMRAD. Our 3D GRRMHD simulation of super-Eddington accretion (about 20 times Eddington) onto a rapidly rotating BH (dimensionless spin $j = 0.9375$) shows sustained non-axisymmemtric disk turbulence, a persistent electromagnetic jet driven by the Blandford-Znajek effect, and a total radiative output consistently near the Eddington rate. The total accretion efficiency is of order 20%, the large-scale electromagnetic jet efficiency is of order 10%, and the total radiative efficiency that reaches large distances remains low at only order 1%. However, the radiation jet and the electromagnetic jet both emerge from a geometrically beamed polar region, with super-Eddington isotropic equivalent luminosities. Such simulations with HARMRAD can enlighten the role of BH spin vs. disks in launching jets, help determine the origin of spectral and temporal states in x-ray binaries, help understand how tidal disruption events (TDEs) work, provide an accurate horizon-scale flow structure for M87 and other active galactic nuclei (AGN), and isolate whether AGN feedback is driven by radiation or by an electromagnetic, thermal, or kinetic wind/jet. For example, the low radiative efficiency and weak BH spin-down rate from our simulation suggest that BH growth over cosmological times to billions of solar masses by redshifts of $z \sim 6$–8 is achievable even with rapidly rotating BHs and ten solar mass BH seeds.

Key words: accretion, accretion discs, black hole physics, hydrodynamics, (magnetohydrodynamics) MHD, methods: numerical, gravitation

1 INTRODUCTION

Modern black hole (BH) accretion theory has identified radiative cooling and transport as having a significant effect on accretion disk states and temporal behaviors. Without radiation, equations like the test field limit of the general relativistic (GR) magnetohydrodynamic (MHD) equations can be solved to obtain a single solution that applies to arbitrary black hole mass M and mass accretion rate $\dot{M}_0$ because only two physical constants, the speed of light c and gravitational constant (times mass) GM, appear independently. Introduction of a radiative scale via the electron scattering Thomson cross section σ_T (giving scattering opacity $\kappa_{\rm es} = \sigma_{\rm T}/m_p$, with Planck's constant per electron mass, $\hbar/m_e$ and proton mass m_p) and radiation constant ($a_{\rm rad}$, with $\hbar$ appearing alone) forces $\dot{M}_0$ and M to be specific physical values. Then, a useful scale that measures the importance of radiative effects in accretion disks is the Eddington luminosity, as due to a radial balance between a radiative force $F_{\rm rad} = L\sigma_T/(4\pi cr^2)$ and gravity $F_{\rm grav} \approx GMm_p/r^2$ for radiative luminosity L, radius r. The Eddington luminosity is given by

$$L_{\rm Edd} = \frac{4\pi GMc}{\kappa_{\rm es}} \approx 1.3\times10^{46}\frac{M}{10^8 M_\odot}\,{\rm erg\ s^{-1}}, \quad (1)$$

which can be used to normalize quantities like the mass accretion rate ($\dot{M}_0c^2$) and L. As done for this paper's abstract, one can also choose to normalize $\dot{M}_0$ by $\dot{M}_{\rm Edd} = (1/\eta_{\rm NT})L_{\rm Edd}/c^2$, where $\eta_{\rm NT}$ is

⋆ E-mail: jcm@umd.edu (JCM)

the nominal accretion efficiency for the Novikov-Thorne thin disk solution (Novikov & Thorne 1973) (commonly, a fixed $\eta_{\rm NT} = 0.1$ is used, but we include the spin dependence).

At very low accretion rates, $L/L_{\rm Edd} \ll 10^{-2}$, e.g., Sgr A* the super-massive BH (SMBH) at our Galactic Center (Narayan, Yi & Mahadevan 1995), the plasma becomes a radiatively inefficient accretion flow (RIAF) with some dissipated energy advecting into the BH and the rest ejected into a wind. These flows could be advection-dominated accretion flows (ADAFs) (Ichimaru 1977; Narayan & Yi 1994, 1995; Abramowicz et al. 1996, 1995; Popham & Gammie 1998), convection-dominated accretion flows (CDAFs) (Narayan et al. 2000; Quataert & Gruzinov 2000), and advection-dominated inflow-outflow solutions (ADIOSs) (Blandford & Begelman 1999; Begelman 2012). Such flows are optically thin and geometrically thick (disk height (H) to cylindrical radius (R) ratio of $|H/R| \sim 0.5$–0.9). Analytical and semi-analytical models agree well with the primary spectral features of, e.g., SgrA* (Yuan et al. 2003). Still, modern GRMHD simulations with physical cooling suggest that accretion rate of Sgr A* is actually near the limit of the regime where radiative cooling may be important (Dibi et al. 2012), while systems like M87 that are normally associated with low luminosity systems may have important radiative cooling (Mościbrodzka et al. 2011; Dibi et al. 2012).

RIAFs have been studied with various GRMHD codes (with no radiative transfer) (e.g., De Villiers et al. 2003; Gammie et al. 2003; Anninos et al. 2005; Del Zanna et al. 2007), and these simulations seek to find thermodynamically and dynamically self-consistent solutions and to determine what free parameters (such as net magnetic flux) set the results (Narayan et al. 2012; McKinney et al. 2012; Tchekhovskoy & McKinney 2012). Some effects of radiation have been included by performing radiative transfer during post-processing to produce observables (e.g. Schnittman et al. 2006; Shcherbakov et al. 2010), which is valid when the radiation has no dynamical importance. In a few cases, physically-motivated local cooling has been included (e.g., Fragile & Meier 2009; Dibi et al. 2012), which is permissable if the gas is quite optically thin. Simulations, however, have not been performed in a way that self-consistently determines the thermodynamic structure of the disk, which would be controlled by significant cooling or regulated by turbulent dissipation and winds. Instead, simulations with various initial conditions lead to evolved disk states of various disk thicknesses, such as $|H/R| \sim 0.1$–0.15 (Hawley & Krolik 2001; De Villiers et al. 2003; Beckwith et al. 2008b,a, 2009) and $|H/R| \sim 0.2$ (Hawley & Balbus 2002; Machida et al. 2000; Martí & Müller 2003; McKinney & Gammie 2004; Fragile et al. 2007; McKinney & Blandford 2009) and $|H/R| \sim 0.3$–0.4 (Igumenshchev et al. 2003; Penna et al. 2010), as well as radiatively efficient, geometrically thick flows with $|H/R| \sim 0.6$–1.0 (Stone & Pringle 2001; Hawley et al. 2001; Igumenshchev & Narayan 2002; Pen et al. 2003; Pang et al. 2011; McKinney et al. 2012).

For higher accretion rates, $10^{-2} \lesssim L/L_{\rm Edd} \lesssim 0.3$, the disk cools efficiently, and the inner accretion disk can collapse into an optically thick geometrically thin accretion disk (Shakura & Sunyaev 1973; Novikov & Thorne 1973; Thorne 1974; Esin et al. 1997, 1998; Martí & Müller 2003; McClintock & Remillard 2006; Done et al. 2007). In this regime, it remains uncertain whether such a radiation-dominated disk is stable (Lightman & Eardley 1974; Piran 1978; Hirose et al. 2009; Jiang et al. 2013). Example systems include transient black hole binaries (BHBs) that approach near-Eddington accretion rates near the peak of their outbursts (McClintock & Remillard 2006; Remillard & McClintock 2006; Done, Gierliński & Kubota 2007), during which they produce a thermal black-body-like spectrum consistent with standard α-disk theory (Shakura & Sunyaev 1973; Noble et al. 2011a; Frank et al. 2002) that allows one to measure black hole spins (McClintock et al. 2011; Straub et al. 2011). However, typical α-disk models assume an averaged vertical structure with limited treatment of the radiation. Simulations have only so-far included an ad hoc cooling function that leads to $|H/R| \sim 0.05$–0.1 (Shafee et al. 2008; Reynolds & Fabian 2008; Reynolds & Miller 2009; Noble et al. 2009; Penna et al. 2010; Noble et al. 2010; Sorathia et al. 2010; Noble et al. 2011b; Beckwith et al. 2011).

Near and beyond the Eddington luminosity limit, $L \gtrsim 0.3L_{\rm Edd}$, the accretion flow become geometrically thick and optically thick, and in this regime the photons can advect or remain trapped within the flow. The "slim disk" model treats this regime (Abramowicz et al. 1988; Sądowski 2009) (but for issues see Ohsuga et al. 2002) and additional physics such as thermal conduction has been added to such models (Ghasemnezhad et al. 2013), but it does not include multi-dimensional effects or magnetic fields. Super-Eddington accretion may help explain ultra-luminous X-ray sources as highly super-Eddington stellar-mass BHs (Watarai et al. 2001; Watarai et al. 2005), without requiring intermediate mass BHs (as required if accretion were limited to Eddington rates) (Miller & Colbert 2004). Also, a few black hole x-ray binaries spend significant periods of time with $L \gtrsim L_{\rm Edd}$ (e.g., SS433, Margon et al. 1979; Margon 1984; Takeuchi et al. 2010; GRS1915+105, Fender & Belloni 2004). In addition, tidal disruption events (TDEs) require such high accretion rates with geometrically-thick accretion disks (Coughlin & Begelman 2013) and strong magnetic fields (Bloom et al. 2011; Burrows et al. 2011; Levan et al. 2011; Zauderer et al. 2011; Tchekhovskoy et al. 2013).

This important regime may determine SMBH mass growth in the Universe from $z \sim 10$–20 to $z \sim 6$–8 leading to black holes with masses of $10^9 M_\odot$ (Collin et al. 2002; Barth et al. 2003; Willott et al. 2005; Fan et al. 2006; Willott et al. 2010; Mortlock et al. 2011; Kawakatu & Ohsuga 2011; Fabian 2012) and control the evolution of black hole mass and spin (Gammie et al. 2004; Volonteri et al. 2005; Berti & Volonteri 2008) as well as set the degree of active galactic nuclei (AGN) feedback (Di Matteo et al. 2005; Springel et al. 2005).

On the one hand, often it is assumed that mass accretion is limited by Eddington, since otherwise radiation blows off a massive wind and prevents accretion (see discussion in Takeuchi et al. 2009). Then one expects the mass accretion rate to be limited to Eddington ($\dot{M}_0 \lesssim \dot{M}_{\rm Edd}$), the luminosity to be limited to Eddington ($L \leqslant L_{\rm Edd}$), and the radiative efficiency ($\eta_{\rm rad}$) to be rougly given by Novikov-Thorne values, which vary from $\eta_{\rm rad} \sim 0.057, 0.065, 0.082, 0.26$ for $a/M = 0, 0.2, 0.5, 0.99$, respectively. Then, the disk luminosity is given by $L = \eta_{\rm rad}\dot{M}_0 c^2$. The black hole mass grows from M_i due to the residual mass not converted to energy, so giving $\dot{M} = (1-\eta_{\rm rad})\dot{M}_0$. Thus, $\dot{M} \leqslant (M/t_{\rm Edd})(1-\eta_{\rm rad})/\eta_{\rm rad}$ where $t_{\rm Edd} \equiv \kappa c/(4\pi G) \approx 4.5\times 10^8$yr. Hence,

$$\frac{M}{M_i} < \exp\left[\frac{t}{t_{\rm Edd}}(1/\eta_{\rm rad} - 1)\right], \qquad (2)$$

which is exponentially sensitive to efficiency (and hence exponentially sensitive to black hole spin). Over $t \sim 0.8$Gyr (roughly $z \sim 20$ to $z \sim 6$), Eddington-limited accretion with $a/M \approx 0.99$ leads to $M/M_i \lesssim 142$, a severe restriction to growth. One requires $a/M \lesssim 0.5$ and seeds of $M_i \approx 10M_\odot$ to reach $M \gtrsim 4\times 10^9 M_\odot$, as needed to produce quasars at $z \sim 6$–8.

On the other hand, photon-trapping can allow for super-Eddington mass accretion rates (Ohsuga & Mineshige 2007), such

that only L might be limited to near Eddington values. So one should split the efficiency due to radiation and accretion, given by $\eta_{\rm acc}$, such that $\dot{M} = (1-\eta_{\rm acc})\dot{M}_0$. Then

$$\frac{M}{M_i} < \exp\left[\frac{t}{t_{\rm Edd}}(1-\eta_{\rm acc})/\eta_{\rm rad}\right]. \quad (3)$$

In this case, if $a/M = 1$ such that $\eta_{\rm acc} \approx 0.43$, then for (e.g.) $\dot{M}_0 c^2 \sim 9L_{\rm Edd}$ one expects $\eta_{\rm rad} \sim 0.43/9 \approx 0.05$. In this case, one can easily have $a/M \approx 1$ and seeds of $M_i \approx 10M_\odot$ and reach $M \sim 10^{10}M_\odot$, as could be required by the most massive quasars at redshifts of $z \sim 6$–8. So even mild modifications to accretion rates and luminosities can exponentially affect the growth of black holes. This highlights the importance of including general relativity (to properly account for spin that controls both efficiencies), radiation (that at least determines the radiative efficiency), as well as magnetic fields (that control the spin down ; Gammie et al. 2004). So to understand the accretion physics in such systems, radiation GRMHD models (that self-consistently couple gas, radiation and magnetic fields) are crucial.

In order to study such a complex and sensitive interaction between GR, radiation, and magnetic fields, modern black hole (BH) accretion disk theory has relied upon several approximations, which often involve approximate closure schemes (e.g. magneto-hydrodynamics (MHD), flux-limited radiative diffusion) to capture unresolved spatial, unresolved temporal scales and unresolved physical processes. Such closure schemes can be more efficient than evolving distribution functions or individual particles/rays, and such methods have been successful in the study of radiative disks.

The flux-limited diffusion approximation is a closure that only allows isotropic emission relative to the fluid frame, which over-constrains disk emission in the highly radiative regions near the BH for the disk surface where the optical depth is order unity. This formalism has been included as an explicit scheme in some codes (Farris et al. 2008; Zanotti et al. 2011; Fragile et al. 2012), but implicit-explicit Runge-Kutta (Pareschi & Russo 2005) or fully implicit type numerical schemes are required to maintain stability for all optical depths (e.g. Roedig et al. 2012). Using a flux-limited diffusion approximation, small patches of radiatively efficient thin accretion disks have been simulated using the local shearing box approximation (Turner et al. 2003; Krolik et al. 2007; Blaes et al. 2007, 2011; Hirose et al. 2009a,b). Also, using a non-relativistic code and flux-limited diffusion, super-Eddington accretion flows have been simulated and their spectra computed (Ohsuga et al. 2003; Ohsuga et al. 2005; Ohsuga 2006; Ohsuga et al. 2009; Ohsuga & Mineshige 2011; Kawashima et al. 2012; Mineshige et al. 2012; Takeuchi et al. 2013; Yang et al. 2013).

To model a radiative disk around a rotating black hole self-consistently, the closure method should be able to handle both the optically thick (disk interior) and optically thin (corona-jet) limits in full GR including rotating black holes. One might treat the radiation more accurately than flux-limited diffusion using the "instant light" approximation (Hayes & Norman 2003; Giacomazzo & Rezzolla 2006; Jiang et al. 2012; Davis et al. 2012; Jiang et al. 2013), but currently such schemes do not allow relativistic radiative fluxes that are natural near the black hole (Jiang et al. 2012; Davis et al. 2012; Jiang et al. 2013).

In the work described here, we have implemented the so-called M1 closure scheme (Levermore 1984; Dubroca & Feugeas 1999; Giacomazzo & Rezzolla 2006; Sądowski et al. 2013c; Takahashi & Ohsuga 2013), which is similar to other schemes that use a truncated moment formalism (Shibata & Sekiguchi 2012). M1 closure allows a limited treatment of anisotropic radiation and works well at all optical depths. Using the Koral code, the M1 method has been shown to work well to handle axisymmetric GR hydrodynamic (HD) flows around black holes (Sądowski et al. 2013c) as well as axisymmetric GRMHD flows around rotating black holes (Sądowski et al. 2013a). We have implemented M1 into the GRMHD code HARM (Gammie et al. 2003), leading to the code we call HARMRAD, that adds to the Koral feature set the additional abilities to handle full 3D in spherical polar coordinates, higher-order reconstruction for both gas and radiation, and efficient parallel computation using distributed nodes on supercomputers.

The structure of the paper is as follows: The equations solved are presented in §2 for the gas fluid and in §3 for the radiation, numerical methods are presented in §4, and radiative tests of the method are presented in §5. Results for our fiducial 3D GRMHD model of a super-Eddington accretion flow around a rotating black hole are presented in §6. We summarize our method and results in §7.

2 GOVERNING MHD EQUATIONS

We solve the GRMHD equations for a radiative magnetized fluid in the test-field limit for the fluid in an arbitrary stationary spacetime. Internal coordinates $\underline{x}^\alpha \equiv (t, \underline{x}^{(1)}, \underline{x}^{(2)}, \underline{x}^{(3)})$ on a uniform grid map to arbitrary set of coordinates (Cartesian, spherical polar, etc.), e.g., for spherical polar coordinates: $\underline{r}^\alpha \equiv (t, r, \theta, \phi)$. We write tensors in an orthonormal basis gas-fluid frame using "widehats" as $\widehat{R}$ that just means the components of R have been transformed to the gas fluid frame in an orthonormal basis (i.e. for vectors, $\widehat{u} \equiv u^{\hat{\mu}}$). We write radiation fluid frame quantities as $\bar{u}$. Quasi-orthonormal vectors are denoted as $u_\mu \approx \sqrt{|g_{\mu\mu}|}u^\mu$. When necessary to distinguish from orthonormal versions, contravariant (covariant) vectors are denoted as $\underline{u}^\mu$ ($\underline{u}_\mu$), while higher-ranked coordinate basis tensors have no underbar. We work with Heaviside-Lorentz units, often set $c = GM = 1$ when no explicit units are given, and let the horizon radius be $r_{\rm H}$.

Mass conservation is given by

$$\nabla_\mu(\rho_0 \underline{u}^\mu) = 0, \quad (4)$$

where ρ_0 is the rest-mass density, $\underline{u}^\mu$ is the contravariant 4-velocity, and $\rho = \rho_0 \underline{u}^t$ is the lab-frame mass density.

Energy-momentum conservation is given by

$$\nabla_\mu T^\mu_{\ \nu} = G_\nu, \quad (5)$$

where G_ν is an external 4-force and the stress energy tensor $T^\mu_{\ \nu}$ includes both matter (MA) and electromagnetic (EM) terms:

$$\begin{aligned} T^{{\rm MA}\mu}_{\ \ \ \nu} &= (\rho_0 + e_{\rm gas} + p_{\rm gas})\underline{u}^\mu \underline{u}_\nu + p_{\rm gas}\delta^\mu_\nu, \\ T^{{\rm EM}\mu}_{\ \ \ \nu} &= b^2 \underline{u}^\mu \underline{u}_\nu + p_b \delta^\mu_\nu - \underline{b}^\mu \underline{b}_\nu, \\ T^\mu_{\ \nu} &= T^{{\rm MA}\mu}_{\ \ \ \nu} + T^{{\rm EM}\mu}_{\ \ \ \nu}. \end{aligned} \quad (6)$$

The MA term can be decomposed into a particle (PA) term: $T^{{\rm PA}\mu}_{\ \ \ \nu} = \rho_0 \underline{u}_\nu \underline{u}^\mu$ and an enthalpy (EN) term. The MA term can be reduced to a free thermo-kinetic energy (MAKE) term, which is composed of free particle (PAKE) and enthalpy (EN) terms:

$$\begin{aligned} T^{{\rm MAKE}\mu}_{\ \ \ \ \nu} &= T^{{\rm MA}\mu}_{\ \ \ \nu} - \rho_0 \underline{u}^\mu \underline{\eta}_\nu/\alpha, \\ T^{{\rm PAKE}\mu}_{\ \ \ \ \nu} &= (\underline{u}_\nu - \underline{\eta}_\nu/\alpha)\rho_0 \underline{u}^\mu, \\ T^{{\rm EN}\mu}_{\ \ \ \nu} &= (e_{\rm gas} + p_{\rm gas})\underline{u}^\mu \underline{u}_\nu + p_{\rm gas}\delta^\mu_\nu, \end{aligned} \quad (7)$$

such that $T^{{\rm MAKE}\mu}_{\ \ \ \ \nu} = T^{{\rm PAKE}\mu}_{\ \ \ \ \nu} + T^{{\rm EN}\mu}_{\ \ \ \nu}$. Here, $e_{\rm gas}$ is the internal energy

density and $p_{\rm gas} = (\Gamma-1)e_{\rm gas}$ is the ideal gas pressure with adiabatic index Γ. The contravariant fluid-frame magnetic 4-field is given by $\underline{b}^\mu$, which is related to the lab-frame 3-field via $\underline{b}^\mu = \underline{B}^\nu h^\mu_\nu/\underline{u}^t$ where $h^\mu_\nu = \underline{u}^\mu\underline{u}_\nu + \delta^\mu_\nu$ is a projection tensor, and δ^μ_ν is the Kronecker delta function. The magnetic energy density (u_b) and pressure (p_b) are $u_b = p_b = \underline{b}^\mu\underline{b}_\mu/2 = b^2/2$. The total pressure is $p_{\rm tot} = p_{\rm gas} + p_b$, and plasma $\beta \equiv p_{\rm gas}/p_b$. The 4-velocity of a zero angular momentum observer (ZAMO) is $\underline{\eta}_\mu = \{-\alpha, 0, 0, 0\}$ where $\alpha = 1/\sqrt{-g^{tt}}$ is the lapse. The 4-velocity relative to this ZAMO is $\underline{\tilde{u}}^\mu = \underline{u}^\mu - \gamma\underline{\eta}^\mu$ where $\gamma = -\underline{u}^\alpha\underline{\eta}_\alpha$.

A corresponding entropy conservation equation (that can be used instead of the energy equation) is given by the evolution of the specific gas entropy $s_{\rm gas,s}$ as determined by the comoving time-rate of change $Ds_{\rm gas,s}/Dt \equiv \partial_\tau s_{\rm gas,s}$. Using baryon conservation one obtains

$$\nabla_\mu(\rho_0 u^\mu s_{\rm gas,s}) = \rho_0\frac{Ds_{\rm gas,s}}{Dt} = \rho_0\frac{\partial s_{\rm gas,s}}{\partial\tau} = G_S \tag{8}$$

where the entropy density is given by $S \equiv \rho_0 s_{\rm gas,s}$, and where the right-hand-side (G_S) corresponds to a source or sink of entropy. To obtain machine accurate entropy conservation, the specific entropy must be per unit volume. For example, for an ideal gas the specific entropy constant $K = P/\rho_0^\gamma$ is constant at constant specific entropy, but using such an entropy tracer only leads to entropy conservation truncation error. Using instead $s_{\rm gas,s} = \log(P^n/\rho_0^{n+1})$ with $n = 1/(\gamma-1)$, such that the entropy density is $s_g = \rho_0 s_{\rm gas,s}$, leads to entropy conservation at machine round-off error.

Magnetic flux conservation is given by the induction equation

$$\partial_t(\sqrt{-g}\underline{B}^i) = -\partial_j[\sqrt{-g}(\underline{B}^i\underline{v}^j - \underline{B}^j\underline{v}^i)], \tag{9}$$

where $g = {\rm Det}(g_{\mu\nu})$ is the metric's determinant, and the lab-frame 3-velocity is $\underline{v}^i = \underline{u}^i/\underline{u}^t$. No explicit viscosity or resistivity are included, but we use the energy conserving HARM scheme so all dissipation is captured (Gammie et al. 2003; McKinney 2006).

Apart from any physical source term giving a non-zero G_μ, the energy-momentum conservation equations are only otherwise modified due to so-called numerical density floors that keep the numerical code stable as described in detail in Appendix A of McKinney et al. (2012). The injected densities are tracked and removed from all calculations.

3 GOVERNING RADIATIVE TRANSFER EQUATIONS

For a radiation stress-energy tensor R^μ_ν, total energy-momentum conservation ($\nabla\cdot(T+R) = 0$) for the MHD fluid and radiation can be written using the 4-force density G^ν as

$$\begin{aligned} T^\mu_{\nu\ ;\mu} &= G_\nu, \\ R^\mu_{\nu;\mu} &= -G_\nu, \end{aligned} \tag{10}$$

The radiation stress-energy tensor can be obtained from its simple form in an orthonormal frame where it is comprised of various moments of the specific intensity I_ν, as discussed in Sądowski et al. (2013c). E.g., in an orthonormal fluid frame it takes the following form,

$$\widehat{R} = \left[\begin{array}{cc} \widehat{E} & \widehat{F^i} \\ \widehat{F^j} & \widehat{P^{ij}} \end{array}\right], \tag{11}$$

where, for frequency ν and solid angle Ω, the orthonormal fluid-frame quantities

$$\widehat{E} = \int \widehat{I_\nu}\,{\rm d}\nu\,{\rm d}\Omega, \tag{12}$$

$$\widehat{F^i} = \int \widehat{I_\nu}\,{\rm d}\nu\,{\rm d}\Omega\,{\rm N^i}, \tag{13}$$

$$\widehat{P^{ij}} = \int \widehat{I_\nu}\,{\rm d}\nu\,{\rm d}\Omega\,{\rm N^i}\,{\rm N^j} \tag{14}$$

are the radiation energy density, the radiation flux and the radiation pressure tensor, respectively, and N^i is a unit vector in direction x^i.

The radiation stress-energy tensor allows one to obtain the radiation 4-force, G^μ as given by (Mihalas & Mihalas 1984),

$$G^\mu = \int(\kappa_{\nu,{\rm tot}}I_\nu - \eta_\nu)\,{\rm d}\nu\,{\rm d}\Omega\,{\rm N^i}, \tag{15}$$

which in the orthonormal fluid frame becomes

$$\widehat{G} = \left[\begin{array}{c} \kappa_{\rm abs}\widehat{E} - \lambda \\ \kappa_{\rm tot}\widehat{F^i} \end{array}\right], \tag{16}$$

where the gas-fluid frame energy density emission rate of the gas is given by λ, and for a given absorption opacity, Kirchhoff's law gives that $\lambda = \kappa_{\rm abs}4\pi\widehat{B}$ for $\widehat{B}_{\rm gas} = a_{\rm rad}T^4_{\rm gas}/(4\pi)$. Here, $\widehat{B}_{\rm gas} = \sigma_{\rm rad}T^4_{\rm gas}/\pi$ is the integrated Planck function corresponding to the gas temperature $T_{\rm gas}$, $\sigma_{\rm rad}$ is the Stefan-Boltzmann constant, $\kappa_{\nu,{\rm tot}}$ and η_ν denote the frequency-dependent opacity and emissivity coefficients, respectively, while $\kappa_{\rm abs}$ and $\kappa_{\rm sca}$ are the frequency integrated absorption and scattering opacity coefficients, respectively, and the total opacity is given by $\kappa_{\rm tot} = \kappa_{\rm abs} + \kappa_{\rm sca}$.

Using covariance (or boosting from the lab-frame to fluid orthonormal frame), the covariant 4-force is then

$$G^\mu = -(\kappa_{\rm abs}R^\mu_\alpha u^\alpha + \lambda u^\mu) - \kappa_{\rm es}(R^\mu_\alpha u^\alpha + R^\alpha_\beta u_\alpha u^\beta u^\mu). \tag{17}$$

The corresponding entropy source term is obtained from

$$T_{\rm gas}\frac{ds_{\rm gas,s}}{d\tau} = \frac{dq_{\rm gas}}{d\tau} \tag{18}$$

such that in covariant form one has

$$(\rho_0 s_{\rm gas,s}u^\mu)_{;\mu} = -\frac{1}{T_{\rm gas}}G^\mu u_\mu \equiv G_S \tag{19}$$

that specifies Eq. (8) in the presence of a radiation 4-force.

3.1 Closure scheme

To close the above set of equations we need a prescription to compute the second moments of the angular radiation intensity distribution. Specifically, we need $R^{\mu\nu}$ only knowing the radiative energy density and fluxes in some frame (e.g. R^{tt} and R^{ti} in the lab-frame).

The simplest approach is the Eddington approximation, which assumes a nearly isotropic radiation field in the gas fluid frame, which in the gas fluid frame is given by

$$\widehat{P^{ij}} = \frac{1}{3}\widehat{E}\delta^{ij}. \tag{20}$$

However, the radiation is only isotropic in the optically thick limit, so this closure does not handle optically thin flows.

To handle general optical depths, we use the M1 closure (Levermore 1984), which assumes the radiation satisfies the Eddington closure in an independent radiation frame within which radiation fluxes vanish. Thus, in the radiation frame, $\bar{R}^{tt} = \bar{E}$, $\bar{R}^{ii} = \bar{E}/3$, and all other components of $\bar{R}$ are zero. In the radiation rest frame, the radiation stress tensor can be written as

$$\bar{R}^{\mu\nu} = \frac{4}{3}\bar{E}\,\bar{u}^\mu_{\rm rad}\bar{u}^\nu_{\rm rad} + \frac{1}{3}\bar{E}\,g^{\mu\nu}, \tag{21}$$

where $\bar{u}^\mu_{\rm rad}$ is the radiation frame's 4-velocity. Using general covariance (or boosting into the lab-frame), the covariant expression is

$$R^{\mu\nu} = \frac{4}{3}\bar{E}\,u^\mu_{\rm rad}u^\nu_{\rm rad} + \frac{1}{3}\bar{E}\,g^{\mu\nu}, \quad (22)$$

The quantity $\bar{E} = u^\mu_{\rm rad}u^\nu_{\rm rad}R_{\mu\nu}$ is the radiation energy density as measured in the radiation rest frame.

For an orthonormal Cartesian basis, the above formulation reduces to the standard formulae (Levermore 1984; Dubroca & Feugeas 1999; Giacomazzo & Rezzolla 2006). For instance, the radiation pressure tensor $\widehat{P}^{ij}$ in the fluid frame has the form,

$$\widehat{P}^{ij} = \left(\frac{1-\xi}{2}\delta^{ij} + \frac{3\xi-1}{2}\frac{f^i f^j}{|f|^2}\right)\widehat{E}, \quad (23)$$

where $f^i = \widehat{F}^i/\widehat{E}$ is the reduced radiative flux and ξ is the Eddington factor given by (Levermore 1984),

$$\xi = \frac{3+4f^i f_i}{5+2\sqrt{4-3f^i f_i}}. \quad (24)$$

In the extreme "optically thick limit", $\widehat{F}^i \approx 0$, and then $f^i = 0$, $f^i f_i = 0$ and $\xi = 1/3$, which gives the expected Eddington approximation,

$$\widehat{P}^{ij}_{\tau\gg1} = \begin{bmatrix} 1/3 & 0 & 0 \\ 0 & 1/3 & 0 \\ 0 & 0 & 1/3 \end{bmatrix}\widehat{E}. \quad (25)$$

In the opposite extreme "optically thin limit", $\widehat{F}^1 = \widehat{E}$, i.e., a unidirectional radiation field directed along the x-axis, we have $f^i = \delta^i_1$, $f^i f_i = 1$ and $\xi = 1/3$, which gives

$$\widehat{P}^{ij}_{\tau\ll1} = \begin{bmatrix} 1 & 0 & 0 \\ 0 & 0 & 0 \\ 0 & 0 & 0 \end{bmatrix}\widehat{E}, \quad (26)$$

which gives the expected intensity distribution of a Dirac δ-function parallel to the flux vector.

The M1 closure scheme thus handles both optical depth extremes well, and smoothly and stably interpolates between these extreme optical depths. However, because M1 treats the radiation as isotropic in a single frame, it cannot handle general anisotropic intensity distributions. So, at locations where multiple radiation fluids interact, M1 isotropizes the radiation in an averaged radiation frame. M1 is expected to be an ok approximation for expanding radiation fields like from accretion disks, but a convergent radiation field will lead to "photon collisions" even in optically thin regions. In any case, M1 closure will provide a superior treatment of radiation in the optically thin regions near and above the disk photosphere, as compared to the Eddington approximation or flux-limited diffusion.

4 NUMERICAL METHODS: HARMRAD

The core of HARMRAD is built upon HARM. The GRMHD code HARM is based upon a conservative shock-capturing Godunov scheme with 3rd order (2nd or 4th order choosable) Runge-Kutta time-stepping, Courant factor 0.5, LAXF (HLL choosable, but less stable for highly magnetized flows) fluxes, simplified wave speeds, PPM-type interpolation for primitive quantities ($P = \{\rho_0, e_{\rm gas}, \tilde{\underline{u}}^i, \underline{B}^i\}$), a staggered magnetic field representation, and any regular grid warping (Gammie et al. 2003; Noble et al. 2006; Tchekhovskoy et al. 2007). Treatment of the numerical density floors, 3D polar axis, conserved to primitive inversion attempts and reductions to simpler equations, and connection coefficients ($\Gamma^\lambda_{\nu\kappa}$) is provided in the appendix in McKinney et al. (2012). As with HARM, HARMRAD is based upon a hybrid OpenMP - MPI framework use ROMIO for parallel I/O operating at up to order 32,000 cores on Kraken at > 70% efficiency. Double precision floats are used for all tests, although long double precision (including for all needed transcendental functions) can be used to test precision issues.

The internal code units set scales for length of $\tilde{L} = GM/c^2$, time $\tilde{T} = \tilde{L}/c$, velocity $\tilde{V} = \tilde{L}/\tilde{T}$, $\tilde{\rho} = 1$ for mass density in cgs units (i.e. grams) for a fiducial arbitrary choice of $M = 10M_\odot$, $\tilde{M} = \tilde{\rho}\tilde{L}^3$, $\tilde{E} = \tilde{M}\tilde{V}^2$, $\tilde{U} = \tilde{\rho}\tilde{V}^2$, and gas temperature $\tilde{T}_{\rm gas} = m_b c^2/k_b$ for baryon mass m_b and Boltzmann's constant k_b. This gives an opacity scaling of $\tilde{\kappa} = \tilde{L}^2/\tilde{M}$, and a radiation constant scaling of $\tilde{a}_{\rm rad} = \tilde{U}/\tilde{T}^4_{\rm gas}$. We sometimes report mass fluxes, energy fluxes, time, density, magnetic field, etc. as per unit Eddington to simplify these scalings for the reader, and these are obtained by simply rescaling $\dot{M}_{\rm Edd}$ by only c, G, and M.

The MHD and radiation conservation laws are evolved using a method of lines using a Runge Kutta approach. We consider a set of $q = 13$ quantities:

(i) primitive: $P_q = \{\rho_0, e_{\rm gas}, \tilde{\underline{u}}^\mu_{\rm gas}, B^i, \bar{E}, \tilde{\underline{u}}^\mu_{\rm rad}, e_{\rm gas}\}$.
(ii) conserved: $U_q = \sqrt{-g}\{\rho_0 u^t, \rho_0 u^t_{\rm gas} + T^t{}_t, T^t{}_i, B^i, R^t{}_\nu, S\,u^t\}$,
(iii) fluxes: $F_q = \sqrt{-g}\{\rho_0 u^j, T^j{}_\nu, B^i v^j - B^j v^i, R^j{}_\nu, S\,u^j\}$,
(iv) geometry: $\mathrm{SM}_q = \sqrt{-g}\{0, T^\kappa{}_\lambda\Gamma^\lambda{}_{\nu\kappa}, 0, 0, 0, R^\kappa{}_\lambda\Gamma^\lambda{}_{\nu\kappa}, 0\}$,
(v) GAS-RAD 4-force: $\mathrm{SR}_q = \sqrt{-g}\{0, G_\nu, 0, 0, 0, -G_\nu, G_S\}$,

Each U_q, F_q, SM_q, SR_q can be obtained in closed form as functions of P_q. Magnetic field primitives/conserved/source quantities sit at cell faces, while magnetic field fluxes (EMFs) sit at the corners of each 2D plane that passes through the cell center. All non-magnetic primitives/conserved/source quantities sit at cell centers, while non-magnetic fluxes sit at cell faces.

4.1 Implicit-Explicit Runge-Kutta

For large 4-forces relative to the conserved quantities (e.g. for large optical depths), the radiative 4-force G_ν become stiff, making explicit integration practically impractical (e.g., Zanotti et al. 2011). To generally handle the 4-force in all regimes, we treat the 4-force term using an implicit-explicit (IMEX) Runge-Kutta (RK) scheme to evolve the equations forward in time on each full timestep of size dt. For intermediate or full steps, let the explicit-only (X) terms and IMEX (M) terms be written as

$$X^i_q \equiv \Delta_j \mathcal{F}^{i\,j}_q/dx^j + \mathrm{SM}^i_q, \quad (27)$$

$$M^i_q \equiv \mathrm{SR}^i_q, \quad (28)$$

where the first equation comes from a Riemann solver with j summed over all spatial dimensions. For any q, let U^i be the value of U, such that $X^i \equiv X(U^i)$ and $M^i \equiv M(U^i)$. Then, IMEX RK schemes take the form (Pareschi & Russo 2005)

$$U^i = U^n + dt\sum_{j=1}^{i-1}\tilde{a}_{ij}X^j + dt\sum_{j=1}^{\nu}a_{ij}M^j \quad (29)$$

$$U^{n+1} = U^n + dt\sum_{i=1}^{\nu}\tilde{\omega}_i X^i + dt\sum_{i=1}^{\nu}\omega_i M^i, \quad (30)$$

where U^i are the auxiliary intermediate values of the IMEX Runge-Kutta scheme and U^{n+1} is the final full step solution. The matrices $\tilde{A} = (\tilde{a}_{ij})$ and $A = (a_{ij})$ are $\nu\times\nu$ matrices (for a ν-stage IMEX scheme), such that the resulting scheme is explicit in F (i.e. $\tilde{a}_{ij} = 0$

for $j \geqslant i$) and implicit in M. An IMEX Runge-Kutta scheme is characterized by these two matrices and the coefficient vectors $\tilde{\omega}_i$ and ω_i. Since simplicity and efficiency in solving the implicit part at each step is important, we consider diagonally implicit Runge-Kutta (DIRK) schemes (i.e. $a_{ij} = 0$ for $j > i$) for stiff terms.

We use a set of IMEX coefficients that generates so-called strongly stable preserving (SSP) (formally known as total variational diminishing (TVD)) schemes (Pareschi & Russo 2000, 2005), such that the total variation in U_q always diminishes. We also restrict ourselves to schemes that are asymptotically preserving (AP), such that in the infinitely stiff limit the RK method preserves higher-order accuracy and becomes an explicit RK method for the non-radiative GRMHD equations – as desired. For efficiency, we also restrict ourselves to diagonally implicit Runge-Kutta (DIRK) schemes with (i.e. $a_{ij} = 0$ for $j > i$) for the stiff terms that reduces the number of calculations required. Several applications of the IMEX method demonstrate its accuracy and robustness (Palenzuela et al. 2009; Kumar 2011; Roedig et al. 2012; Takahashi et al. 2013; Takahashi & Ohsuga 2013). Improvements in IMEX schemes beyond our implementation are discussed elsewhere (Boscarino & Russo 2009; Boscarino 2011; Boscarino & Russo 2013; Trenchea 2014).

The IMEX scheme can be written many ways, and here we expand the form for implementation into HARMRAD. The 2nd order IMEX scheme has 2 explicit stages (given in square brackets) and 2 implicit stages and one final result for U^{n+1}, given by (IMEX2)

$$U^0 = [U^n] + \gamma dt M^0 \quad (31)$$

$$U^1 = [\frac{3\gamma-1}{\gamma}U^n + \frac{1-2\gamma}{\gamma}U^0 + dtF^0] + \gamma dt M^1 \quad (32)$$

$$U^{n+1} = [\frac{1}{2}U^n + \frac{1}{2}U^1 + \frac{dt}{2}F^1 + dt\gamma M^0 + dt\frac{1-\gamma}{2}M^1], \quad (33)$$

where $\gamma = 1 - 1/\sqrt{2}$. The steps are written so explicit steps only need use the immediately prior U^i or U^n to avoid needing to store intermediate F^i, while one should progressively store each M^i as computed so available for any substep.

Similarly, another 2nd order IMEX scheme has 3 explicit stages and 3 implicit stages, given by (IMEX2B)

$$U^0 = [U^n] + \frac{dt}{4}M^0 \quad (34)$$

$$U^1 = [U^n + \frac{dt}{2}F^0] + \frac{dt}{4}M^1 \quad (35)$$

$$U^2 = [U^1 + \frac{dt}{2}F^1 + \frac{dt}{3}M^0 + \frac{dt}{12}M^1] + \frac{dt}{3}M^2 \quad (36)$$

$$U^{n+1} = [\frac{1}{3}U^n + \frac{2}{3}U^2 + \frac{dt}{3}F^2 + \frac{dt}{9}(M^0 + M^1 + M^2)], \quad (37)$$

which again is written to avoid storing intermediate F^i.

Likewise, the 3rd order IMEX scheme has 3 explicit stages, 4 implicit stages, given by (IMEX3)

$$U^0 = [U^n] + \alpha dt M^0 \quad (38)$$

$$U^1 = [2U^n - U^0] + \alpha dt M^1 \quad (39)$$

$$U^2 = [U^n + dtF^1 + (1-\alpha)dtM^1] + \alpha dt M^2 \quad (40)$$

$$U^3 = [\frac{3}{4}U^n + \frac{1}{4}U^2 + \frac{dt}{4}F^2 + \beta dt M^0 + \frac{(-1+\alpha+4\eta)dt}{4}M^1 + \frac{(2-5\alpha-4(\beta+\eta))dt}{4}M^2] + \alpha dt M^3 \quad (41)$$

$$U^{n+1} = [\frac{1}{3}U^n + \frac{2}{3}U^3 + \frac{2dt}{3}F^3 + \frac{-2\beta dt}{3}M^0 + \frac{(1-4\eta)dt}{6}M^1 + \frac{(-1+4\alpha+4(\beta+\eta))dt}{6}M^2 + \frac{4(1-\alpha)dt}{6}M^3], \quad (42)$$

which again is written to avoid storing intermediate F^i. Here $\alpha \approx 0.24169426078821$, $\beta \approx 0.06042356519705$, and $\eta \approx 0.12915286960590$ (Pareschi & Russo 2005).

For equal implicit and explicit stages as well as equal coefficients for either implicit or explicit terms, one obtains the standard mid-point non-TVD 2nd order RK (RK2M), TVD 2nd order RK (RK2), TVD 3rd order RK (RK3), and 4th order non-TVD RK (RK4) methods (Shu & Osher 1988), where then the implicit and explicit substeps use the exact same timestep coefficients for substeps and final solution. This leads to the implicit terms being treated to 2nd order in time and 1st order in space for optically thick fast waves.

In this paper, for simplicity and for historial reasons, we only consider such simplified IMEX Runge-Kutta methods. In particular, we use the RK3 method with the same stages and coefficients for both explicit and implicit terms. The full higher-order IMEX2, IMEX2B, and IMEX3 will be considered for other applications beyond the scope of this paper.

4.2 HARMRAD Algorithm

During each sub-step of the Runge-Kutta time integration, the code carries out the following steps in the given order:

(i) P_q on the evolved domain are mapped into ghost cells however boundary conditions required.

(ii) P_q at cell centers is used to compute U_q at cell centers.

(iii) SM_q geometry sources are computed at cell centers.

(iv) P_q is interpolated from cell centers to faces in each direction in each dimension giving P_L, P_R at each face in each dimension.

(v) For each L and R, F_q is computed at faces from P_q at faces of cube in three-dimensions

(vi) For each L and R, v_w wavespeeds (v_+ for positive direction, v_- for negative direction) are computed at faces for each P_q.

(vii) Using F_q, U_q, v_+, v_- at each face, Godunov flux is computed using the 2-state HLL solution:

$$\mathcal{F}_q = \frac{v_{\rm min}F_{q,R} + v_{\rm max}F_{q,L} - v_{\rm min}v_{\rm max}(U_{q,R} - U_{q,L})}{v_{\rm min} + v_{\rm max}}, \quad (43)$$

where $v_{\rm min} = -\min(0, v_{-,R}, v_{-,L})$, $v_{\rm max} = \max(0, v_{+,R}, v_{+,L})$, or LAXF solution:

$$\mathcal{F}_q = \frac{1}{2}(F_{q,R} + F_{q,L} - v_{\rm tot}(U_{q,R} - U_{q,L})), \quad (44)$$

where $v_{\rm tot} = \max(v_{\rm min}, v_{\rm max})$.

(viii) B^i, v^j at cell faces are interpolated to cell centers and to the corner of each 2D plane passing through the cell center.

(ix) Godunov EMF flux is computed using 4-state Riemann LAXF/HLL solution using B^i, v^j at corners (Del Zanna et al. 2007).

(x) $U_{q,i}$ is set for both cell centered and staggered U_q's.

(xi) Magnetic field primitives P_q^{i+1} are obtained, so implicit solver uses the final magnetic field as guess.

(xii) IMEX solution is found based upon explicit U_q^n, X^i and IMEX radiation source term M^i that converges to give $U_{q,(i+1)}$ and $P_{q,(i+1)}$. For each step, MHD and RAD inversions from conserved to primitive quantities are performed.

(xiii) Backup methods are employed if implicit solver fails.

4.3 Primitive Spatial Reconstruction

As in HARM, PPM interpolation (with no contact steepener, but with shock flattener) (Colella & Woodward 1984) is used to reconstruct primitive quantities at different spatial locations. For spherical polar coordinates, for the radial and ϕ directions, we interpolate $\sqrt{-g}\underline{\tilde{u}}^i_{\rm gas}$, $\sqrt{-g}\underline{\tilde{u}}^i_{\rm rad}$, and $\sqrt{-g}B^i$, and otherwise we interpolate P_q. The PPM reconstruction's monotonized slopes use the monotonized central (MC) limiter. The PPM flattener (with shock parameter SP0=0.75 as in the Flash code; Fryxell et al. 2000) is applied separately on GAS and RAD quantities, but each GAS and RAD flattener is formed as a linear interpolation based upon the optical depth τ, so that by $\tau = 1/2$, each GAS and RAD use a single flattener value set as the maximum of the GAS and RAD flattener values. The PPM flattener for the GAS quantities uses the specific mass flux $\sqrt{-g}u^i_{\rm gas}$ and gas pressure, and the RAD quantities use $\sqrt{-g}u^i_{\rm rad}$ and radiation pressure. The pressures used in the flattener are linearly interpolated for each GAS and RAD to become a total GAS+RAD pressure in the limit that $\tau = 1/2$. On Runge-Kutta sub-steps, the maximum flattener value over any prior sub-steps is used for the current sub-step.

4.4 Characteristic wavespeeds

Godunov schemes, like the LAXF scheme, require knowledge of the maximal characteristic wave speeds of the system (v_w in Eq. 44). The wave speed calculation can be quite approximate, because the value only enters as a numerical grid dissipation that improves the stability of the method in handling discontinuities. Each GAS and RAD fluxes are computed separately, which preserves stability while avoids excessive artificial numerical viscosity when the characteristic wavespeeds are not separated.

The GAS's fast magnetosonic characteristics are computed as in HARM (see the approximate dispersion in section 3.2 of Gammie et al. 2003), which solves for the lab-frame characteristic 3-velocity ($v_{w,\rm gas}$) in terms of the covariant quantities such as the metric, gas-fluid 4-velocity, and gas-fluid frame magnetosonic speed $c_{\rm ms}$. For GAS quantities, the wavespeeds are computed at faces for the left and right states before forming the 2-state Riemann solution, while for the magnetic field fluxes (EMFs) the wave speeds are interpolated from those face values to the EMF location before forming the 4-state Riemann solution.

For the M1-closure scheme, the radiation characteristic moves at a uniform value of $c_{\rm rad}$ in the radiation frame, so we simply use the HARM method to obtain the lab-frame velocity $v_{w,\rm rad}$ from $c_{\rm rad}$ by replacing the gas-fluid 4-velocity with the radiation-fluid 4-velocity. We do not solve for the Jacobian's eigenvalues as done in Koral (see section 3.2 in Sądowski et al. 2013c).

To determine $c_{\rm rad}$, we consider the optically thin and thick limits to determine how this wavespeed is used to compute the flux using the Godunov scheme. In the optically thin limit, $c_{\rm rad} = \pm 1/\sqrt{3}$. In the limit of large optical depths, we follow the Koral code by using the effective wave speed rather than the actual wave speed. The radiative energy density, when decoupled from gas (e.g., for $\kappa_{\rm abs} \ll 1$ but $\kappa_{\rm tot} \gg 1$), has a diffusion coefficient D given by (see Section 5.4)

$$D = \frac{1}{3\kappa_{\rm tot}}. \tag{45}$$

In this limit the distribution of radiative energy density should remain stationary ($\partial/\partial t \to 0$). On the other hand, the optically thin value of $c_{\rm rad}$ is near the speed of light (Giacomazzo & Rezzolla 2006). If such large wave speeds are incorporated into a numerical scheme they will result in large, unphysical, numerical diffusion. To limit this effect, we modify the radiative wave speeds in the fluid frame according to

$$\begin{aligned} a^i_R &\to \min\left(a^i_R, \frac{4}{3\tau^i}\right), \\ a^i_L &\to \max\left(a^i_L, -\frac{4}{3\tau^i}\right), \end{aligned} \tag{46}$$

where a^i_R and a^i_L are the maximal right- and left-going radiative wave speeds in the fluid frame in the direction i, and $\tau^i = \kappa_{\rm tot}{\rm dx^i}$ is the total optical depth of a given cell in that direction, where $\rm dx^i$ is the orthonormal cell size in each direction.

The smaller the characteristic wave speed in Eq. (44), the weaker the numerical diffusion. This choice of the wave speed limiter (Eq. 46) is motivated by the fact that, for a diffusion equation of the form $y_{,t} = Dy_{,xx}$, the maximum allowed time step for an explicit numerical solver is

$$\Delta t = \frac{(\Delta x)^2}{4D}. \tag{47}$$

This expression, combined with Eq. (45), gives

$$\frac{\Delta x}{\Delta t} = \frac{4}{3\kappa_{\rm tot}\Delta x} = \frac{4}{3\tau}, \tag{48}$$

which is the limiter introduced in Eq. (46). Essentially, we set $v_{w,\rm rad}$ to the velocity of diffusion in the optically thick limit.

For each Runge-Kutta timestep, in each direction, the timestep is to $dt_i = dx_i/v^i_w$ for v^i_w as the larger of $v^i_{\rm gas}$ and $v^i_{\rm rad}$, where $v_{w,\rm gas}$ and $v_{w,\rm rad}$ were obtained as effectively located at cell centers by taking the maximum of characteristic speed at the left or right of each cell face. These characteristic speeds were constructed as lab-frame internal HARM coordinate basis 3-velocities using the above-mentioned HARM dispersion relation to convert $c_{\rm gas}, c_{\rm rad}$ to $v_{w,\rm gas}, v_{w,\rm rad}$. The dx_i are the uniform (constant) grid internal cell sizes in each dimension. The overall timestep is set as $dt = 1/(1/dt_1 + 1/dt_2 + 1/dt_3)$.

4.5 MHD Inversion of Conserved to Primitive Quantities

The gas MHD inversion involves taking known conserved quantities U_q and obtaining primitive quantities P_q. Our method uses a single non-linear equation as a function of one MHD variable plus the MHD conserved quantities in order to obtain a solution to gas primitives $P_q^{n+1}(U_q^{n+1})$ for the explicit case (Noble et al. 2006; Mignone & McKinney 2007; Sądowski et al. 2013c) or steps within the implicit solver.

First, we calculate $p(\rho_0, e_{\rm gas}) = p(\rho_0, \chi_{\rm gas})$ where $\chi_{\rm gas} = e_{\rm gas} + p_{\rm gas}$ (e.g. ideal gas of $p_{\rm gas} = (\Gamma - 1)\, e_{\rm gas}$), $w = \rho_0 + e_{\rm gas} + p_{\rm gas}$, ZAMO relative Lorentz factor $\gamma_{\rm gas} = \sqrt{1 + g_{ij}\tilde{u}^i_{\rm gas}\tilde{u}^j_{\rm gas}}$, ZAMO relative 4-velocity $\tilde{u}^\mu_{\rm gas} = u^\mu_{\rm gas} - \gamma_{\rm gas}\eta^\mu$, $\tilde{v}^\mu_{\rm gas} = \tilde{u}^\mu_{\rm gas}/\gamma_{\rm gas}$ such that $\gamma^2_{\rm gas} = 1/(1 -$

$\tilde{v}^2_{\rm gas}$), ZAMO field $\mathcal{B}^\mu = \eta_\mu {}^*F^{\mu\nu} = \alpha B^\mu$ for HARM magnetic field variable B^μ, fluid-frame field $b^\mu = h^\mu{}_\nu \mathcal{B}^\nu/\gamma$, with projection tensor $h^\mu{}_\nu = \delta^\mu_\nu + u^\mu{}_{\rm gas} u_{\nu{\rm gas}}$, and new variable $W \equiv w\gamma^2_{\rm gas}$ or $W' = W - D = D(\gamma_{\rm gas} - 1) + \chi_{\rm gas}\gamma^2_{\rm gas}$. The $\mathcal{B}^i$s are both primitive and conserved variables.

The ZAMO mass density is given by

$$D = \gamma_{\rm gas}\rho_0, \tag{49}$$

and

$$b^2 = \frac{1}{\gamma^2_{\rm gas}}\left[\mathcal{B}^2 + \left(\mathcal{B}^\mu u_{\mu{\rm gas}}\right)^2\right] \tag{50}$$

and

$$n_\mu b^\mu = -u_{\mu{\rm gas}}\mathcal{B}^\mu. \tag{51}$$

Using $\eta_\mu \mathcal{B}^\mu = 0$, then

$$\begin{aligned} Q_\mu &\equiv -\eta_\nu T^\nu{}_\mu = \gamma_{\rm gas}\left(w + b^2\right)u_{\mu{\rm gas}} - \left(p_{\rm gas} + b^2/2\right)n_\mu + (\eta_\nu b^\nu)b_\mu \\ &= (W + \mathcal{B}^2)\tilde{v}_{\mu{\rm gas}} - (\tilde{v}_{\nu{\rm gas}}\mathcal{B}^\nu)\mathcal{B}_\mu \\ &- (-W + p_{\rm gas} - (1/2)\mathcal{B}^2(1 + \tilde{v}^2_{\rm gas}) + (1/2)(\tilde{v}_{\nu{\rm gas}}\mathcal{B}^\nu)^2)\eta_\mu. \end{aligned} \tag{52}$$

Using $\eta_\mu \mathcal{B}^\mu = 0$ and $S \equiv Q_\mu \mathcal{B}^\mu = v_{\mu{\rm gas}}\mathcal{B}^\mu W$, $\eta_\mu \tilde{v}^\mu_{\rm gas} = 0$, and $\mathcal{B}^t = \tilde{v}^t_{\rm gas} = 0$, then the ZAMO energy density is given by

$$\begin{aligned} -E &= \eta^\mu Q_\mu = -W + p_{\rm gas} - \mathcal{B}^2\frac{1 + \tilde{v}^2_{\rm gas}}{2} + \frac{S^2}{2W^2} \\ &= -W + p_{\rm gas} - \mathcal{B}^2\frac{1 + \tilde{v}^2_{\rm gas}}{2} + \frac{(\tilde{v}^k_{\rm gas}\mathcal{B}_k)^2}{2}. \end{aligned} \tag{53}$$

such that

$$Q_\mu = (W + \mathcal{B}^2)\tilde{v}_{\mu{\rm gas}} + E\eta_\mu - (\tilde{v}_{\nu{\rm gas}}\mathcal{B}^\nu)\mathcal{B}_\mu. \tag{54}$$

As discussed in Mignone & McKinney (2007), one can avoid catastrophic cancellation issues in Eq. (53) by using

$$W' = \frac{D\tilde{u}^2_{\rm gas}}{1 + \gamma_{\rm gas}} + \chi_{\rm gas}\gamma^2_{\rm gas} \tag{55}$$

instead of using $W = W' + D$, where $\chi_{\rm gas} \equiv \rho_0\epsilon_{\rm gas} + p_{\rm gas}$ and $\epsilon_{\rm gas} = (\rho_0 + e_{\rm gas})/\rho_0$. Catastrophic cancellations for non-relativistic velocities can be avoided by replacing $\gamma_{\rm gas} - 1$ in any expression with $\tilde{u}^2_{\rm gas}/(\gamma_{\rm gas} + 1)$.

Next, using $j^\mu{}_\nu = \delta^\mu_\nu + \eta^\mu\eta_\nu$, compute the ZAMO momentum

$$\tilde{Q}^\nu \equiv j^\nu{}_\mu Q^\mu = Q^\nu + \eta^\nu(-E) = (W + \mathcal{B}^2)\tilde{v}^\nu_{\rm gas} - (\tilde{v}_{\mu{\rm gas}}\mathcal{B}^\mu)\mathcal{B}^\nu, \tag{56}$$

and, since $u^\mu_{\rm gas}\mathcal{B}_\mu/\gamma_{\rm gas} = \tilde{u}_\mu\mathcal{B}^\mu/\gamma_{\rm gas} = \tilde{v}_{\mu{\rm gas}}\mathcal{B}^\mu = (Q_\mu\mathcal{B}^\mu)/W = (\tilde{Q}_\mu\mathcal{B}^\mu)/W$, one can solve Eq. (56) for

$$\tilde{v}^i_{\rm gas} = \frac{1}{W + \mathcal{B}^2}\left[\tilde{Q}^i + \frac{\left(Q_\mu\mathcal{B}^\mu\right)\mathcal{B}^i}{W}\right] \tag{57}$$

Also, one can obtain

$$\tilde{Q}^2 = \tilde{v}^2_{\rm gas}\left(\mathcal{B}^2 + W\right)^2 - \left(Q_\mu\mathcal{B}^\mu\right)^2\left(\mathcal{B}^2 + 2W\right)\frac{1}{W^2}. \tag{58}$$

that can be solved for

$$\tilde{v}^2_{\rm gas} = \frac{\tilde{Q}^2W^2 + \left(Q_\mu\mathcal{B}^\mu\right)^2\left(\mathcal{B}^2 + 2W\right)}{\left(\mathcal{B}^2 + W\right)^2W^2}. \tag{59}$$

A one dimensional inversion scheme is derived by regarding Eq. (53) as a single nonlinear equation in the only unknown W (or W'). Then one uses Eq. (57) to obtain $\tilde{v}^i_{\rm gas}$, then compute $\gamma_{\rm gas}$, then obtain ρ_0 from the definition of D, then compute $p_{\rm gas}$ from the definition of W. More details are provided in Mignone & McKinney (2007).

4.6 RAD Inversion of Conserved to Primitive Quantities

The radiative inversion is based upon the ZAMO frame, as compared to the lab-frame in Koral. For the radiative inversion using the M1 closure, one can solve for the radiation $P^{n+1}_q(U^{n+1}_q)$ analytically when given the radiative conserved quantities U^{n+1}_q.

First, we let $p_{\rm rad}(e_{\rm rad}) = e_{\rm rad}/3$ (as for an ideal gas with $\Gamma = 4/3$), $\gamma_{\rm rad} = \sqrt{1 + g_{ij}\tilde{u}^i_{\rm rad}\tilde{u}^j_{\rm rad}}$, $\tilde{u}^\mu_{\rm rad} = u^\mu_{\rm rad} - \gamma_{\rm rad}\eta^\mu$, $\tilde{v}^\mu_{\rm rad} = \tilde{u}^\mu_{\rm rad}/\gamma_{\rm rad}$, and $v^\mu_{\rm rad} = u^\mu_{\rm rad}/\gamma_{\rm rad}$, so that $\tilde{v}^2_{\rm rad} = v^2_{\rm rad} + 2\gamma_{\rm rad} - 1$, and $W_{\rm rad} \equiv 4p_{\rm rad}\gamma^2_{\rm rad}$. For M1's $R^\mu{}_\nu = p_{\rm rad}(4u^\mu_{\rm rad}u_{\nu{\rm rad}} + \delta^\mu_\nu)$, then

$$\begin{aligned} U_\mu &= -R^\nu{}_\mu\eta_\nu = \alpha R^t{}_\mu \\ &= p_{\rm rad}(4\gamma_{\rm rad}u_{\mu{\rm rad}} - \eta_\mu) = W_{\rm rad}\tilde{v}_{\mu{\rm rad}} - (-W_{\rm rad} + p_{\rm rad})\eta_\mu, \end{aligned} \tag{60}$$

and

$$\begin{aligned} -E_{\rm rad} &= -R^\nu{}_\mu\eta_\nu\eta^\mu = U_\mu\eta^\mu = \alpha R^t{}_\mu\eta^\mu \\ &= -p_{\rm rad}(4\gamma^2_{\rm rad} - 1) = -W_{\rm rad} + p_{\rm rad}, \end{aligned} \tag{61}$$

so that $p_{\rm rad} = -E_{\rm rad} + W_{\rm rad}$ and

$$U_\mu = W_{\rm rad}\tilde{v}_{\mu{\rm rad}} + E_{\rm rad}\eta_\mu, \tag{62}$$

and

$$\begin{aligned} \tilde{U}^\mu &= j^\mu{}_\nu U^\nu = (\delta^\mu_\nu + \eta^\mu\eta_\nu)U^\nu = U^\mu + \eta^\mu(-E_{\rm rad}) \\ &= W_{\rm rad}(v^\mu_{\rm rad} - \eta^\mu) = W_{\rm rad}\tilde{v}^\mu_{\rm rad}, \end{aligned} \tag{63}$$

such that

$$U^2 = W^2_{\rm rad}v^2_{\rm rad} - p^2_{\rm rad} + 2p_{\rm rad}W_{\rm rad} \tag{64}$$

and

$$\tilde{U}^2 = W^2_{\rm rad}\tilde{v}^2_{\rm rad}. \tag{65}$$

One could solve Eq. (61) for $W_{\rm rad}$ using an iterative approach. After obtaining a sufficiently accurate $W_{\rm rad}$, one obtains the primitives from $\tilde{v}^\mu_{\rm rad}$ from Eq. (63), then compute $\gamma_{\rm rad}$, then obtain $p_{\rm rad}$ from the definition of $W_{\rm rad}$.

The M1 radiation inversion can be treated analytically (Sądowski et al. 2013c), where we solve these equations differently than in Koral. First, one has

$$E_{\rm rad} = p_{\rm rad}(4\gamma^2_{\rm rad} - 1) \tag{66}$$

and

$$\tilde{U}^\mu = 4p_{\rm rad}\gamma^2_{\rm rad}\tilde{v}^\mu_{\rm rad}. \tag{67}$$

Solving these equations for $p_{\rm rad}$ and $\tilde{v}^\mu_{\rm rad}$ (via $\tilde{v}^2_{\rm rad}$ or $\gamma^2_{\rm rad}$) gives

$$p_{\rm rad} = \frac{E_{\rm rad}}{4\gamma^2_{\rm rad} - 1} \tag{68}$$

and

$$\tilde{v}^\mu_{\rm rad} = \frac{\tilde{U}^\mu(4\gamma^2_{\rm rad} - 1)}{4E_{\rm rad}\gamma^2_{\rm rad}} = \frac{\tilde{U}^\mu}{4p_{\rm rad}\gamma^2_{\rm rad}} \tag{69}$$

where the correct root to choose is

$$\gamma^2_{\rm rad} = \frac{2 - y + \sqrt{4 - 3y}}{4(1 - y)}, \tag{70}$$

where

$$y \equiv \frac{\tilde{U}^2}{E^2_{\rm rad}}, \tag{71}$$

which is only allowed to range from $y = 0$ to $y = 1$ for $\gamma_{\rm rad} = 1$ to ∞, respectively.

Note that $\tilde{Q}^\mu + \tilde{U}^\mu$ and $E + E_{\rm rad}$ are constant, so any instance of $E_{\rm rad}$ or $\tilde{U}^\mu$ can be replaced by the total value minus the MHD value. So, any occurrence of $\gamma_{\rm rad}$ can be written in terms of quantities only dependent upon MHD variables, and so $p_{\rm rad}$ (and so $W_{\rm rad}$) and $\tilde{v}^\mu_{\rm rad}$ can be similarly written. One needs to have some means to ensure that $0 \leqslant y \leqslant 1$ and $p_{\rm rad} \geqslant 0$.

We have three approaches to limiting the radiation when $E_{\rm rad} \leqslant 0$ or $0 < y \gtrsim 1$. The "BASIC" limiter forces $\bar{E} = 10^{-300}$ and $\underline{\tilde{u}}^i = 0$ when $E_{\rm rad} \leqslant 0$, $\underline{\tilde{u}}^i_{\rm rad} = 0$ when $0 > y > -\epsilon_m$ for machine precision ϵ_m, and if $y \geqslant y_{\rm max}$ then relative 4-velocities are rescaled to ensure $y = y_{\rm max}$ corresponding to a $\gamma_{\rm max}$ via Eq. (70). The "TYPE1" and "TYPE2" limiters are similar, except if $y > y_{\rm max}$, then $U_{\rm abs} = (1/2)(\sqrt{|\tilde{U}^2|} + |E_{\rm rad}| + 10^{-150})$ and $\underline{\tilde{u}}^i = \gamma \tilde{U}^i / U_{\rm abs}$ is first set, and then this is rescaled to give the desired $\gamma_{\rm rad,max}$. If "TYPE2" or if "TYPE1" with an original $y > 1 - 100\epsilon_m$, then we solve for $E_{\rm rad} = 10^{-150} + \sqrt{\tilde{U}^2 / y_{\rm max}}$ then obtain $p_{\rm rad}$ and $\bar{E}$ as usual. If using "TYPE1", then we check whether this $\bar{E}$ is larger than the original estimate, and if so we use the smaller value. In summary, the "BASIC" limiter is the most conservative for an actual solution to use during the evolution since it helps avoids run-away energy gains. However, for a smooth Newton stepping, "TYPE2" is best since it avoids drop-outs to small $\bar{E}$ that would cause the Newton stepping difficulties and failure to recover the Newton stepping.

4.7 Implicit radiative source terms

To find an implicit solution (i.e. when Eq. (29) has U^i on the left-hand side and M^i on the right hand side for the same i in the IMEX scheme), we use a 4D Newton scheme on a subset of the equations of motion. This is possible because of the constraint provided by total energy-energy momentum conservation between the gas and fluid in a given cell. We avoid a fully implicit scheme (e.g., Krumholz et al. 2007; Jiang et al. 2012), which would require us to use a more expensive 8D Newton scheme (to include geometry source terms and expensive multi-cell Riemann flux differences and spatial interpolations within the Newton solver).

We numerically solve one of the following two equations

$$T^t_{\nu,(i+1)} - T^t_{\nu,(i)} = \Delta t \, G_{\nu,(i+1)}, \tag{72}$$

$$R^t_{\nu,(i+1)} - R^t_{\nu,(i)} = -\Delta t \, G_{\nu,(i+1)}, \tag{73}$$

where for the IMEX scheme, i corresponds to all explicit contributions (i.e. initial+flux+geometry+explicit radiation), while $i+1$ contains all implicit contributions (i.e. implicit radiation). When solving the first equation, we find updates to $R^{\mu\nu}$ via the constraint that $T^t_{\mu,(i+1)} = T^t_{\mu,(i)} - \Delta R^t_{\mu,(i)}$ with $\Delta R^t_{\mu,(i)} = (R^t_{\mu,(i+1)} - R^t_{\mu,(i)})$. When solving the second equation, we find updates to $T^{\mu\nu}$ via the constraint that $R^t_{\mu,(i+1)} = R^t_{\mu,(i)} - \Delta T^t_{\mu,(i)}$ with $\Delta T^t_{\mu,(i)} = (T^t_{\mu,(i+1)} - T^t_{\mu,(i)})$.

In cases when the energy-momentum conservation gives no solution or $e_{\rm gas} < 0$, then we replace the energy equation

$$T^t_{t,(i+1)} - T^t_{t,(i)} = \Delta t \, G_{t,(i+1)}, \tag{74}$$

with the entropy equation

$$[S u^t]_{(i+1)} - [S u^t]_{(i)} = \Delta t \, G_{S,(i+1)}, \tag{75}$$

while if also the entropy has no solution, we ignore energy and entropy conservation (cold MHD limit).

Note that $\rho_0 u^t_{\rm gas}$ is constant for the implicit equations, so its addition to T^t_t does not modify changes in R^t_t when computing ΔR^t_t or modify the value of G_μ.

4.8 Implicit Solver Methods

We use a Newton method to solve these energy/entropy/cold MHD equations and estimate the Jacobian matrix numerically.

When the gas dominates the radiation or visa versa, then the finite machine precision in the dominant fluid component can lead to arbitrarily large numerical changes in the sub-dominant fluid component. E.g., when $|R^t_t| \gg |\rho_0 u^t_{\rm gas} + T^t_t|$ or $e_{\rm gas} \gg \widehat{E}$ and under other conditions, one should iterate the sub-dominant gas-fluid quantities. Further, one can choose to iterate conserved quantities or primitive quantities in the implicit solver. HARMRAD obtains the best solution out of iterating one of four sets of quantities: R^t_μ, T^t_μ, $e_{\rm gas}, \tilde{u}^i_{\rm gas}$, or $\bar{E}, \tilde{u}^i_{\rm rad}$.

For each of the four sets of iterated quantities one requires different steps to be taken to determine the error function that enters into the Newton method.

For the method based upon iterating R^t_μ (called URAD), the steps are:

- Set $\Delta T^t_\mu = -\Delta R^t_\mu$.
- Compute G_s using prior primitives (P_n) to compute G_μ and $T_{\rm gas}$.
- Perform an inversion from conserved quantities (latest solution for $T^t_{\mu,(i+1)}, R^t_{\mu,(i+1)}$) to gas+radiation primitives (latest solution for P_{i+1})
- Recompute all conserved quantities from P_{i+1} for consistency (in case of inversion failure/modification of solution).

This method requires an expensive Newton-inside-Newton calculation as well as a numerical Jacobian that itself requires 4 MHD inversions per overall Newton step. That numerical Jacobian is computed with a one-sided difference with a fixed difference size, which is prone to arbitrarily large errors (see numerical recipes). A centered difference would be more accurate, but then 8 MHD inversions would be required per Newton step. Also, this method is unable to obtain an accurate entropy source term (although it will eventually converge), and iterating R^t_μ can directly lead to out-of-bounds values leading to no solution for the inversion to radiation primitives.

For a method based upon iterating T^t_μ (called UMHD), the steps are:

- Set $\Delta R^t_\mu = -\Delta T^t_\mu$.
- Compute G_s using prior primitives (P_n) to compute G_μ, u^μ, and $T_{\rm gas}$.
- Perform an inversion from conserved quantities (latest solution for $T^t_{\mu,(i+1)}, R^t_{\mu,(i+1)}$) to gas+radiation primitives (latest solution for P_{i+1})
- Recompute all conserved quantities for consistency.

This method is unable to obtain an accurate entropy source term (although it will eventually converge), and iterating T^t_μ can directly lead to out-of-bounds values leading to no solution for the inversion to gas primitives.

For a method based upon iterating $S u^t, T^t_i$ (called ENTROPY-UMHD), the steps are:

- Invert $S u^t, T^t_i$ to gas primitives (latest gas variables in P_{i+1})
- Recompute full T^t_μ.
- Set $\Delta R^t_\mu = -\Delta T^t_\mu$.
- Invert R^t_μ to radiation primitives (latest radiation variables in P_{i+1}).
- Recompute R^t_μ for consistency.

This method obtains an accurate entropy source for each implicit

step, but like the UMHD method, it iterating T^t_i can directly lead to out-of-bounds values leading to no solution for the inversion to gas primitives.

For a method based upon iterating the radiation primitives $(\bar{E}, \tilde{\underline{u}}^\mu_{\rm rad})$ (called PRAD), the steps are:

- Compute R^t_μ from radiation P_{i+1}.
- Estimate G_S using prior primitives (P_n) to compute G_μ, u^μ, and $T_{\rm gas}$.
- Set $\Delta T^t_\mu = -\Delta R^t_\mu$.
- Invert T^t_μ to gas primitives (latest gas variables in P_{i+1}).
- Recompute T^t_μ for consistency.

This method estimates G_S and is slow as the UMHD method, but it at least does not iterate out of bounds like the URAD method. However, it cannot be used when the gas is very sub-dominant due to machine precision issues.

For a method based upon iterating the gas primitives $(e_{\rm gas}, \tilde{\underline{u}}^\mu_{\rm gas})$ (called PMHD), the steps are:

- Obtain $\rho_0 = U_1/u^t$ from the newly updated P_{i+1}.
- Compute $S\,u^t, T^t_\mu$ from gas P_{i+1}.
- Set $\Delta R^t_\mu = -\Delta T^t_\mu$.
- Invert R^t_μ to radiation primitives (latest radiation variables in P_{i+1}).
- Recompute R^t_μ for consistency.

This method has none of the flaws mentioned in the previous methods and is fast because the radiation inversion is analytic and simple. Its only flaw is that it cannot be used when the radiation is very sub-dominant due to machine precision issues.

Now, after one (or all) of these methods are used, we have consistent values for U_q and P_q from which we can compute an error function required by the Newton method. So, the next steps are:

- Compute 4-force $G_{\mu,(i+1)}(P_{q,(i+1)})$.
- Compute the error function for each type of variable as $E_q = (U_{q,(i+1)} - U_{q,(i)})F_q + dtS_qF_q$.
- Compute the normalized error e_q, by dividing by sum of absolute value of any signed terms that appear in E_q and all its sub-expressions. For each gas and radiation terms, spatial norms are merged in an orthonormal basis to form a single spatial norm for all dimensions.

For the q conserved/primitive quantities, a similar set of extra factors $F_q = \{1, 1, 1, 1, 1, 1, T_{\rm gas}\}$ multiply the overall error function. The temperature is factored into the entropy equation using F_{13} in order to generate a more regular/linear functional behavior near roots to make it easier to find the solution, as found experimentally using HARMRAD and test code in Mathematica using both an analytical and numerical Jacobian. Also, for this entropy term with the $T_{\rm gas}$ factor, we include in the norm the energy norm, which helps normalize the error in $T_{\rm gas}dS$.

The "total normalized error" is computed as

$$e_T = (1/4)\sum_q e_q, \tag{76}$$

which is computed over all quantities to produce an error independent of the method or iterated quantities used as well as to account for the error in the un-iterated quantities that could be large despite small iterated quantities in different regimes. The "iterated normalized error" is computed from iterated quantities as

$$e_I = (1/4)\sum_{q_k} e_{q_k}, \tag{77}$$

over only those q's that were iterated (q_k's). E.g., $k = 2, 3, 4, 5$ in U_k for the UMHD method, $k = 9, 10, 11, 12$ in U_k for the URAD method, and the same k's in P_k for each of the PMHD and PRAD methods, respectively. For the energy methods, entropy is ignored in the error. For entropy methods, energy is ignored. For cold MHD methods, both energy and entropy errors are ignored. This generates the appropriate total and iterated error for each method.

Once the solution for $U_{q,(i+1)}$ is obtained, the implicit radiation source term is given by

$$\mathrm{SR}_{q,(i+1)} = \frac{1}{dt_i}(U_{q,(i+1)} - U_{q,(i)}) \tag{78}$$

for each implicit Runge-Kutta sub-step of size dt_i. This then provides all terms required for the radiation GRMHD method to complete a single Runge-Kutta sub-step.

4.9 4D Newton-Raphson Scheme

The implicit solver involves computing the $(k+1)$-th approximation to a set of iterated dependent variables $\boldsymbol{x}$ using a Newton-Raphson method. For the various methods, the iterated quantities are one of the q = 1–13 quantities in the list of quantities given by $\tilde{U}_q = U_q/\sqrt{-g} = \{\rho_0 u^t, \rho_0 u^t_{\rm gas} + T^t{}_t, T^t{}_i, B^i, R^t{}_\nu, S\,u^t\}$. For the energy-based or entropy-based URAD,UMHD,PRAD,PMHD methods, we iterate $\{\tilde{U}_{9,10,11,12}, \tilde{U}_{2,3,4,5}, P_{9,10,11,12}, P_{2,3,4,5}\}$, respectively. The cold MHD based method simply uses a reduced 3D method with iterated quantities from one of $\{\tilde{U}_{10,11,12}, \tilde{U}_{3,4,5}, P_{10,11,12}, P_{3,4,5}\}$. The error function is independent from the iterated quantities, and for each energy-based URAD,UMHD,PRAD,PMHD methods, the error function quantities are one of $\{\tilde{U}_{9,10,11,12}, \tilde{U}_{2,3,4,5}, \tilde{U}_{9,10,11,12}, \tilde{U}_{2,3,4,5}\}$, respectively, while for each entropy-based URAD,UMHD,PRAD,PMHD methods, the error function quantities are one of $\{\tilde{U}_{13,10,11,12}, \tilde{U}_{13,3,4,5}, \tilde{U}_{13,10,11,12}, \tilde{U}_{13,3,4,5}\}$, respectively, while for the cold MHD based URAD,UMHD,PRAD,PMHD methods, the error function quantities are one of $\{\tilde{U}_{10,11,12}, \tilde{U}_{3,4,5}, \tilde{U}_{10,11,12}, \tilde{U}_{3,4,5}\}$, respectively. Then, the Newton update is obtained via

$$\boldsymbol{x}^{(k+1)} = \boldsymbol{x}^{(k)} - D\boldsymbol{E}(\boldsymbol{x}) \cdot \left(\frac{\partial \boldsymbol{E}(\boldsymbol{x})}{\partial \boldsymbol{x}}\right)^{-1} |_{\boldsymbol{x}=\boldsymbol{x}^{(k)}}. \tag{79}$$

for damping factor D.

The Newton step requires computation of the Jacobian $\partial \boldsymbol{E}/\partial \boldsymbol{x}$, which is simply obtained as a finite difference of the error function away from a reference value of x from the latest estimate of P_{i+1} or U_{i+1}. A one-sided finite difference (using reference and an offset) is used for URAD,PRAD due the expense of the error function requiring the 1D MHD inversion, while the UMHD,ENTROPYUMHD,PMHD methods use a two-sided finite difference (using two offsets away from the reference value) if the "stages" approach (see below) is used. A fixed normalized error offset of 10^{-8} is used, until e_I from Eq. (77) drops below 10^{-9} in which case a normalized error offset of 10^{-10} is used. If the Jacobian calculation hits a conserved to primitive inversion failure, larger or smaller offsets are attempted until no inversion problem occurs up until a normalized error offset of 0.3. Any MHD inversions for the Jacobian are computed with a tolerance of 10^{-2} times the Jacobian difference used, since any more accuracy is wasted in the finite difference. Any RAD inversions for the Jacobian use the TYPE2 limiter on the inversion, which avoids both offsets giving the same f (and so singular inversion) when otherwise the BASIC or TYPE1 limiters would lead to $\bar{E} \to 0$ as the solution.

4.10 Quickly Choosing Optimal Implicit Solution

In total there are 6 Newton methods for each energy and entropy based methods, while there is a single cold MHD method. Arbitrary use of all these approaches would be costly, so one needs to estimate which is optimal to use to get the smallest error in the shortest time.

First, we consider quantities: (1) energy gas vs. radiation values of $U_{q,i}$, (2) energy gas vs. radiation values of $\Delta_r U_q = (U_{q,i} - U^n_q)/(|U_{q,i}| + |U^n_q|)$, and (3) $e_{\rm gas}$ vs. $\widehat{E}$. If any of the radiation versions of these quantities have absolute magnitudes smaller than $10\epsilon_m$, then we assume the radiation is in an "extreme radiation sub-dominant regime" that the numerical machine precision errors in gas conserved quantity calculations will ruin the ability to find an implicit solution. Hence, in this situation, we first try the URAD/PRAD methods. Otherwise, we use no other pre-conditions to control the order of the method attempted, and in particular we otherwise first use the fastest PMHD method as described next.

To optimize performance, a "normal" Newton method for a maximum of 20 steps is attempted first using the fast energy-based PMHD method as the first attempted iterate/error choice, then the URAD method is attempted if the PMHD solution is unacceptable, then the PRAD method is attempted if the URAD solution is unacceptable. Newton steps are undamped ($D = 1$), although damping has been found to help seek errors closer to machine precision and to avoid cycle behaviors, at greater computational cost. For the PRAD,URAD methods, the total number of MHD inversion steps is also monitored and not allowed to go beyond 20×6 total steps to avoid excessive steps.

Then, the PMHD, URAD, PRAD methods are attempted using a "stage" approach that takes (stage 1) one momentum-only Newton step, then (stage 1) converges using energy-only Newton stepping, then (stage 3) seeks the full 4D solution for a maximum of 40 steps. For this "staged" approach, the Newton steps are damped by a factor of $D = 1/2$ for the first momentum step, $D = 1/2$ for the first energy step, and $D = 1/4$ for the first full 4D step. This avoids large changes when transitioning to using a different set of equations to step. The "staged" approach is avoided if the radiation is not in the "extreme radiation sub-dominant regime," described already. The total number of MHD inversion steps is limited to 40×6 total steps to avoid excessive steps.

The guess for the Newton method, for any attempted method, is set as the solution from the previous attempt with the smallest error (e_T) as long as that previous attempt gave a solution with $e_T < 10^{-4}$. If no prior guess exist or have $e_T < 10^{-4}$, then the prior primitives P_n are used as the guess. For the PRAD method, that simple guess is modified by first finding P from $U_{q,i}$ given in Eq. (29) that describes some "optically thin" limit for the primitive solution as if there were no source term. Then, the optical depth τ is computed from P_n, and if $\tau < 2/3$, then that "optically thin limit" primitive is set as the guess. Otherwise, the prior primitive P^n corresponding to U^n_q is used. For the PMHD method, similarly, P is obtained from an MHD inversion of $U_{q,i}$ (using MHD inversion tolerance of 10^{-9}) and used if $\tau < 2/3$, otherwise P^n is used. For the PMHD method, the "stage" guess for $e_{\rm gas}$ is further modified as an inversion from the conserved entropy Su^t per unit conserved mass $\rho_0 u^t_{\rm gas}$ to give a specific entropy $s_{\rm gas}$ that together with the previous density ρ_0 is used to obtain an estimate of $e_{\rm gas}$. This helps avoid issues with stepping when the initial guess for $e_{\rm gas}$ is too small and leads to a guess for the 4-force that is large.

For the first step and after each step, the error is computed using the TYPE2 limiter when computing the radiation inversion. If the limiter was activated because the radiation energy was negative, then the error excludes the energy term (or entropy term for the entropy-based methods) in the error function. The TYPE2 limiter then ensures the radiation momentum is unchanged, so momentum can continue to be monitored. If this leads to an inversion error, then the step is backed-up half-way until it succeeds for 20 attempts.

Then, we perform pre-step checks. We check if the error is already small, and if so break before computing the Jacobian or step. We also check to see (for steps beyond the 5th full 4D type step) that the error is dropping fast enough (dropping by 0.5) compared to the average of 3 steps starting from 5 steps to 2 steps ago. Each of the total and iterated errors must satisfy this requirement or the iterations are stopped to save computational expense when no improvements are being made in the error. Another pre-step check is to see if the error is repeatedly rising, by checking whether the error has risen (instead of dropped) 5 times starting after the 5th full 4D type step. Once the error has risen that many times, the iterations are dropped to avoid computational expense.

The Newton step is then taken for either U or P using Eq. (79).

Then we perform post-step checks. If $e_{\rm gas} < 0$ for PMHD,UMHD methods or $\bar{E} < 0$ for URAD,PRAD methods, then each $e_{\rm gas}$ or $\bar{E}$ are set to 0.5 of their absolute magnitudes. This helps do a one-sided bisection down to small values. If this modification occurs 2 times for the "staged" momentum steps or "staged" energy steps for the energy-based method or 4 times for the "staged" momentum steps or "staged" energy steps for the entropy-based methods, then the prior value is held and the next "stage" in the stages approach is attempted. Another post-step check is we count to see if $e_{\rm gas} < 0$ for the URAD,PRAD methods more than 3 times. In that case, we assume another method or the entropy-based method are more appropriate and stop the iterations.

For each attempt, the iterations are stopped and Newton method aborted if any of the following occurs:

(i) the "total normalized error" e_T from Eq. (76), falls below a tolerance of tol $= 10^{-12}$ for the PMHD,UMHD methods or tol $= 10^{-9}$ for the URAD,PRAD methods.
(ii) the residual $\left|\boldsymbol{x}^{(k+1)}/\boldsymbol{x}^{(k)} - 1\right|$ falls below $10\epsilon_m$.
(iii) a maximum number of Newton steps is hit (chosen independently for each method given each of their performance issues).

In any case, for a given attempt, a final error is computed based on the last step, and the best solution (with the smallest total error) is used as the solution. Lastly, when using the PMHD, UMHD, or ENTROPYUMHD methods, if that best solution used the TYPE2 limiter and encountered a negative radiation energy density, then the radiative inversion is recomputed using the BASIC limiter. This ensures that while we chose the best solution possible, the actual solution used reduces the radiation primitives to $\bar{E} \sim 0$ to avoid run-away energy gains.

In any case, if the attempted tolerance is not met, an error of $e_T < 10^{-9}$ is considered acceptable regardless of the attempted error and no further attempts at using other methods are made. An error of $e_T > 10^{-9}$ is considered not quite acceptable, in which case the next method in line is attempted to seek a smaller error. The solution with the lowest error over all steps and methods used is taken as the energy-based solution.

4.11 Backup solvers/solutions when Implicit Energy solver Fails

If the energy-based method fails to obtain the required error or if the energy-based solution gives $e_{\rm gas} < 0$, then the entropy-based

methods are attempted in the same sequence as the energy-based methods (the ENTROPYUMHD method is currently not used). As with the energy-based method, the entropy solution with the lowest error over all steps and methods used is taken as the entropy-based solution.

If the entropy method fails and the energy method gives $e_{\rm gas} < 0$ or if both energy and entropy methods fail, then we consider using the cold MHD equations. Let $t^t_\mu = T^t_\mu + \rho_0 u^t_{\rm gas}$, then the cold MHD solver is only attempted if $e_{\rm gas} < 0.1\rho_0|\underline{u}^i\underline{u}_i|$, and $|t^t_t t^{tt}| < 0.1|t^t_i t^{ti}|$, and $|R^t_t R^{tt}| < 0.1|R^t_i R^{ti}|$. Only the PMHD method is used. The final value of $e_{\rm gas}$ is spatially averaged over neighbors that had good energy or entropy inversions, or averaged over all bad neighbors if no good neighbors exist.

The stages, entropy, and especially cold backup methods are used rarely, but they help avoid lack of inversion.

No solution is considered to be when the total error is $e_T > 10^{-7}$, as experimenting shows that beginning around 10^{-4} or so, such a large error can imply a static solution with no changes when evolution should occur. When none of energy, entropy, or cold MHD methods meet this tolerance, then diffusive back-up methods are used. In this very rare case where none of these find an acceptable solution, then the radiative source term is temporarily updated explicitly using backup inversion methods as in HARM for the gas quantities, but then the full set of primitives is spatially averaged over neighbors that had a good inversion. If no good neighbors exist for a point, then averages are performed over all neighbors, but this happens in none of the tests considered in this paper. Note that using static values (rather than averages) as a final backup method can lead to catastrophic evolution because then (e.g.) the induction equation (that must evolve the magnetic field in order to preserve the solenoidal constraint) is an simple differential equation for a constant v^i that gives an exponentially growing B^j.

In cases where a solution is acceptable but has too small $\rho_0, e_{\rm gas}$, we use the numerical floor approach described in McKinney et al. (2012). The only constraint on $\bar{E}$ is that it is forced to be positive by setting it to 10^{-150} if it was non-positive.

In our experimentation with explicit sub-cycling as an alternative/backup to the implicit inversion, some conditions to use subcycle methods were experimented with, but nothing was found to be generally applicable in all regimes. So sub-cycling was completely abandoned in favor of the implicit method.

5 TEST PROBLEMS

We consider several radiative tests to ensure the numerical method is accurate, robust, and fast. Our goal is not to have exceptionally sharp discontinuities or noise-less solutions by tweaking the numerical method used for each test, but rather our goal is to use a high-resolution interpolation scheme and ensure the noise or issues are manageable so we understand how the code would operate when used to study general problems involving magnetized accretion flows around black holes. So we accept some noise and study under what extreme situations that noise appears.

Non-radiative tests were performed in Gammie et al. (2003) and so are not considered in this paper. Most of the radiative tests are based on test problems from Sądowski et al. (2013c,a). We extend this set by considering a larger physical parameter space in linear wave convergence tests (section 5.1), MHD radiative Bondi flow (section 5.11), and for the first time present a fully 3D radiation GRMHD simulation of a disk-jet accretion system.

We used fixed numerical parameters for all tests and the fiducial 3D simulation in section 6, but all tests use LAXF except the double shadow test (see section 5.7) uses HLL (we discuss the minor LAXF issues with this test). We use a maximum radiative Lorentz factor of $\gamma_{\rm rad,max} = 100$ (or twice larger than the injected beam's value for tests that inject higher $\gamma_{\rm rad}$), 3rd order Runge-Kutta method (RK3), LAXF flux, PPM reconstruction, and Courant factor $C = 0.49999$. Note that using a lower-order reconstruction like MINM or MC leads to more diffusion and does not stress the method as much as using PPM, while PPM can lead to some additional grid-scale artifacts. Also, we use a 3rd order Runge-Kutta with $C \sim 1/2$ in order to more generally handle cases where the gas temperature is low, giving a relatively low internal energy density compared to the kinetic or magnetic energies. None of these tests exhibit any implicit solver failures.

5.1 Radiation modified MHD linear waves in 1D Cartesian Minkowski

First, we test the accuracy with which our numerical scheme propagates linear MHD waves in the presence of radiation. As waves propagate through the gas, their interactions with the photon field feed back into the gas and modify the nature of the perturbations themselves relative to the non-radiative case. Making sure that this interaction is correctly captured in the numerical scheme and that the numerical solution converges to the analytical solution at the expected order is a stringent test of the numerical method. We will consider sound, slow, and fast waves. We do not consider Alfvén waves because they are less affected by radiative effects (Jiang et al. 2012).

For each of the tests, we initialize a single eigenmode, of form

$$q^i = Re\left[q^i_a + \delta q^i e^{i(\omega t - kx)}\right], \tag{80}$$

with eigenvectors δq^i given in Table 1 and computed using the method described in Sądowski et al. (2013a). Here $Re\,(\dots)$ indicates the real part of a variable. The ambient background medium is uniform, of density $\rho_a = 1$ and sound speed $c_{\rm s,a} = 0.1$. This corresponds to gas internal energy, $e_{\rm gas,a} = \rho[\Gamma(\Gamma-1)c^{-2}_{\rm s,a} - \Gamma]^{-1} = 0.009137055837563452$, and the thermal pressure of the ambient gas, $p_{\rm gas,a} = (\Gamma-1)e_{\rm gas}$, where we choose $\Gamma = 5/3$. The ambient medium is at rest ($v^x_a = v^y_a = 0$), and the radiation flux in the fluid frame vanishes $\widehat{F}^x_a = \widehat{F}^y_a = 0$. For sound waves we set all magnetic field components to zero, whereas for slow and fast waves, we set $B^x_a = B^y_a = B_0 = 0.10075854437197568$ (see Table 1 and Sądowski et al. 2013a).

We carry out the simulations on a 1D domain, $0 \leqslant x \leqslant 1$, however, we allow for velocities and magnetic fields in the $y-$direction. We use periodic boundary conditions in the x-direction. We consider a wavenumber $k = 2\pi$ such that one wavelength fits in the domain. We set the absorption opacity to zero, $\kappa_{\rm abs} = 0$. We vary the scattering opacity given by the optical depth of the domain, $\kappa_{\rm es} = \tau$, and set the radiation pressure via a dimensionless parameter, $\mathbb{P} = p_{\rm rad,a}/p_{\rm gas,a}$ (see Table 1).

After one period of the wave, i.e., $P = 2\pi/Re\,(\omega)$, the numerical solution, $\rho^j_0(t = P)$, deviates from the analytic solution, $\rho^j_{0,\rm A}(t = P)$, which is given by eq. (80). We measure this deviation using L_1 norm:

$$L_1 = N^{-1}\sum_j \left|\rho^j_0 - \rho^j_{0,A}\right|, \tag{81}$$

where the summation is carried out over all of the N grid cells. Figure 1 shows convergence of our scheme in four panels, with

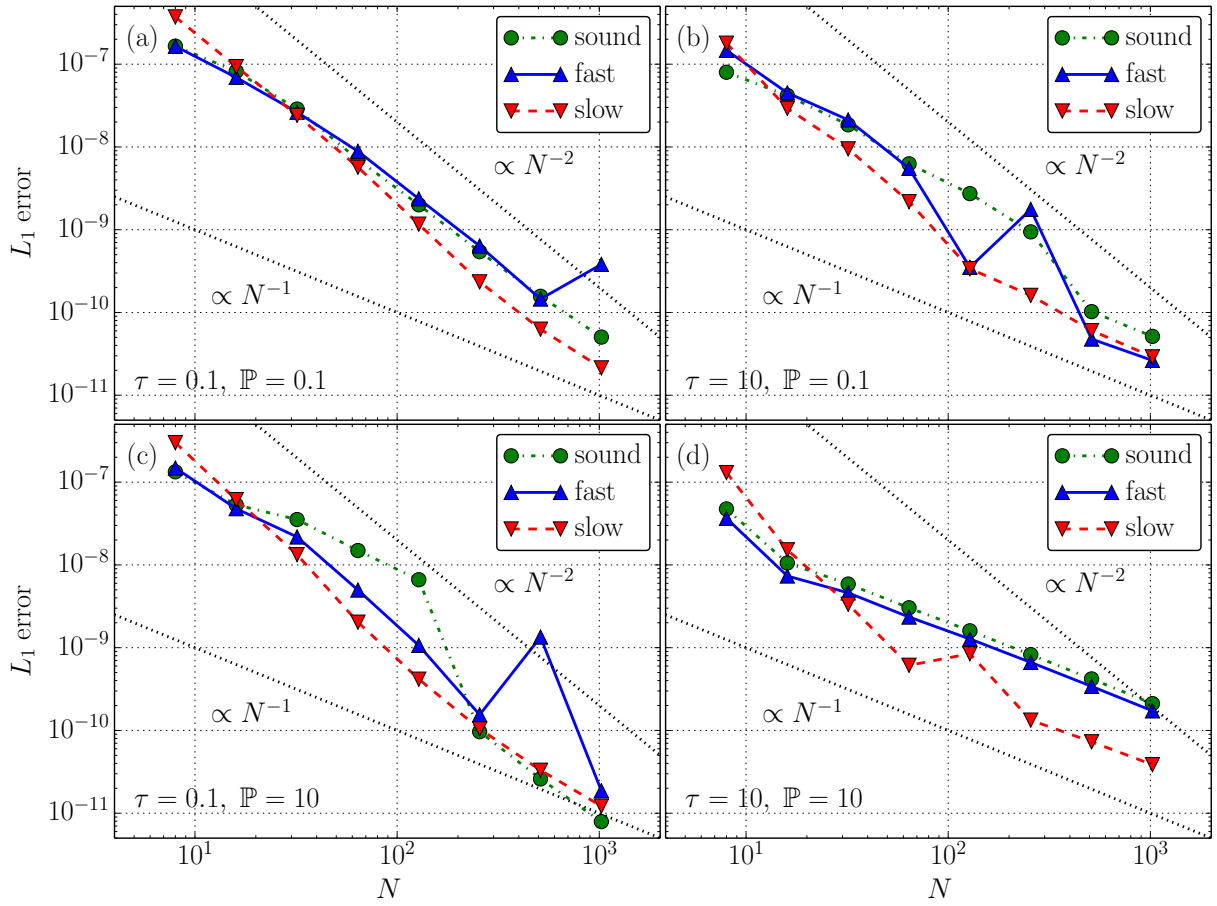

Figure 1. Spatial convergence rate of the radiation modified MHD linear waves. Similar to Table 1, the four panels in this table show eigenmodes of linear waves: top row of panels [panels (a) and (b)] shows gas-dominated and bottom row of panels [panels (c) and (d)] radiation-dominated systems; left column of panels [panels (a) and (c)] shows optically-thin and right column of panels [panels (b) and (d)] optically-thick systems. Numerical results for sound waves are shown with green circles, fast waves with blue triangles, and slow waves with red inverted triangles. The black dotted lines show quadratic and linear convergence. Summarizing, the code converges at the expected rate, although PPM leads to some non-monotonic convergence that does not occur with MINM or MC limiters.

each panel demonstrating the convergence of the eigenmodes given in the corresponding panel in Table 1. As seen in Fig. 1(a),(c), in the optically-thin case, $\tau = 0.1$, the numerical solution converges to the analytic solution at 2nd order, as expected. (Note that PPM leads to some non-monotonic convergence that does not occur with MINM or MC limiters.) As is clear from Fig. 1(b), higher optical depth simulations converge at 2nd order at low and moderate resolutions and switch over to 1st order convergence at high resolutions. Thus, the radiation component of the code, which is treated implicitly and converges at 1st order, affects the overall convergence rate at $\tau \gg 1$. As expected, Fig. 1(d) demonstrates that radiation-dominated optically-thick case converges at first order.

5.2 HD Radiative Shocks in 1D Cartesian Minkowski

For our next test, we set up a number of radiative shock tube problems as described in Farris et al. (2008) and Roedig et al. (2012). The system begins with gas in two different states (left and right), separated by a membrane. The membrane is removed at $t = 0$ and the system is allowed to evolve. The left- and right-states of all the tests except test No. 5 are set up in such a way that the shock asymptotically becomes stationary (see Appendix C of Farris et al. 2008).

Table 2 lists the parameters describing the initial states of seven test problems that we have simulated. The scattering opacity in all the tests is set to zero, so $\kappa_{\rm tot} = \kappa_{\rm abs}$. The value of the radiative constant $\sigma_{\rm rad} = a_{\rm rad}c/4$ in code units is given in the table. All the tests were solved on a grid of 800 uniformly spaced points and evolved till $t = 300$ for all tests except No. 5 that is run till $t = 13$. The M1 closure was used, while prior work used the Eddington approximation, but this only leads to minor differences right at the shock in the fluid-frame radiative fluxes.

Fig. 2 shows the numerical solution for radiative shock tube problem No. 1, which corresponds to a non-relativistic strong shock. This plot can be compared to the corresponding figures and analytical solutions provided elsewhere (Farris et al. 2008; Zanotti et al. 2011; Fragile et al. 2012). The agreement is good, except for a slight smoothing of the numerical profiles at the position of the shock (see the bottom panel). Also, the shock shows some oscillations that lead to a mild bump to the right of the shock in rest-mass density by the end of the simulation. Lower-order MINM and even DONOR cell reconstruction, any other Runge-Kutta method, and both LAXF and HLL lead to the same/similar bump, so PPM or RK3 or LAXF/HLL are not the origin of the bump.

Fig. 3 shows results for radiative shock tube test No. 2, which corresponds to a mildly relativistic strong shock. Again, the agree-

Table 1. Eigenmodes of linear waves. Top row, panels (a) and (b), shows gas-dominated and bottom row, panels (c) and (d), radiation-dominated systems; left column, panels (a) and (c), shows optically-thin and right column, panels (b) and (d), optically-thick systems. Other parameters: $\rho_a = 1$, $e_{\rm gas,a} = 0.009137055837563452$, $u^x_a = u^y_a = 0$, $\widehat{F}^x_a = \widehat{F}^y_a = 0$, $B^x_a = B^y_a = B_0$, $\kappa_{\rm abs} = 0$, $k = 2\pi$, $\Gamma = 5/3$, and $\mathbb{P} \equiv p_{\rm rad,a}/p_{\rm gas,a}$, $\kappa_{\rm es} = \tau$ as given in the Table. Here we choose $B_0 = 0$ for sound waves and $B_0 = 0.10075854437197568$ for fast and slow waves. Perturbations are of the form $q^i = Re\,[q^i_a + \delta q^i e^{i(\omega t - kx)}]$.

(a)		Optically-thin, gas-dominated ($\tau = 0.1$, $\mathbb{P} = 0.1$)
sound wave	$\delta\rho_0$	1e-06 + 0 *i*
	$\delta e_{\rm gas}$	1.51556529080798e-08 + 7.69692971953054e-10 *i*
	δu^x	9.97992249118626e-08 + 2.55207217592872e-09 *i*
	δu^y	0 + 0 *i*
	δB^y	0 + 0 *i*
	$\delta\widehat{E}$	1.33147769911346e-13 + 3.6001746512389e-11 *i*
	$\delta\widehat{F}^x$	-2.52471264862269e-10 + 7.40040781015203e-11 *i*
	$\delta\widehat{F}^y$	0 + 0 *i*
	ω	0.627057023634126 + 0.0160351423986572 *i*
fast wave	$\delta\rho_0$	1e-06 + 0 *i*
	$\delta e_{\rm gas}$	1.5198360895975e-08 + 4.81575290993662e-10 *i*
	δu^x	1.60251314293283e-07 + 7.2383120050772e-10 *i*
	δu^y	-9.79544263084857e-08 + 9.83678950177998e-10 *i*
	δB^y	1.62343664101617e-07 − 8.96662164240542e-10 *i*
	$\delta\widehat{E}$	1.48421181882934e-12 + 6.06322316295508e-11 *i*
	$\delta\widehat{F}^x$	-3.95432710842345e-10 + 8.51051304663626e-11 *i*
	$\delta\widehat{F}^y$	2.36679521545993e-10 + 2.11182386936598e-11 *i*
	ω	1.00688870342377 + 0.00454796556390826 *i*
slow wave	$\delta\rho_0$	1e-06 + 0 *i*
	$\delta e_{\rm gas}$	1.50174235106495e-08 + 1.22298943455801e-09 *i*
	δu^x	6.15332754996702e-08 + 1.83139801648519e-09 *i*
	δu^y	9.89772118301622e-08 + 6.54185791061938e-09 *i*
	δB^y	-6.14882091832378e-08 − 5.88315338295397e-09 *i*
	$\delta\widehat{E}$	1.9170283012363e-13 + 2.18721458210053e-11 *i*
	$\delta\widehat{F}^x$	-1.65180532693438e-10 + 7.1752041819694e-11 *i*
	$\delta\widehat{F}^y$	-2.23678888272661e-10 − 7.43141463935117e-11 *i*
	ω	0.386624972522161 + 0.0115070131087776 *i*

(b)		Optically-thick, gas-dominated ($\tau = 10$, $\mathbb{P} = 0.1$)
sound wave	$\delta\rho_0$	1e-06 + 0 *i*
	$\delta e_{\rm gas}$	1.1797669003418e-08 + 3.04292104805925e-09 *i*
	δu^x	9.29098565575498e-08 + 1.44382411133922e-08 *i*
	δu^y	0 + 0 *i*
	δB^y	0 + 0 *i*
	$\delta\widehat{E}$	1.98197717210158e-09 + 2.2064547519989e-09 *i*
	$\delta\widehat{F}^x$	-4.36777061885618e-10 + 4.31621443724302e-10 *i*
	$\delta\widehat{F}^y$	0 + 0 *i*
	ω	0.58376984561456 + 0.0907181444251821 *i*
fast wave	$\delta\rho_0$	1e-06 + 0 *i*
	$\delta e_{\rm gas}$	1.31055121995324e-08 + 2.26907894858283e-09 *i*
	δu^x	1.59214919060003e-07 + 4.26730946717188e-09 *i*
	δu^y	-9.86565964237949e-08 + 6.11642411231371e-09 *i*
	δB^y	1.63044500663243e-07 − 5.5401556994765e-09 *i*
	$\delta\widehat{E}$	2.95346370713069e-09 + 1.59680781762658e-09 *i*
	$\delta\widehat{F}^x$	-2.7219589023768e-10 + 6.08653555066593e-10 *i*
	$\delta\widehat{F}^y$	3.23862842131416e-12 + 2.38270732468968e-11 *i*
	ω	1.0003768401216 + 0.0268122961453227 *i*
slow wave	$\delta\rho_0$	1e-06 + 0 *i*
	$\delta e_{\rm gas}$	1.03536412109072e-08 + 2.54899319130145e-09 *i*
	δu^x	5.51070747399867e-08 + 6.81771795916397e-09 *i*
	δu^y	7.68347744278899e-08 + 1.80695857270459e-08 *i*
	δB^y	-4.16352105336264e-08 − 1.54220614899084e-08 *i*
	$\delta\widehat{E}$	9.0589203896316e-10 + 1.85948699094183e-09 *i*
	$\delta\widehat{F}^x$	-3.83040910798238e-10 + 1.9926795423209e-10 *i*
	$\delta\widehat{F}^y$	2.11405825132413e-12 − 6.39415393177625e-12 *i*
	ω	0.346247962327932 + 0.0428369853095135 *i*

(c)		Optically-thin, radiation-dominated ($\tau = 0.1$, $\mathbb{P} = 10$)
sound wave	$\delta\rho_0$	1e-06 + 0 *i*
	$\delta e_{\rm gas}$	9.14134312414906e-09 + 3.83221342644378e-10 *i*
	δu^x	7.74804632510917e-08 + 3.58319335378836e-09 *i*
	δu^y	0 + 0 *i*
	δB^y	0 + 0 *i*
	$\delta\widehat{E}$	-1.52193074553572e-10 + 9.38040606030636e-10 *i*
	$\delta\widehat{F}^x$	-1.93666448665796e-08 − 7.93046885686635e-10 *i*
	$\delta\widehat{F}^y$	0 + 0 *i*
	ω	0.486824108292728 + 0.0225138678333065 *i*
fast wave	$\delta\rho_0$	1e-06 + 0 *i*
	$\delta e_{\rm gas}$	9.20593402786723e-09 + 7.43788681605899e-10 *i*
	δu^x	1.51647542124337e-07 + 2.92430743208669e-09 *i*
	δu^y	-1.11471565905267e-07 + 6.59617536694267e-10 *i*
	δB^y	1.74787152941627e-07 − 1.8658034881622e-09 *i*
	$\delta\widehat{E}$	-4.70212889643857e-10 + 1.98234059740446e-09 *i*
	$\delta\widehat{F}^x$	-3.79422297680303e-08 − 3.18097469382448e-10 *i*
	$\delta\widehat{F}^y$	2.69349129873962e-08 + 2.6704669357673e-09 *i*
	ω	0.952829608545529 + 0.0183739654909631 *i*
slow wave	$\delta\rho_0$	1e-06 + 0 *i*
	$\delta e_{\rm gas}$	9.13449746980553e-09 + 2.48194479126941e-10 *i*
	δu^x	5.01905313372291e-08 + 2.38661835159163e-09 *i*
	δu^y	6.76529059165483e-08 + 3.82639444942364e-09 *i*
	δB^y	-3.51141271790158e-08 − 1.22066297927614e-09 *i*
	$\delta\widehat{E}$	-7.35475223430181e-11 + 6.00744732838449e-10 *i*
	$\delta\widehat{F}^x$	-1.25407400097346e-08 − 5.53621772791961e-10 *i*
	$\delta\widehat{F}^y$	-1.48948162136833e-08 − 5.73105396778065e-09 *i*
	ω	0.315356409057614 + 0.0149955653605657 *i*

(d)		Optically-thick, radiation-dominated ($\tau = 10$, $\mathbb{P} = 10$)
sound wave	$\delta\rho_0$	1e-06 + 0 *i*
	$\delta e_{\rm gas}$	1.17069780348943e-08 + 1.88153271018629e-09 *i*
	δu^x	2.66250797919881e-07 + 6.33514446524509e-08 *i*
	δu^y	0 + 0 *i*
	δB^y	0 + 0 *i*
	$\delta\widehat{E}$	2.05419184448571e-07 + 1.49858618430197e-07 *i*
	$\delta\widehat{F}^x$	-2.07308153187279e-08 + 3.77555645793647e-08 *i*
	$\delta\widehat{F}^y$	0 + 0 *i*
	ω	1.67290310151504 + 0.39804886622888 *i*
fast wave	$\delta\rho_0$	1e-06 + 0 *i*
	$\delta e_{\rm gas}$	1.17305399804545e-08 + 1.71290104013922e-09 *i*
	δu^x	2.78499110985032e-07 + 5.23803931682287e-08 *i*
	δu^y	-2.81093153546097e-08 + 6.25587500197671e-09 *i*
	δB^y	1.10169648551894e-07 − 4.0333708502353e-09 *i*
	$\delta\widehat{E}$	2.07294118408597e-07 + 1.36363627261037e-07 *i*
	$\delta\widehat{F}^x$	-1.83330848150565e-08 + 3.63663817465466e-08 *i*
	$\delta\widehat{F}^y$	2.67581446787218e-10 + 1.242717958826e-09 *i*
	ω	1.74986152220373 + 0.329115716738904 *i*
slow wave	$\delta\rho_0$	1e-06 + 0 *i*
	$\delta e_{\rm gas}$	9.46188670634028e-09 + 1.21375747602521e-09 *i*
	δu^x	8.34268734887456e-08 + 1.20828776295457e-08 *i*
	δu^y	1.1363325579508e-07 + 2.72697239558014e-07 *i*
	δB^y	-8.03822945939874e-08 − 3.03114251603687e-07 *i*
	$\delta\widehat{E}$	2.59666249422664e-08 + 9.67891091325844e-08 *i*
	$\delta\widehat{F}^x$	-1.98262867256072e-08 + 5.47609651018276e-09 *i*
	$\delta\widehat{F}^y$	3.6607454416002e-09 − 1.14749752402299e-09 *i*
	ω	0.524186505728416 + 0.0759189591904107 *i*

Table 2. Radiative shock tubes

Test				Left state:				Right state:			
No.	Γ	$\sigma_{\rm rad}$	$\kappa_{\rm abs}/\rho_0$	ρ_0	$p_{\rm gas}$	u^x	$\widehat{E}$	ρ_0	$p_{\rm gas}$	u^x	$\widehat{E}$
1	5/3	$3.085 \cdot 10^9$	0.4	1.0	3.0×10^{-5}	0.015	1.0×10^{-8}	2.4	1.61×10^{-4}	6.25×10^{-3}	2.51×10^{-7}
2	5/3	$1.953 \cdot 10^4$	0.2	1.0	4.0×10^{-3}	0.25	2.0×10^{-5}	3.11	4.512×10^{-2}	8.04×10^{-2}	3.46×10^{-3}
3a	2	$3.858 \cdot 10^{-8}$	0.3	1.0	6.0×10^1	10.0	2.0	8.0	2.34×10^3	1.25	1.14×10^3
3b	2	$3.858 \cdot 10^{-8}$	25.0	1.0	6.0×10^1	10.0	2.0	8.0	2.34×10^3	1.25	1.14×10^3
4a	5/3	$3.470 \cdot 10^7$	0.08	1.0	6.0×10^{-3}	0.69	0.18	3.65	3.59×10^{-2}	0.189	1.3
4b	5/3	$3.470 \cdot 10^7$	0.7	1.0	6.0×10^{-3}	0.69	0.18	3.65	3.59×10^{-2}	0.189	1.3
5	2	$3.858 \cdot 10^{-8}$	1000.0	1.0	6.0×10^1	1.25	2.0	1.0	6.0×10^1	1.10	2.0

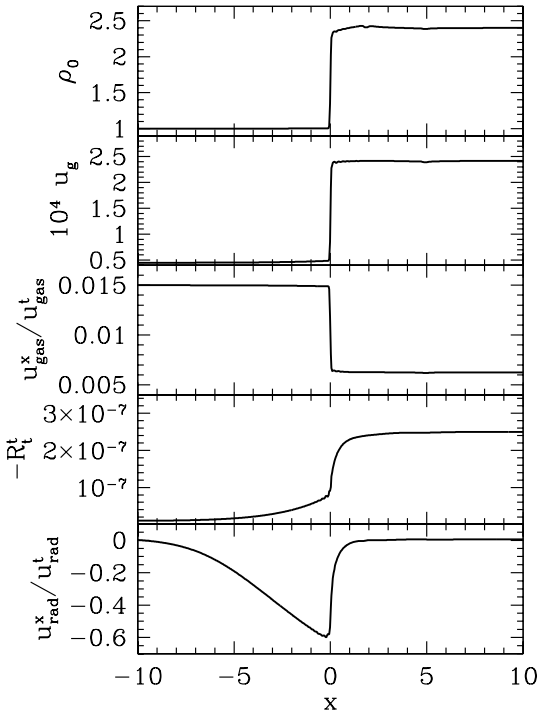

Figure 2. Results obtained for radiative shock tube test No. 1. From top to bottom, the panels show the profiles rest-mass density (ρ_0), gas internal energy density ($e_{\rm gas}$), gas 3-velocity ($u^x_{\rm gas}/u^t_{\rm gas}$), lab-frame radiative energy density ($-R^t_t$), and radiation 3-velocity ($u^x_{\rm rad}/u^t_{\rm rad}$). The profiles match the analytical solution, except for a slight bump in density near the shock.

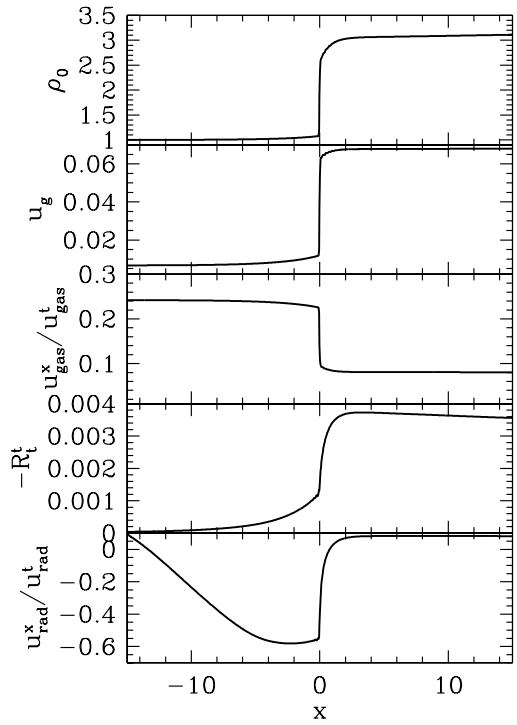

Figure 3. Same as Fig. 2 but for radiative shock tube test No. 2. The profiles match the analytical solution.

ment between the numerical and semi-analytical (Farris et al. 2008) profiles is good.

Fig. 4 shows results corresponding to radiative shock tube tests No. 3a and 3b. These are strongly relativistic shocks with upstream $u^x = 10$. Test No. 3a corresponds to shock tube test 3 of Farris et al. (2008), while test 3b is the optically thick version of the same test which was proposed and solved by Roedig et al. (2012). These two tests verify that the code is able to resolve a highly relativistic wave in two very different optical depth limits. In both cases, the numerical solution reaches a steady state and closely follows the corresponding semi-analytical solution as presented in (Farris et al. 2008; Sądowski et al. 2013c). The acceptable and normal amount of mild oscillations near the shock appear because we use the high-order PPM reconstruction and the flattener is only moderately efficient at reducing the order of spatial interpolation near shocks.

Fig. 5 shows results for radiative shock tube tests No. 4a and 4b. These tests correspond to radiation pressure dominated mildly relativistic waves. Test 4b is the optically thick version of test 4a that was proposed by Roedig et al. (2012). In both tests, the numerical solution reaches a stationary state and agrees well with the semi-analytical solution. The opacity coefficient $\kappa_{\rm abs}$ in tests 3b and 4b are the maximum values that the scheme by Roedig et al. (2012) could handle while remaining stable. The algorithm implemented in `harmrad` has no such limitation.

Fig. 6 corresponds to radiative shock tube test No. 5. This is the only test that does not asymptote to a stationary solution. This test was proposed and solved by Roedig et al. (2012) and represents an optically thick flow with mildly relativistic velocities. The left- and right-states are identical except that they have different velocities. As a result, two shock waves propagate in opposite directions. This test does not have an analytical solution. However, by comparing our numerical solution with that presented in Roedig et al. (2012), we confirm that our scheme performs well.

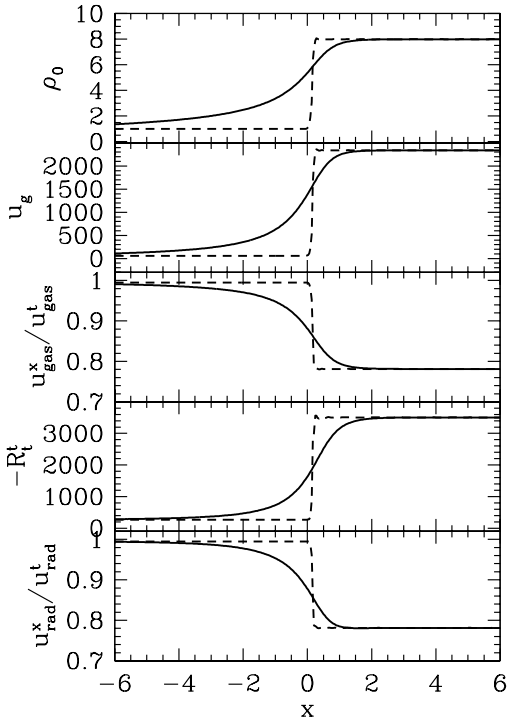

Figure 4. Similar to Fig. 2 but showing results for radiative shock tube tests No. 3a (solid) and No. 3b (dashed). The profiles match the analytical solution.

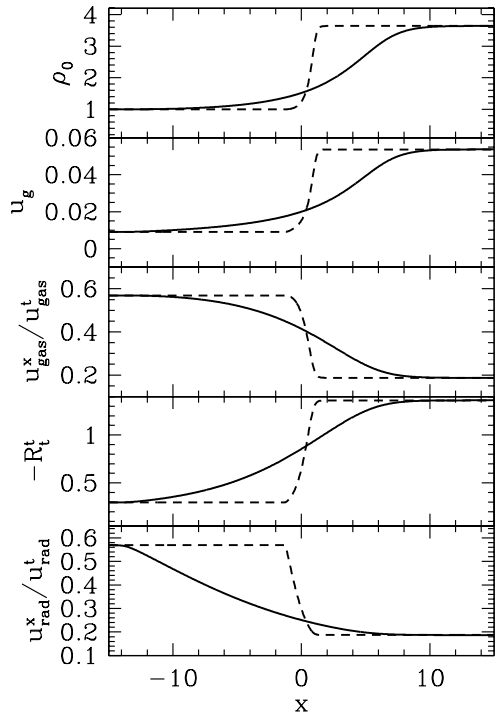

Figure 5. Similar to Fig. 2 but showing results for radiative shock tube tests No. 4a (solid) and No. 4b (dashed). The profiles match the analytical solution.

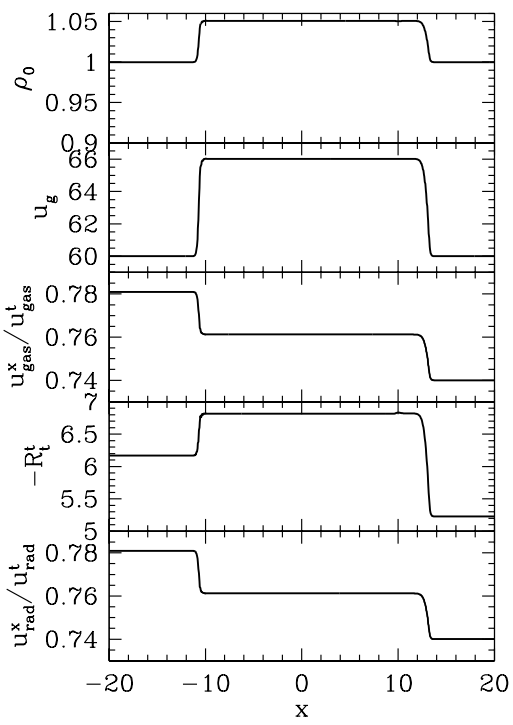

Figure 6. Same as Fig. 2 but for radiative shock tube test No. 5. There is no analytical solution available for this problem, but it agrees with prior work.

5.3 Optically Thin Radiative Pulse in 3D Cartesian Minkowski

We now test the ability of our scheme to handle the evolution of a radiation pulse in the optically thin limit. We set up a Gaussian distribution of radiative energy density at the center of a 3D Cartesian coordinate system. The pulse radiative temperature is set according to,

$$T_{\rm rad} = \left(\frac{E}{4\sigma}\right)^{1/4} = T_a\left(1 + 100e^{-(x^2+y^2+z^2)/w^2}\right), \qquad (82)$$

with $T_a = 10^6$, $w = 5.0$. The value of $a_{\rm rad} \approx 8.77\times10^{-12}$. We assume zero absorption opacity ($\kappa_{\rm abs} = 0$) and scattering opacity ($\kappa_{\rm es} = 0$). The background fluid field has constant density $\rho_0 = 1$ and temperature $T = T_a$. We solve the problem in three dimensions on a coarse Cartesian grid of $32x32x32$ and $50x50x50$ cells (showing only the $50x50x50$ result).

The initial pulse in radiative energy density is expected to spread isotropically with the speed of light (optically thin medium) and to decrease inversely proportionally to the square of radius (energy conservation). Such behavior is visible in Fig. 7 showing the radiative energy distribution in the $z = 0$ plane (left panel) and its cross-section along $y = z = 0$ (right panel). The orange circles in the left panel show the expected size of the pulse. It is clear that the propagation speed of the pulse is consistent. This problem was solved on a relatively coarse Cartesian grid, and this results in deviations from the perfectly spherical shape. Also, the PPM scheme uses a stencil size of ±4 cells, so one should have an initial radiative distribution mostly within $\gg 8$ cells to avoid grid-induced artifacts. The solution becomes more isotropic at larger resolution or when using a spherical grid. The right panel in Fig. 7 shows the profiles of the energy density along the x-axis, which follows the expected rate of energy decrease with increasing distance from the center.

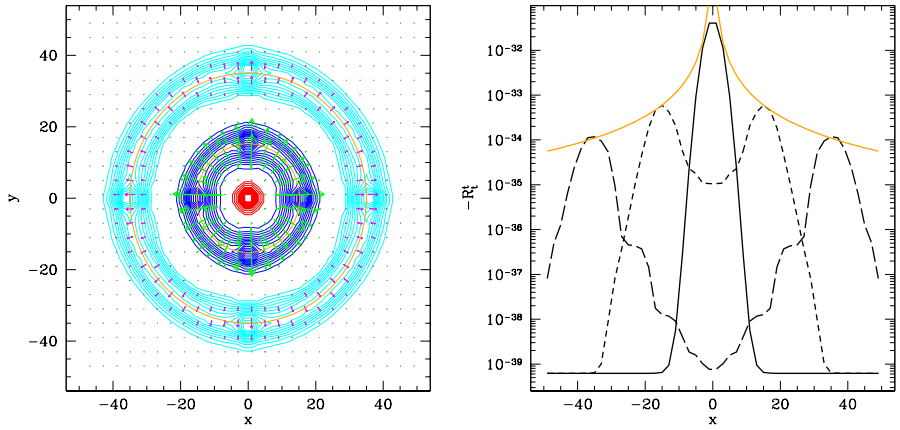

Figure 7. Profiles of the lab-frame radiative energy density ($-R^t_t$) for the optically thin radiative pulse test described in section 5.3. The left panel shows the distribution in the $x-y$ plane at $z=0$ at times $t=0$ (red, 15 contours from 6.24×10^{-40} to 4.038×10^{-32}), $t=15.21$ (blue, 15 contours from 6.24×10^{-40} to 5.963×10^{-34}), and $t=35.01$ (cyan, 15 contours from 6.24×10^{-40} to 1.174×10^{-34}) with lab-frame energy flux ($-R^i_t$) shown for $t=15.21$ (green vectors) and $t=35.01$ (magenta vectors). The orange circles correspond to the initial pulse spreading at the speed of light from $x=y=z=0$, and the centroid of the pulse distribution matches well with this position for both evolved times. The right panel shows the same times at $t=0$ (solid), $t=15.21$ (dashed), and $t=35.01$ (long-dashed) in the $y=z=0$ line. The pulse should decay as $1/x^2$, which is shown as an orange line, and there is a reasonable match.

5.4 Optically Thick Radiative Pulse in 1D Cartesian Minkowski

To test the optically thick limit we choose to set up a similar pulse but this time planar instead of a point-like, i.e., according to,

$$T_{\rm rad}=\left(\frac{E}{4\sigma}\right)^{1/4}=T_a\left(1+100e^{-x^2/w^2}\right). \tag{83}$$

This time we set the scattering opacity to $\kappa_{\rm es}=10^3$ and solve the problem as one-dimensional on 100 grid points distributed uniformly between $x=-50$ and $x=50$ with periodic boundary conditions in y and z. The total optical depths per cell and per pulse are therefore $\tau=10^3$ and $\tau=10^4$, respectively. The value of $a_{\rm rad}\approx8.77\times10^{-12}$ in code units and the absorption opacity is zero.

In the optically thick limit the evolution of such a system is described by a diffusion equation with diffusion coefficient $D=1/(3\kappa_{\rm tot})$. An initially Gaussian pulse of radiative internal energy will diffusive as

$$-R^t_t(t)=A\exp\left(\frac{-x^2}{4D(t+t_0)}\right)\left(\frac{t+t_0}{t_0}\right)^{-n/2}, \tag{84}$$

for $n=1$ dimensions, $t_0\approx4800$ and $A\approx5.49\times10^{-32}$.

In Fig. 8 we plot profiles of the radiative energy at various moments and compare them to the analytical solution given by Eq. 84. The numerical solution for the central two points diffuses slightly faster due to the additional numerical dissipation introduced by the scheme. At later times this difference becomes insignificant.

A code's speed can be sensitive to this high optical depth case, depending upon the way the initial guess is chosen in the implicit solver as well as how the wavespeeds are determined. `harmrad` only takes 200 steps with 2.6 average energy-based iterations using the URAD scheme without stages, and despite the large timesteps, the Newton method does not need to reject any implicit Newton steps as could happen for large steps when conserved quantities step out of bounds without a physical primitive inversion.

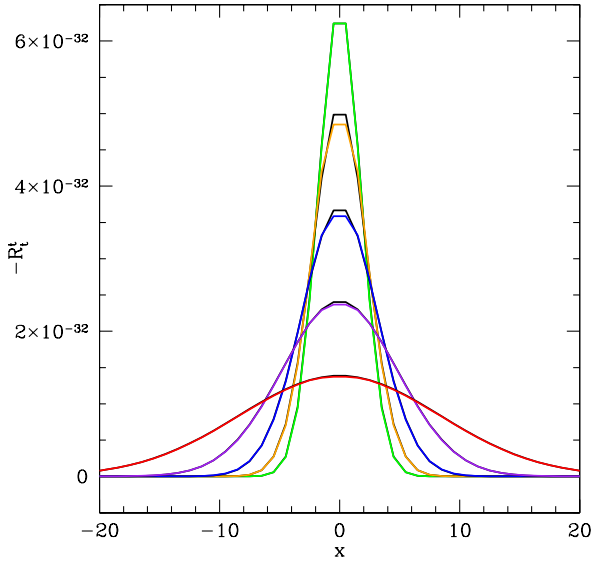

Figure 8. The radiative energy density for the optically thick pulse described in section 5.4. The colored lines show times $t=0$ (green), $t=2951.05$ (orange), $t=9867.95$ (blue), $t=29877.1$ (purple), and $t=10^5$ (red). Behind each solution is a black line for the analytical solution from Eq. 84 (which overlaps at $t=0$). The analytical and numerical solutions agree very well in this diffusion regime at high optical depth.

5.5 Single Beam of Light in 2D Cartesian Minkowski

Fig. 9 show the results for an injected single beam of light with a top-hat distribution. The gas and radiation are decoupled by neglecting absorptions and scatterings ($\kappa_{\rm abs}=\kappa_{\rm tot}=0$). The grid is two-dimensional in the $x-y$ plane with 31 points distributed uniformly from 0 to 1 in each dimension. All initial values for primitive quantities are negligibly small. The ideal gas constant is set to $\gamma=4/3$. Outflow boundary conditions are used on all borders, except the region covered by the beam from $y=0.4$ to $y=0.6$, where we set the injected lab-frame radiation energy density to be 100

times the ambient value, and we set the radiative 3-velocity to be to be $v^x_{\rm rad} = 0.99998$ or $\gamma_{\rm rad} \approx 500$. The value of $a_{\rm rad} \approx 1.18\times10^{17}$, and the maximum radiative gamma allowed is $\gamma_{\rm rad} = 1000$. Note that for $\gamma_{\rm rad} \gtrsim 2000$, the beam edge can appear mildly unstable with PPM, but there is no significant disruption and the beam moves at the correct speed. Higher $\gamma_{\rm rad}$ are achievable with MINM limiter at the cost of resolution/accuracy in more general simulations.

5.6 Single Shadow in 2D Cartesian Minkowski

Here we test the ability of the M1 closure scheme, as incorporated in `harmrad`, to resolve shadows. We set up a blob of dense, optically thick gas in flat space-time, surrounded by an optically thin medium, and we illuminate this system.

We start with a single source of light imposed on the left boundary. We solve the problem in two dimensions on a 100×50 grid, with the density blob distribution set to be

$$\rho_0 = \rho_a + (\rho_b - \rho_a)\, e^{-\sqrt{x^2+y^2}/w^2}, \tag{85}$$

where $\rho_a = 10^{-4}$, $\rho_b = 10^3$ and $w = 0.22$. The gas temperature is adjusted so as to give constant pressure throughout the domain,

$$T = T_a \frac{\rho_a}{\rho_0}, \tag{86}$$

with $\gamma = 1.4$.

The initial radiative energy density is set to the local thermal equilibrium value, and the initial velocities and radiative fluxes are zero. We apply periodic boundary conditions at the top and bottom and outflow boundary conditions at the right border of the domain. At the left border we have the external source of light, which we specify with $E_L = 4\sigma T_L^4$, $F^x = 0.99999E_L$, $T_L = 100T_a$. All other quantities are set to match the ambient gas. We assume $\kappa_{\rm abs} = \kappa_{\rm tot} = \rho_0$. The value of $a_{\rm rad} \approx 351.37$ in code units, and the maximum radiative gamma allowed is $\gamma_{\rm rad} = 447.215$.

Fig. 10 shows the results at $t = 10$. By this time, the initial radiation wave has passed through the domain and the system has reached a stationary state. The M1 closure is designed to keep flux moving parallel to itself in optically thin regions for $F \approx E$. As a result, a strong shadow develops behind the optically thick blob.

Note that the beam is stable up to a choice of $\gamma_{\rm rad} \gtrsim 2000$ for the beam injected. However, the radiation behind the blob has a few lack of implicit inversion solutions beyond $\gamma_{\rm rad} \sim 500$, although this only affects the radiative velocity where the radiative energy density is negligible.

5.7 Double Shadow in 2D Cartesian Minkowski

We also consider a two-beam test problem similar to the one described in Jiang et al. (2012). We set up similar initial conditions for gas and radiation as in the single beam shadow test. This time, however, we set up a reflection symmetry at the lower boundary ($y = 0$) and we impose an inclined (lab-frame $F^x_0 = 0.93E_0$, $F^y_0 = -0.37E_0$ with $\gamma_{\rm rad}$ limited as stated) beam on the upper boundary and on the part ($y > 0.3$) of the left boundary. As a result, the domain is effectively lit by two self-crossing beams of light.

We plot the result of a numerical simulation in Fig. 11. In the region near the left top, where the beams do not overlap, the direction of the flux follows the imposed boundary condition. In the region of the overlap the radiative energy density increases twice ($E = 2E_0$) while the flux becomes equivalent to the superposition of the beam-intrinsic fluxes, i.e., it is purely horizontal and its x-component equals $F^x = 2F^x_0 = 1.86E_0 = 0.93E$. The clump of optically thick gas is, therefore, effectively illuminated by a purely horizontal beam. Unlike in the planar beam case, there are regions of the partial shadow (penumbra) resulting from these perpendicular photons allowed by the closure when $F^x < E$. The region of the total shadow (umbra) is therefore limited by the edges of the penumbra and follows the expected shape (compare Fig. 11 in Jiang et al. (2012)) to a good accuracy. The M1 closure, however, produces an extra narrow horizontal shadow along the x-axis that should not be present.

For Fig. 11 we set the beam's $\gamma_{\rm rad} \approx 22$, because with PPM any higher values lead to mild oscillations driven away from the stationary inclined radiative edge into the rest of the beam. Even at $\gamma_{\rm rad} \approx 500$ these oscillations are only at the $\leqslant 20\%$ level and are proportional to the beam's $(\gamma_{\rm rad})^{1/2}$, but it is visually obvious in such plots. We plan to continue to improve PPM and HLL/LAXF (designed for fluid shocks, not radiative jumps) to work better at radiative discontinuities that are stationary and not aligned with the grid. No such oscillations appear with MINM that is significantly more diffusive for general applications. Much weaker oscillations $< 2\%$ for $\gamma_{\rm rad} \approx 2000$) appear when using HLL, but for general applications (e.g. highly magnetized or nearly force-free flows near a rotating black hole), we have found HLL to also be unstable (apparently due to the conflict between the causal one-sided flux solution and the acausal centered reconstruction stencil).

This test shows limits of the M1 closure approach but at the same time stresses the fact that, in principle, it does not limit specific intensity to one particular direction (assuming only its symmetry with respect to the flux). It performs much better than the Eddington approximation, but in the case of multiple sources of light it must be used with caution.

5.8 Static Radiative Atmosphere in 1D Spherical Polar Minkowski

An important aspect of radiation in accretion disks is momentum transfer between radiation and gas, such as the balance expressed by the Eddington luminosity described in section 1. To validate the treatment of gas-radiation momentum exchange, we consider a static atmosphere which is in equilibrium under the action of gravity, a gas pressure gradient, and the radiation force. We take the optically thin limit and assume that gas-radiation interactions occur only through a scattering coefficient, i.e., $\kappa_{\rm abs} = 0$, $\kappa_{\rm tot} = \kappa_{\rm es}$. We consider a polytropic atmosphere with equation of state $p_{\rm gas} = K{\rho_0}^\Gamma$.

An analytical solution can be obtained for this model problem. For a polytropic equation of state and $\kappa_{\rm abs} = 0$, there is no energy equation, and the radial component of the momentum equation can be used to find the solution. In the non-relativistic limit ($r \gg 2$), assuming stationarity ($\partial_t = 0$) and zero velocity ($v^i = 0$), the radial momentum equation takes the form

$$\frac{1}{\rho_0}\frac{\partial p}{\partial r} = -\frac{1-f}{r^2}, \tag{87}$$

where

$$f = \kappa_{\rm es} F_{\rm in} r^2_{\rm in}. \tag{88}$$

Here $F_{\rm in}$ is the radiative flux imposed as a boundary condition at the bottom of the atmosphere, $r = r_{\rm in}$, and f gives the ratio of the radiative to gravitational (or geometrical) forces; $f = 1$ corresponds to the Eddington limit, where the luminosity is $L_{\rm Edd} = 4\pi/\kappa_{\rm es}$ and the radiative flux is $F_{\rm in} = F_{\rm Edd} = 1/\kappa_{\rm es} r^2_{\rm in}$. Since radiative energy

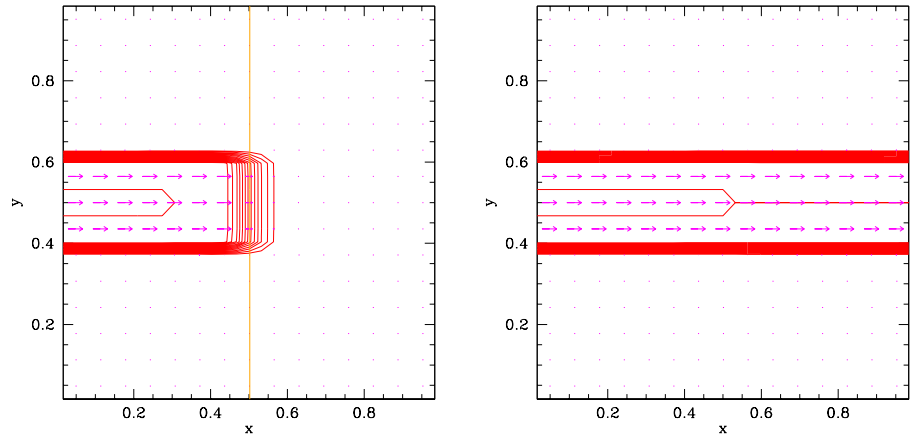

Figure 9. Results for single beam of light in Minkowski for beam injected with $\gamma_{\rm rad} \approx 500$ in section 5.5. Left panel shows $t = 0.5023$ with 15 red contours for $-R^t_t$ from 0.3666 to 3.333×10^7 and R^i_t as magenta vectors scaled by 5×10^{-8} shown every other grid point. Orange vertical line indicating the light travel distance since injection. Right panel shows $t = 10$ with 15 red contours for $-R^t_t$ from 0.494 to 3.333×10^7 and R^i_t as magenta vectors scaled by 5×10^{-8} shown every other grid point. The beam travels out as expected.

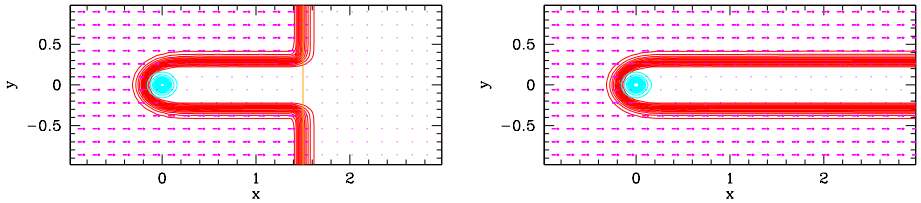

Figure 10. Results for shadow in Minkowski for beam injected with $\gamma_{\rm rad} \approx 158$ in section 5.6. Left panel shows $t = 2.502$ with 15 red contours for $-R^t_t$ from 9×10^{-25} to 2.5×10^{-14} and R^i_t as magenta vectors scaled by 2×10^{12} shown every 4th grid point. Orange vertical line indicating the light travel distance since injection. Right panel shows $t = 10$ with 15 red contours for $-R^t_t$ from 2.085×10^{-26} to 2.5×10^{-14} and R^i_t as magenta vectors scaled by 2×10^{12} shown every 4th grid point. In both panels the massive blob is shown as ρ_0 with 15 cyan contours from 0.0001 to 557.4. The beam travels out as expected with no beam instability or disruption. As required, the shadow is sharply defined with negligible radiative flux behind the blob of mass.

must be conserved, in the stationary state the flux must satisfy $F = F_{\rm in} r_{\rm in}^2/r^2$ (non-relativistic limit).

The solution to Eq. (87) is

$$\rho_0 = \rho_a \equiv \left[\frac{(\Gamma-1)}{\Gamma K}\left(C + \frac{1-f}{r}\right)\right]^{\frac{1}{\Gamma-1}}, \tag{89}$$

where

$$C = \frac{\Gamma K}{(\Gamma-1)}\rho_{0,\rm in}^{\Gamma-1} - \frac{1-f}{r_{\rm in}}, \tag{90}$$

and $\rho_{0,\rm in}$ is the assumed rest-mass density at $r = r_{\rm in}$. The entropy constant K is calculated at the bottom of the atmosphere from the assumed gas temperature $T_{\rm in}$.

We set up a uniform spherical polar grid in Boyer-Lindquist coordinates with only 40 points between $r = 10^6$ and 1.4×10^6 gravitational radii with θ spanning only 1 cell from $0.99\pi/2$ to $1.01\pi/2$. We scaled all quantities to physical units assuming $M = 1M_\odot$ and $\kappa_{\rm es} = 0.4\rho_0\,{\rm cm}^{-1}$. At the innermost radius we set $\rho_{0,\rm in} = 10^{-15}\,{\rm g\,cm}^{-3}$ (optically thin atmosphere) and $T_{\rm in} = 10^6\,{\rm K}$. All the velocities were initially zero and the radiative energy density $E = F_{\rm in}/0.99999$. Initial values of the gas density and temperature in the domain and in the ghost cells were assigned based on the analytical solution. We ran four models corresponding to four luminosities: 10^{-10}, 0.1, 0.5 and $1.0\,L_{\rm Edd}$. Each model was run up to a time $t = 2 \times 10^9 M$, which is sufficient to reach relaxed steady state for these optically thin atmospheres.

Fig. 12 shows the results. For the top panel, the higher the luminosity, the flatter is the density profile, indicating the effect of the outward force due to radiation. For the particular case of the Eddington luminosity, the density should be perfectly constant, reflecting the fact that the gravitational force is exactly balanced by radiation and no pressure gradient in required. Even at this low resolution, `harmrad` properly handles gas-radiation momentum exchange as shown by looking at the residuals in the 2nd panel, where fractional deviations in the density are below $\lesssim 2\%$. Much of the error is because of the finite $\gamma_{\rm rad} \approx 158$ rather than $v = c$ (i.e. a smaller $F_{\rm in}/E \sim 0.99$ gives about 3 times larger errors), the PPM reconstruction, what form of the primitives one interpolates (e.g. interpolating more constant quantities leads to much lower error for the $F_{\rm in} = 1.0F_{\rm Edd}$ case), and small relativistic corrections for the non-relativistic solution.

The middle panel in Fig. 12 shows our results for the radial radiative flux. Once again, the models behave very well and the agreement with the analytical solution is excellent. Finally, the bottom panel shows the residual radial velocities (v_r/c). These are of the order of 10^{-5} (they should be zero), and appear to be mostly driven by slight inconsistencies near the boundaries for reasons similar to the reasons given for the density deviations. Use of MINM or HLL vs. LAXF or the entropy equations does not improve these errors, but the errors do decrease with increasing resolution, but only to

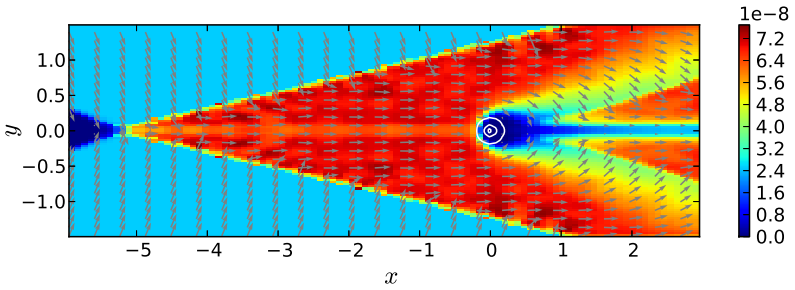

Figure 11. Results for double shadow test in Minkowski for beam injected with $\gamma_{\rm rad} \approx 22$ at an angle, which then reflects and interacts with the original beam before casting a shadow due to the blob in section 5.7. Shows lab-frame $-R^t_t$ at $t = 20$ as color (with legend), and lab-frame $-R^i_t$ as vectors. White contours show three logarithmic rest-mass contours from $\rho_0 = 100$ to $\rho_0 = 650$. The radiative intersection is sharply defined, but PPM with HLL (as shown) generates slight oscillations that drives weak waves into the beam.

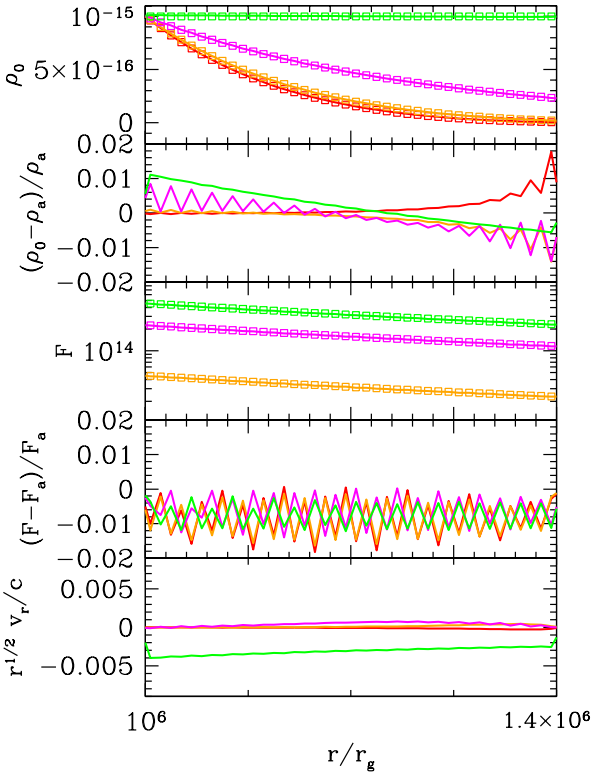

Figure 12. Results obtained with the static atmosphere test in section 5.8. Numerically determined profiles and residuals between the numerical and analytical solutions are plotted for the density (top panel), radial lab-frame flux (middle panel), and radial velocity (bottom panel, residuals only). Colors denote the Eddington ratio of the flux boundary condition $F_{\rm in}$ at the bottom of the atmosphere: $F_{\rm in} = 10^{-10} F_{\rm Edd}$ (red), $0.1F_{\rm Edd}$ (orange), $0.5F_{\rm Edd}$ (magenta) and $1.0F_{\rm Edd}$ (green). Squares correspond to the numerical solutions and lines show the analytical profiles (equation 87). There is agreement at the percent level between the numerical and analytical solutions.

first order due the errors being introduced by the discontinuities at the inner and outer boundaries.

5.9 Beam of light in 2D spherical polar for $a/M = 0$ Black Hole

To test the performance of the code for radiation in strong gravitational field, we study propagation of a beam of light in the Schwarzschild metric. The technical aspects of these results are qualitatively similar for our (not shown) tests of beams in spherical polar Minkowski, so we only consider the curved space-time case.

Table 3. Model parameters for the light beam tests

Model	$r_{\rm beam}$	$r_{\rm in}$	$r_{\rm out}$
1	3.0 ± 0.1	2.6	3.5
2	6.0 ± 0.2	5.5	7.5
3	16.0 ± 0.5	14.5	20.5

We consider three models, in each of which a beam of light is emitted in the azimuthal direction at a different radius. We decouple gas and radiation by neglecting absorptions and scatterings ($\kappa_{\rm abs} = \kappa_{\rm tot} = 0$). We run the models on a two-dimensional grid with only 30 points distributed uniformly in r between $r_{\rm in}$ and $r_{\rm out}$ (see Table 3 for values) and only 60 points distributed uniformly in azimuthal angle ϕ between $\phi = 0$ and $\pi/2$. Initially, we assign negligibly small values for all primitive quantities, including the radiation energy density and flux. We use outflow boundary conditions on all borders except the region covered by the beam at the equatorial plane (see the range of $r_{\rm beam}$ in Table 3), where we set the radiation temperature to $T_{\rm beam} = 10^{10} = 1000T_a$ and the lab-frame flux to $F^\phi = 0.9999E$. Here T_a is the initial gas and radiation temperature of the ambient medium. We always stop the simulation when the beam reaches the outer boundary and show that result. This corresponds to $t = 9$, $t = 8.5$, $t = 16.5$ for Model 1,2,3, respectively.

The panels in Fig. 13 show the results for the three beam models. Consider the right panel, which corresponds to Model 3 (Table 3) with the beam centered at $r_{\rm beam} = 16$. At such a large radius we do not expect significant bending of photon geodesics and this is indeed the case — the beam is only slightly bent towards the BH. We also expect the beam to be tightly confined, i.e., it should propagate with a nearly constant width. However, the numerical solution shows some artificial broadening (but much less than MINM used in Koral ; Sądowski et al. 2013c).

The middle panel in Fig. 13 shows Model 2, where the beam is centered at the marginally stable orbit: $r_{\rm beam} = 6$. At this radius, photon geodesics are significantly deviated by gravity, resulting in strong curvature in the beam. The numerical beam follows the correct trajectory.

Finally, the left panel in Fig. 13 shows Model 1, where the center of the beam is exactly at the photon orbit: $r_{\rm beam} = 3$. An azimuthally oriented ray at this radius is expected to orbit around the BH at a constant r. This is seen clearly in the numerical solution.

Some of the diffusion seen is due to the need to use $F^\phi = 0.9999E$ with PPM, while some is physical broadening due to photons emitted inside the $r = 3$ curve bending inwards while those emitted outside $r = 3$ bend outward and head towards radial infinity.

A value of $F^\phi = 0.99999E$ (giving $\gamma_{\rm rad} \approx 220$) leads to some disruptions of the beam when using PPM and LAXF. Using HLL or decreasing F^ϕ improves stability. No such disruptions occur with MINM even at $F^\phi = 0.99999E$. Even with PPM and $F^\phi = 0.9999E$ (giving $\gamma_{\rm rad} \approx 70$), some disruptions can eventually occur where the incoming beam interacts with reflections (due to the simplified outflow boundary conditions) off the outer boundary where the beam contacts. As our goal is to test the on-grid behavior (not advanced boundary conditions), we always stop the simulation when the beam reaches the outer boundary. We plan to improve PPM's behavior to add a bit of diffusion to keep such beam's more uniform, but the behavior non-uniformity shown is due to the beam being roughly the size of the PPM stencil size and PPM can exaggerate features on such unresolved scales. Note that use of HLL does not improve the solution compared to the solution shown in Fig. 13.

5.10 Radiative spherical (Bondi) accretion in 1D spherical polar for $a/M = 0$ Black Hole

Our next test problem considers radiative spherical accretion onto a non-rotating BH. This problem has been studied in the past by Shapiro & Teukolsky (1983); Vitello (1984) and Nobili et al. (1991) and more recently by Roedig et al. (2012) and Fragile et al. (2012). We follow Fragile et al. (2012) in the setup of our simulations to facilitate comparison with their results. As in their work, we consider Thomson scattering and thermal bremsstrahlung, which give the following opacity coefficients,

$$\kappa_{\rm abs} = 1.7 \times 10^{-25} T^{-7/2} m_p^{-2} \rho_0 \, {\rm cm}^{-1}, \quad (91)$$

$$\kappa_{\rm tot} = \kappa_{\rm abs} + 0.4\rho_0 \, {\rm cm}^{-1}, \quad (92)$$

where ρ_0 is in g cm^{-3} and m_p is the mass of the proton. Our numerical grid spans from $r_{\rm in}$ to $r_{\rm out} = 2 \times 10^4$ and is resolved by 512 grid points spaced logarithmically following $r = R_0 + \exp(x^{(1)})$. We assume a BH mass of $3M_\odot$. For the initial state, we choose the mass accretion rate $\dot{M}_0$ (see Table 4 for values) and set the density profile accordingly,

$$\rho_0 = -\frac{\dot{M}_0}{4\pi r^2 u^r}, \quad (93)$$

where the radial velocity u^r is equal to its free fall value $u^r = -\sqrt{2/r}$. The gas temperature is given by

$$T = T_{\rm out} \left(\frac{\rho_0}{\rho_{0,\rm out}} \right)^{\Gamma - 1}, \quad (94)$$

where $T_{\rm out}$ is the temperature at the outer radius and Γ is the adiabatic index. The latter is calculated from the radiation to gas pressure ratio $f_p = p_{\rm rad}/p_{\rm gas}$ of the initial state (Table 4),

$$\Gamma = 1 + \frac{1}{3} \left(\frac{2 + 2f_{\rm p}}{1 + 2f_{\rm p}} \right). \quad (95)$$

The radiative energy density is set to $E = 3 f_{\rm p} p_{\rm gas}$.

The numerical simulations are run in one (radial) dimension. The primitive quantities at the outer boundary are fixed at their initial values, as described above. At the inner boundary we apply outflow boundary conditions. We could apply special extrapolating and interpolating radial dependencies, but we avoid changing the boundary conditions to keep the results applicable to more general simulations. Table 4 lists the parameter values we used corresponding to five models. The first model, E1T6, is characterized by the lowest mass accretion rate and is designed to highlight the ability of our scheme to handle optically thin media. The other four models are identical to simulations described in Fragile et al. (2012).

Table 4. Model parameters and results for radiative spherical accretion tests

Model	$\dot{M}_0 c^2 / L_{\rm Edd}$	$T_{\rm out}[K]$	$f_{\rm p} = \frac{p_{\rm rad}}{p_{gas}}$	Measured $L/L_{\rm Edd}$
E1T6	1.0	10^6	1.2×10^{-4}	2.8×10^{-8}
E10T5	10.0	10^5	1.2×10^{-7}	1.3×10^{-6}
E10T6	10.0	10^6	1.2×10^{-4}	3.4×10^{-6}
E10T7	10.0	10^7	1.2×10^{-1}	7.5×10^{-6}
E100T6	100.0	10^6	1.2×10^{-4}	1.0×10^{-4}

Model names and parameters after Fragile et al. (2012).

For all models, we choose a grid such that $r = R_0 + \exp(x_1)$ for some uniform grid x_1. We can set, e.g., $r_{\rm in} = 1.9$ for Kerr-Schild coordinates, while $r_{\rm in} = 2.5$ also works for Boyer-Lindquist coordinates. We show results for Kerr-Schild coordinates using Kerr-Schild coordinates with $r_{\rm in} = 2.5$ and $R_0 = 2.2$ for all models except E10T5 where we choose $r_{\rm in} = 1.9$ and $R_0 = 1.85$ in order to place more cells near the BH to ensure the energy equation evolve remains accurate for $e_{\rm gas}$ despite the small $T_{\rm gas}$. The models are run till $t = 3.13 \times 10^4$, $t = 1.674 \times 10^4$, $t = 1.21 \times 10^5$, $t = 1.485 \times 10^5$, and $t = 1.351 \times 10^5$ for the models E1T6, E10T5, E10T6, E10T7, and E100T6, respectively.

Fig. 14 shows the numerical solutions obtained with `harmrad`. The top panel presents profiles of density, which follow the initial profile (equation 93) throughout the simulation.

The 2nd panel of Fig. 14 shows the gas temperature. For all but the coldest model, E10T5, the temperature follows equation (94). In the case of model E10T5, the gas is hotter than the analytical result. This is because of gas-radiation coupling which heats up the gas as it approaches the BH (the analytical solution assumes that there is no interaction). Some models show mild oscillations in the temperature (or $e_{\rm gas}$), which is due to the large dynamic range in radius when using PPM and the energy equation due to the differences between point and average quantities due to the non-linearity of the energy equation. The noise in $e_{\rm gas}$ is especially pronounced in model E10T5. A higher-order scheme like WHAM (Tchekhovskoy et al. 2007) or a scheme that interpolates conserved quantities (e.g. MP5 in Koral) can improve the temperature behavior. Also, use of the entropy equations in `harmrad` avoids all such oscillations, and the entropy equations need much lower resolution to achieve the same accuracy as the energy equation. Also, the noise in temperature (or $e_{\rm gas}$) with the energy equation is less as one increases resolution or focuses resolution toward the BH by using R_0 closer to $R_{\rm in}$. Note that lowering the implicit solver tolerance (say always requiring $e_T < 10^{-13}$) for the energy method does not avoid the noise.

The 3rd and 4th panels in Fig. 14 show radial profiles of the fluid-frame radiative energy density and fluid frame radial energy flux for the five models. Both quantities follow roughly an r^{-2} scaling, reflecting the fact that in steady-state (barring redshift factors) the luminosity is equal to $4\pi F r^2$ and should be conserved. The glitches at large radius are due to the finite run time of those particular models, as the radiative variables are still evolving towards equilibrium.

Because the flux in these models is non-negligible compared

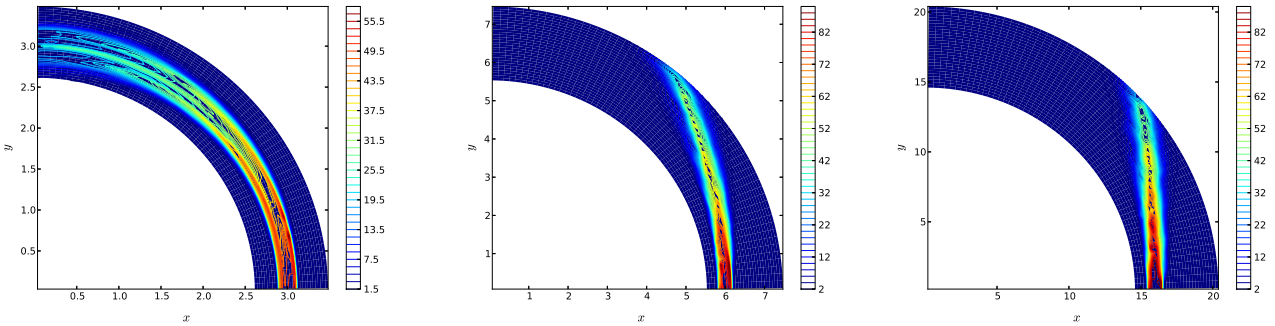

Figure 13. Results for Model 1 (left panel), Model 2 (middle), Model 3 (right), involving light beams propagating near a Schwarzschild BH (see Table 3 for model details) described in section 5.9. The BH is at $r = 0$ (i.e., $x = y = 0$) with horizon $r = 2$. The beams are introduced via a boundary condition on the x-axis. The beams initially move vertically, i.e., in the azimuthal direction, in the lab-frame. Contours indicates the lab-frame radiation energy density. The beams travel as expected in curved space-time.

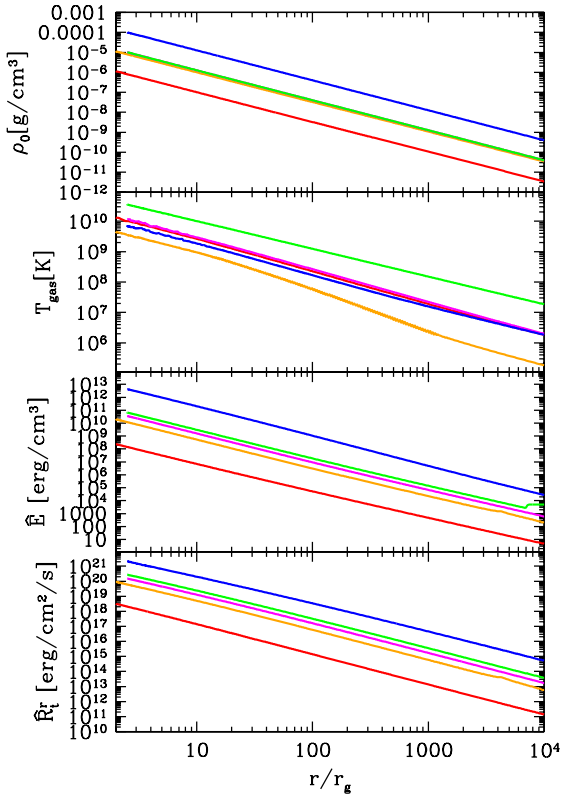

Figure 14. Numerical results obtained with `harmrad` for five models of spherical Bondi accretion with radiation. Parameters of the models are given in Table 4. The panels show density (top), gas temperature (2nd), fluid-frame radiative energy density (3rd), and fluid-frame radiative radial flux (bottom). Lines correspond to models E1T6 (red), E10T5 (orange), E10T6 (magenta), E10T7 (green), and E100T6 (blue). The results show that the code handles well both optically-thin and optically-thick regions for a large radial dynamic range in curved space-time.

to the energy density (e.g., $F \approx 0.9E$ for the E10 family of models), the Eddington closure scheme does not work very well, especially at low optical depth. For instance, Fragile et al. (2012) used Eddington closure and obtained unphysical noise or breaks in their profiles of radiative quantities (see their Figure 5) in all models with $\dot{M}_0 < 300 L_{\rm Edd}$. This just reflects the fact that their closure cannot handle optically thin media. Our algorithm uses the M1 closure scheme and has no problems with either optically thick or thin regimes. To emphasize this point, we have solved an additional model, E1T6, in which the accretion rate is an order of magnitude lower than the smallest rate considered by Fragile et al. (2012). `harmrad` works fine for this model, and can, in fact, handle even more extreme configurations, both at lower and higher accretion rates.

For direct comparison of our results with those reported in Fragile et al. (2012), we have calculated for all our models the luminosities,

$$L = 4\pi F r^2, \tag{96}$$

emerging at radius $r = 7700$ (which is within 10% of the value at $r \sim 1360$.

Fig. 15 shows model E10T7 for different radial resolutions (64, 128, 256, 512) to show convergence behavior. The energy equations fail for 32 cells for such a large radial dynamic range, where clearly visible oscillations appear with 64 cells. The error is dominated by the temperature, which converges to 2nd order. E.g., for the first radial cell, the relative differences in gas temperature between models are 0.2466, 1.194, and 5.125 for 256, 128, and 64, respectively, which is a drop by a factor of 4 for each increase in resolution by a factor of 2. Use of the entropy equation instead of the energy equation reduces the temperature error substantially, with the same convergence rate at that lower error.

5.11 MHD Radiative Bondi Flow in 2D spherical polar with $a/M = 0$ BH

Our next test involves the same radiative Bondi problem as in section (5.10) for model E10T7, but now we include a strong monopolar magnetic field with vector potential component $A_\phi \propto (1 - \cos(\theta))$. We choose $b^2/e_{\rm gas} \approx 812$ (giving $b^2/\rho_0 \approx 4.9$) at the horizon at $r = 2M$. The flow is along the magnetic field, so all magnetic forces cancel exactly. This is a difficult test, however, because numerically the magnetic terms cancel only to truncation error, and the small value of $e_{\rm gas}$ has to be recovered from the total energy equation dominated by truncation errors in the magnetic field. This causes problems at high magnetic field strengths, unless one uses the entropy evolution equation that involves lower-order velocity terms. For entropy evolution, we get highly accurate results even if we choose $b^2/e_{\rm gas} \sim 10^5$ and even higher, at relatively lower resolutions.

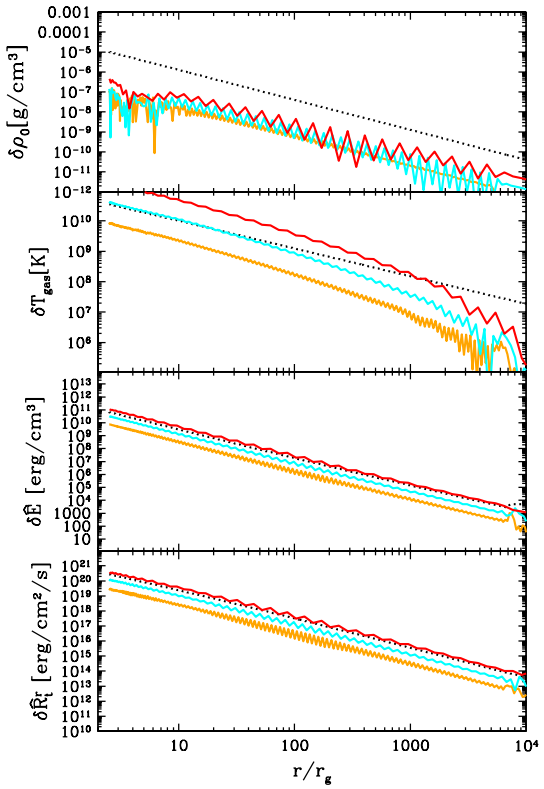

Figure 15. Convergence test for 1D radiative Bondi test (similar quantities plotted as in Fig. (14)). Here we only consider model E10T7 with radial resolutions of 64 (solid red), 128 (solid cyan), 256 (solid orange), and 512 (dotted black) (as used in Fig. (14, where this model is shown as green lines in that other figure)). Model with resolution 512 is directly plotted for reference (dotted black), while remaining models at lower resolutions are plotted as an absolute difference away from the 512 resolution model in order to show the relative error. Shows convergence to correct solution to 2nd order, with most sensitive dependence in temperature.

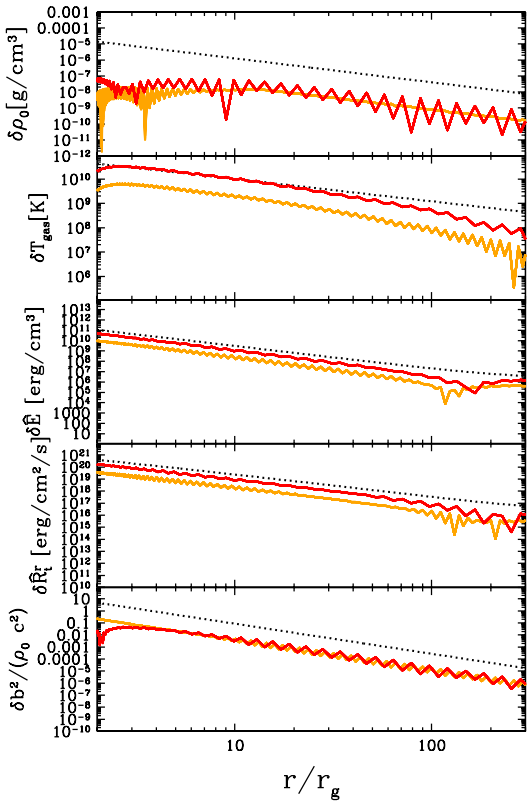

Figure 16. Convergence test for model E10T7 for a relativistically strong radial magnetic field with spherical Bondi accretion with radiation in 2D (until here, our Bondi tests were in 1D). The panels show density (top), gas temperature (2nd), fluid-frame radiative energy density (3rd), fluid-frame radiative radial flux (4th), and $b^2/(\rho_0 c^2)$ (bottom). The 512 resolution model is plotted directly (dotted black) for reference, while the 256 model (orange) and 128 model (red) are plotted as the differences from the 512 model to show convergence. The models have 16 angular cells, and all are shown in the difference. This results show that the code handles well the case of 2D relativistically strong magnetic fields in radiative flows, the angular direction introduces no anisotropy, and the solution converges to 2nd order in the temperature that dominates the error.

We now also solve the problem in Kerr-Schild coordinates in full 2D spherical polar coordinates with resolution $N_r \times N_\theta = 512 \times 16$ with angular span from $\theta = 0$ to π and using $R_{\rm in} = 1.9$, $R_{\rm out} = 2 \times 10^4$, and $R_0 = 1.88$ chosen to allow the energy evolution method to accurately evolve this scenario. This appears to simply be a one-dimensional test, but for HARM it is actually two dimensional. Although the pressure is independent of the Boyer-Lindquist coordinate θ, the θ acceleration does not vanish identically due to round-off error. This is because pressure enters the momentum equations through a flux ($-\partial_\theta(p \sin\theta)$ in the Newtonian limit) and a source term ($p\cos\theta$ in the Newtonian limit). Analytically these terms cancel; numerically they produce an acceleration that is of order the truncation error for the original HARM (Gammie et al. 2003) and round-off error for HARM. This test also exercises many terms in the code because in Kerr-Schild coordinates only three of the ten independent components of the metric are zero.

Fig. 16 shows the model E10T7 in 2D and with the magnetic field. We show resolutions: high (512×16), medium (256×16), and low (128 × 16). While the outer radius is 2×10^4, we only evolved for a finite time and so only show out to $r \sim 300 r_g$.

All resolutions do well, except for a radial resolution of 128 for which the temperature starts to deviate at smaller radii. For even smaller radial resolutions of 64 and 32, the implicit solver fails. This occurs because of the energy equation's limits over such a large dynamic range. An evolution with the entropy equations has no such limits on resolution and the temperature behaves accurately even at low resolutions. Over the span in equilibrium, the simulations converge to at least 2nd order in space in temperature, the quantity that dominates the error. E.g., for any of the first several radial cells, the relative errors are 0.04264 and 0.319 for the 256 and 128 models, respectively.

6 FIDUCIAL FULLY 3D GR RADIATIVE MHD DISK MODEL

As a test of the scheme to handle astrophysically realistic situations, we consider magnetized radiative accretion onto a rotating black hole. This model with black hole mass of $M = 10 M_\odot$ and $a/M = 0.9375$ has nominal thin disk efficiency $\eta_{\rm NT} \approx 17.91\%$, so that $\dot{M}_{\rm Edd} \approx 7.8 \times 10^{18}$g/s (see Eq. 1). Then rescaling $\dot{M}_{\rm Edd}$ by only c, G, and M, we normalize other quantities by letting $\rho_{\rm Edd} \approx 1.2 \times 10^{-4}$g, $u_{\rm Edd} \approx 1.07 \times 10^{17}$erg, and $b_{\rm Edd} \approx 3.2 \times 10^8$G.

We use the same numerical parameters as all prior tests given

in section 5. The implicit solver takes an average of 3.0 iterations per complete solution (including all unused attempts), where 99.8% are from the PMHD method, 0.2% are from the URAD method, and 0.002% are from the PRAD method. Among all used solutions, 99.7% come from the energy-momentum equations, 0.3% come from the entropy-momentum equations, 0% come from the cold MHD equations, and 0.0004% have no solution such that diffusive backups are used. Nearly 100% of those unacceptable solutions occur inside the horizon near the polar axis. As compared to an otherwise identical non-radiative simulation, this simulation is about 2-3 times slower per core, while it operates at slightly higher parallel efficiency because there are more per-core operations between any cross-core Message Passing Interface (MPI) operations.

6.1 Initial Mass Distribution: Polish doughnut and Atmosphere

We set up analytical equilibrium torii (Polish doughnuts, Abramowicz et al. 1978) in the Kerr ($a/M = 0.9375$) metric as initial conditions. For the analytical model, we assume a constant specific angular momentum, $\ell = -u_\phi/u_t =$ constant. From the condition $u^\mu u_\mu = -1$, it follows that

$$u_t^{-2} = -g^{tt} + 2\ell g^{t\phi} - \ell^2 g^{\phi\phi}. \quad (97)$$

We choose the specific internal energy at the inner edge of the torus, $u_{t,\rm in}$, which determines the radius of the inner edge of the torus, and we then calculate the fluid enthalpy, $h = \rho_0 + e_{\rm gas} + p_{\rm gas}$ (e.g., Hawley et al. 1984),

$$h = \frac{u_{t,\rm in}}{u_t}. \quad (98)$$

Using an equation of state $p = \kappa_1 \rho^\Gamma$ (where the constant κ_1 determines the entropy of the torus gas), we obtain

$$\rho_0 = \left[\frac{(h-1)}{\kappa_1}\frac{(\Gamma-1)}{\Gamma}\right]^{1/(\Gamma-1)}, \quad (99)$$

$$u = \rho_0 \frac{(h-1)}{\Gamma}. \quad (100)$$

We set the initial velocity to $v^r = v^\theta = 0$, $v^\phi = u^\phi/u^t$ within the doughnut, and set the gas to the ZAMO velocity outside. We choose $\Gamma = 5/3$, where $\Gamma = 4/3$ may lead to somewhat different results (McKinney & Gammie 2004; Mignone & McKinney 2007). The specific angular momentum is set to be $\ell = 4.5$, $u_{t,\rm in} = 0.9999999$, corresponding to a torus inner radius $r_{\rm in} \approx 8.5$ and pressure maximum at $r_{\rm max} \approx 18 r_g$. We set $\rho_0 = \rho_{\rm max} = 1$ at the maximum rest-mass density. To seed the magneto-rotational instability (MRI), $e_{\rm gas}$ is perturbed by a factor $1 + F_R(E - 0.5)$, where $F_R = 0.1$ and E is a random number from 0 to 1. The torus is surrounded by an atmosphere with $\rho_0 = 10^{-4}(r/r_g)^{-2}$, $e_{\rm gas} = 10^{-6}(r/r_g)^{-5/2}$, $\tilde{u}^i = 0$, and $B^i = 0$. The density can consistently drop to zero in the jet that emerges, so we use a numerical density floor that ensures a maximum of $b^2/\rho_0 = 200$, maximum of $b^2/e_{\rm gas} = 10^5$, and maximum of $e_{\rm gas}/\rho_0 = 10^{10}$.

6.2 Initial Magnetic Field

We consider an initial poloidal field geometry that does not lead to magnetic flux saturation near the BH, so a magnetically arrested disk (MAD) or magnetically choked accretion flow (MCAF) does not form. A single set of field loop of a single polarity are inserted. For this poloidal field geometry, the ϕ-component of the magnetic vector potential is

$$\begin{aligned} \underline{A}_\phi &\propto f_1 f_2, \quad (101)\\ f_1 &= |q|^p |r\sin(\theta)|^\nu,\\ q &= u_{\rm g}/u_{\rm g,max} - f_c,\\ f_2 &= \sin(\log(r/S)/T), \end{aligned}$$

where f_1 has $p = 1$ and $\nu = 2$, q has $f_c = 0.2$, $u_{\rm gas,max}$ is the maximum $e_{\rm gas}$, $q = 0$ is set if $q < 0$, and f_2 has $S = 0.5 r_{\rm in}$ and $T = 0.28$ for the flipping field and $f_2 = 1$ for the non-flipping field.

The magnetic field strength is set via the plasma $\beta = p_{\rm gas}/p_b \sim (2/\Gamma)(c_s/v_a)^2$ where $v_a^2 = b^2/(\rho_0 + e_{\rm gas} + p_{\rm gas} + b^2)$ gives the Alfvén speed v_a. Our model has $\beta_{\rm min}$, the smallest value of β (within the resolved disk region, e.g., $r \sim 1000 r_g \ll R_{\rm out}$) of $\beta_{\rm min} \approx 100$. An alternative measure is $\beta_{\rm rat-of-maxes} \equiv p_{\rm gas,max}/p_{b,\rm max} \approx 240$, where $p_{\rm gas,max}$ is the maximum thermal pressure on the domain and $p_{b,\rm max}$ is the maximum magnetic pressure on the domain. Another alternative is $\beta_{\rm rat-of-avg} \equiv p_{\rm gas,avg}/p_{b,\rm avg} = \langle p_{\rm gas}\rangle/\langle p_b\rangle \approx 3800$. These β are computed with condition $b^2/\rho_0 < 1$. Our choices for β ensure that $S_{d,\rm MRI} > 1$ so the MRI operates, while we push close to $S_{d,\rm MRI} \sim 1$.

6.3 Initial Radiation

The initial solution solves for the hydrostatic equilibrium torus with $\Gamma = 4/3$ (which is the correct value for a radiation pressure dominated disk). This pressure is then assumed to be the actual total pressure $p_{\rm tot}$, which is then distributed between gas and radiation so as to satisfy local thermal equilibrium (LTE, $\widehat{E} = a_{\rm rad} T^4$) based upon a single temperature satisfying

$$p_{\rm tot} = p_{\rm gas} + p_{\rm rad} = k_{\rm B}\rho_0 T + \frac{1}{3} a_{\rm rad} T^4. \quad (102)$$

Once this initial state has been set, we reset $\Gamma = 5/3$ for a nonrelativistic gas. Because the gas is very optically thick, the initial state holds hydro-radiation-static equilibrium to good accuracy.

The radiative fluxes in each direction i are set as based upon the flux-limited diffusion approximation

$$F_i = -\frac{c}{\kappa_{\rm tot}}\frac{dp_{\rm rad}}{dx^i}, \quad (103)$$

where the orthonormal gas-fluid frame radiation fluxes are limited to $|F| < 0.7\widehat{E}$.

6.4 Numerical Grid

The uniform spatial coordinates $\underline{x}^{(i)}$ have resolution $N_r \times N_\theta \times N_\phi$ active grid cells and 4 boundary cells for each of the 6 boundaries in 3D. The radial grid of $N_r = 256$ cells spans from $R_{\rm in}$ to $R_{\rm out}$ with mapping

$$r(x^{(1)}) = R_0 + \exp f[\underline{x}^{(1)}] \quad (104)$$

where $R_0 = 0.2$ is chosen in this paper. For $\underline{x}^{(1)} < x_{\rm break}$

$$f[\underline{x}^{(1)}] = n_0 \underline{x}^{(1)}, \quad (105)$$

where $x_{\rm break} = \log(r_{\rm break} - R_0)/n_0$ (with $n_0 = 1$), and otherwise

$$f[\underline{x}^{(1)}] = n_0 \underline{x}^{(1)} + c_2(\underline{x}^{(1)} - x_{\rm break})^{n_2}, \quad (106)$$

where $c_2 = 1$, and $n_2 = 10$. The $\underline{x}^{(1)}$ grid ranges from $\underline{x}_s^{(1)} = (\log(R_{\rm in} - R_0))/n_0$ to $\underline{x}_f^{(1)}$, which is $\underline{x}_f^{(1)} = (\log(R_{\rm out} - R_0))/n_0$ if $R_{\rm out} < r_{\rm break}$ and otherwise determined iteratively from $R_{\rm out} = r[\underline{x}_f^{(1)}]$. The

value of $R_{\rm in} = 1.1 \approx 0.816 r_{\rm H}$ is chosen so that there are 6 active grid cells inside the outer horizon, while $R_{\rm in}$ is outside the inner horizon. So the boundary cells only connect to stencils (each ±4 cells) that are inside the horizon, which avoids causal connection between the inner boundary and the flow outside the horizon. We set $R_{\rm out} = 10^4 r_g$ and $r_{\rm break} = 5 \times 10^2 r_g$. The radius $r_{\rm break}$ is where the grid changes from exponential to hyper-exponential, which allows the grid to focus on the dynamics at small radii while avoiding numerical reflections off the outer grid. Radial boundaries use absorbing conditions.

The θ-grid of $N_\theta = 128$ cells spans from 0 to π with mapping

$$\theta(\underline{x}^{(2)}) = \Theta_2 + W(\Theta_1 - \Theta_2) \quad (107)$$

where $\underline{x}^{(2)}$ ranges from 0 to 1 (i.e. no polar cut-out ; but see Appendix 4). The first grid mapping function is given by

$$\begin{aligned}
\Theta_1 &= T_0 S_2 + T_2 S_0, \quad (108)\\
T_2 &= (\pi/2)(1 + \arctan(h_2(\underline{x}^{(m2)} - (1/2)))/\arctan(h_2/2)),\\
h_2 &= h_3 + ((r - r_{sj3})/r_{0j3})^{n_{j1}},\\
T_0 &= \pi \underline{x}^{(2)} + ((1-h_0)/2)\sin(2\pi \underline{x}^{(2)}),\\
h_0 &= 2 - Q_j (r/r_{1j})^{-n_{j2}((1/2)+(1/\pi)\arctan(r/r_{0j} - r_{sj}/r_{0j}))},\\
S_2 &= (1/2) - (1/\pi)\arctan((r - r_s)/r_0),\\
S_0 &= (1/2) + (1/\pi)\arctan((r - r_s)/r_0),
\end{aligned}$$

where $r_s = 40$ and $r_0 = 20$. For h_2, we set $h_3 = 0.3$, $r_{0j3} = 20$, $r_{sj3} = 0$, and $n_{j1} = 1$ so the jet is resolved with grid lines following $\theta_j \propto r^{-n_{j1}}$. For h_0, we set $r_{1j} = 2.8$, $n_{j2} = 1$, $r_{0j} = 15$, $r_{sj} = 40$, and $Q_j = 1.3$. We set $\underline{x}^{(m2)} = \underline{x}^{(2)}$ unless $\underline{x}^{(2)} > 1$ then $\underline{x}^{(m2)} = 2 - \underline{x}^{(2)}$ and unless $\underline{x}^{(2)} < 0$ then $\underline{x}^{(m2)} = -\underline{x}^{(2)}$. Θ_1 focuses on the disk at small radii and the jet at large radii. The second mapping function is

$$\Theta_2 = (\pi/2)(h_\theta(2\underline{x}^{(2)} - 1) + (1 - h_\theta)(2\underline{x}^{(2)} - 1)^{n_\theta} + 1), \quad (109)$$

where $n_\theta = 5$ and $h_\theta = 0.15$. Θ_2 focuses on the thin inflow near the horizon in poloidal field models, while it also avoids small ϕ polar cells that would limit the time step. The interpolation factor is

$$W = (1/2) + (1/\pi)(\arctan((r - r_{sj2})/r_{0j2})), \quad (110)$$

where $r_{sj2} = 5$ and $r_{0j2} = 2$. The polar axis boundary condition is transmissive as described in Appendix 4.

The ϕ-grid of $N_\phi = 64$ cells spans from 0 to 2π with mapping $\phi(\underline{x}^{(3)}) = 2\pi \underline{x}^{(3)}$. Many of our simulations have $\underline{x}^{(3)}$ vary from 0 to 1 such that $\Delta\phi = 2\pi$. This is a fully 3D (no assumed symmetries) domain. Periodic boundary conditions are used in the ϕ-direction.

We choose a resolution $N_r \times N_\theta \times N_\phi$ that has a grid aspect ratio of 1:1:1 for most of the inner-radial domain. This allows the ϕ dimension to be treated equally to the $r - \theta$ dimensions. The aspect ratio (as volume-averaged within $|\theta - \pi/2| \leqslant [\theta^d]_t$) is given as A_r for radius r. We measure $A_{r_{\rm H}} \approx 1.1 : 1 : 8$, $A_{12} \approx 1 : 1 : 3$, and $A_{14} \approx 1 : 2 : 3$, where $r_{\rm H}$ is the horizon. There are about 14 vertical cells resolving the disk at the horizon where the disk thins-out.

6.5 Resolving the MRI and Turbulence

The MRI is a linear instability with fastest growing wavelength of

$$\lambda_{x,\rm MRI} \approx 2\pi \frac{|v_{x,\rm A}|}{|\Omega_{\rm rot}|}, \quad (111)$$

for $x = \theta, \phi$, where $|v_{x,\rm A}| = \sqrt{\underline{b}_x \underline{b}^x/\epsilon}$ is the x-directed Alfvén speed, $\epsilon \equiv b^2 + \rho_0 + e_{\rm gas} + p_{\rm gas}$, and $r\Omega_{\rm rot} = v_{\rm rot}$. $\lambda_{\rm MRI}$ is accurate for $\Omega_{\rm rot} \propto r^{-5/2}$ to r^{-1}. $\Omega_{\rm rot}, v_{\rm A}$ are separately angle-volume-averaged at each r, t.

The MRI is resolved for grid cells per wavelength (Eq. (111)),

$$Q_{x,\rm MRI} \equiv \frac{\lambda_{x,\rm MRI}}{\Delta_x}, \quad (112)$$

of $Q_{x,\rm MRI} \geqslant 6$, for $x = \theta, \phi$, where $\Delta_r \approx d\underline{x}^{(1)}(dr/d\underline{x}^{(1)})$, $\Delta_\theta \approx r d\underline{x}^{(2)}(d\theta/d\underline{x}^{(2)})$, and $\Delta_\phi \approx r \sin\theta d\underline{x}^{(3)}(d\phi/d\underline{x}^{(3)})$. Volume-averaging is done as with $S_{d,\rm MRI}$, except $v_{x,\rm A}/\Delta_x$ and $|\Omega_{\rm rot}|$ are separately θ, ϕ-volume-averaged before forming $Q_{x,\rm MRI}$. The $t = 0$ values and time-averaged values are measured at same radii as $S_{d,\rm MRI}$, and we find $Q_{\theta,\rm MRI} \approx 8$ and $S_{d,\rm MRI} \approx 2$ near the pressure maximum.

The MRI suppression factor corresponds to the number of MRI wavelengths across the full disk:

$$S_{d,\rm MRI} \equiv \frac{2r\theta^d}{\lambda_{\theta,\rm MRI}}. \quad (113)$$

Wavelengths $\lambda < 0.5\lambda_{\theta,\rm MRI}$ are stable, so the linear MRI is suppressed for $S_{d,\rm MRI} < 1/2$ when no unstable wavelengths fit within the full disk (Balbus & Hawley 1998; Pessah & Psaltis 2005). $S_{d,\rm MRI}$ (or $S_{d,\rm weak,MRI}$) uses averaging weight $w = (b^2\rho)^{1/2}$ (or $w = \rho$), condition $\beta > 1$, and excludes regions where density floors are activated. Weight $w = (b^2\rho)^{1/2}$ is preferred, because much mass flows in current sheets where the magnetic field vanishes and yet the MRI is irrelevant. When computing the averaged $S_{d,\rm MRI}$, $v_{\rm A}$ and $|\Omega_{\rm rot}|$ are separately θ, ϕ-volume-averaged within $\pm 0.2r$ for each t, r. The averaged $S_{d,\rm MRI}$ is at most 30% smaller than $S_{d,\rm weak,MRI}$.

6.6 Modes and Correlation Lengths

The flow structure is studied via the discrete Fourier transform of dq (related to quantity Q) along $x = r, \theta, \phi$ giving amplitude a_p for $p = n, l, m$, respectively. The averaged amplitude is

$$\left\langle |a_p| \right\rangle \equiv \left\langle |\mathcal{F}_p(dq)| \right\rangle \equiv \int_{\rm not\ x} \left| \sum_{k=0}^{N-1} dq\ {\rm e}^{\frac{-2\pi i p k}{N-1}} \right|, \quad (114)$$

computed at $r = r_{\rm H}, 4r_g, 8r_g, 30r_g$. The x is one of r, θ, ϕ and "not x" are others (e.g. θ, ϕ for $x = r$). The dq is (generally) a function of x on a uniform grid indexed by k of N cells that span: δr equal to $0.75r$ around r for $x = r$, π for $x = \theta$, and 2π for $x = \phi$. The N is chosen so all structure from the original grid is resolved, while the span covered allows many modes to be resolved.

For all x, $dq \equiv \sqrt{-g} d\underline{x}^{(1)} d\underline{x}^{(2)} d\underline{x}^{(3)} \delta Q/q_N$. For $x = r, \theta$, we let $q_N = \int_{\rm not\ x} \sqrt{-g} d\underline{x}^{(1)} d\underline{x}^{(2)} d\underline{x}^{(3)} \langle [Q]_t \rangle$, $\langle [Q]_t \rangle$ as the time-ϕ averaged Q, and $\delta Q = Q - \langle [Q]_t \rangle$. Using dq removes gradients with r, θ so the Fourier transform acts on something closer to periodic with constant amplitude (see also Beckwith et al. 2011). For $x = \phi$, we let $q_N = 1$ and $\delta Q = Q$ because the equations of motion are ϕ-ignorable. For $x = \theta, \phi$, the radial integral is computed within $\pm 0.1r$. For $x = r, \theta$, the ϕ integral is over all 2π. For $x = r, \phi$, the θ integral is over all π. For all x cases, the θ range of values uses the "fdc" or "jet" conditions (respectively called "Disk" and "Jet", where these conditional regions are defined via ϕ-averaged quantities at each time. Notice we average the mode's absolute amplitude, because the amplitude of $\langle \delta Q \rangle$ de-resolves power (e.g. $m = 1$ out of phase at different θ gives $\langle \delta Q \rangle \to 0$ and $a_m \to 0$) and is found to underestimate small-scale structure.

We also compute the correlation length: $\lambda_{x,\rm cor} = x_{\rm cor} - x_0$, where $x_0 = 0$ for $x = \theta, \phi$ and x_0 is the inner radius of the above given radial span for $x = r$, where $n_{\rm cor} = \delta r/\lambda_{r,\rm cor}$, $l_{\rm cor} = \pi/\lambda_{\theta,\rm cor}$, and $m_{\rm cor} = (2\pi)/\lambda_{\phi,\rm cor}$. The Wiener-Khinchin theorem for the auto-correlation gives

$$\exp(-1) = \frac{\mathcal{F}^{-1}_{x=x_{\rm cor}}[\langle |a_{p>0}| \rangle^2]}{\mathcal{F}^{-1}_{x=x_0}[|\langle a_{p>0} \rangle|^2]}, \quad (115)$$

where $\mathcal{F}^{-1}[\langle|a_{p>0}|\rangle^2]$ is the inverse discrete Fourier transform of $\langle|a_p|\rangle^2$ but with $\langle a_0\rangle$ reset to 0 (i.e. mean value is excluded).

Turbulence is resolved for grid cells per correlation length (Eq. (115)),

$$Q_{p,\rm cor} \equiv \frac{\lambda_{x,\rm cor}}{\Delta_x}, \tag{116}$$

of $Q_{p,\rm cor} \geqslant 6$, for $x = r,\theta,\phi$ and $p = n,l,m$, respectively. Otherwise, modes are numerically damped on a dynamical timescale (even $Q = 5$ would not indicate the mode is marginally resolved, because numerical noise can keep $Q \approx 5$ at increasing resolution until finally the mode is actually resolved – finally leading to an increasing $Q \geqslant 6$ with increasing resolution ; as seen by Shiokawa et al. 2012). Reported $Q_{p,\rm cor}$ take $1/\Delta_x$ as the number of grid cells covering the span of $\lambda_{x,\rm cor}$ as centered on: middle of $x^{(1)}$ within the used radial span for $x = r$, $\theta = \pi/2$ for $x = \theta$ for the "Disk" and $\theta = 0$ for $x = \theta$ for the "Jet", and anywhere for $x = \phi$. For $\Delta\phi < 2\pi$, $Q_{\phi,\rm MRI}, Q_{m,\rm cor} \ll N_\phi$ is required to avoid truncating the mode.

6.7 Diagnostics

Diagnostics are computed from snapshots produced every $\sim 4r_g/c$. For quantities Q, averages over space ($\langle Q\rangle$) and time ($[Q]_t$) are performed directly on Q (e.g. on v_ϕ rather than on any intermediate values). Any flux ratio vs. time with numerator F_N and denominator F_D (F_D often being mass or magnetic flux) is computed as $R(t) = \langle F_N(t)\rangle/[\langle F_D\rangle]_t$. Time-averages are then computed as $[R]_t$.

6.7.1 Fluxes and Averages vs. Radius

For flux density F_d, the flux integral is

$$F(r) \equiv \int dA_{23} F_d, \tag{117}$$

where $dA_{23} = \sqrt{-g}d\underline{x}^{(2)}d\underline{x}^{(3)}$ ($dA_{\theta\phi}$ is the spherical polar version). For example, $F_d = \rho_0\underline{u}^{(1)}$ gives $F = \dot{M}_0$, the rest-mass accretion rate. For weight w, the average of Q is

$$Q_w(r) \equiv \langle Q\rangle_w \equiv \frac{\int dA_{\theta\phi} wQ}{\int dA_{\theta\phi} w}, \tag{118}$$

All θ,ϕ angles are integrated over.

6.7.2 Fluxes and Averages vs. θ

The flux angular distribution, at any given radius, is

$$F(\theta) = \int_{\theta'=0}^{\pi/2-|\theta-\pi/2|} dA_{\theta'\phi} F_d + \int_{\theta'=\pi/2+|\theta-\pi/2|}^{\pi} dA_{\theta'\phi} F_d, \tag{119}$$

which just integrates up from both poles towards the equator, is symmetric about the equator, and gives the total flux value at $\theta = \pi/2$. The average of Q vs. θ using weight w is given by

$$Q_w(\theta) = \frac{\int dA_{\theta\phi} wQ}{\int dA_{\theta\phi} w}. \tag{120}$$

All ϕ-angles are integrated over.

6.7.3 Disk Thickness Measurements

The disk's geometric half-angular thickness is given by

$$\theta^d \equiv \left\langle\left\langle(\theta-\theta_0)^2\right\rangle_\rho\right\rangle^{1/2}, \tag{121}$$

where we integrate over all θ for each r,ϕ, and $\theta_0 \equiv \pi/2 + \langle(\theta-\pi/2)\rangle_\rho$ is also integrated over all θ for each r,ϕ, and the final $\theta^d(r)$ is from ϕ-averaging with no additional weight or $\sqrt{-g}$ factor. This way of forming $\theta^d(r)$ works for slightly tilted thin disks or disordered thick disks. For a Gaussian distribution in density, this satisfies $\rho/(\rho[\theta=0]) \sim \exp(-\theta^2/(2(\theta^d)^2))$. For sound speed $c_s = \sqrt{\Gamma p_{\rm gas}/(\rho_0 + e_{\rm gas} + p_{\rm gas})}$, the thermal half-angular thickness is

$$\theta^t_w \equiv \arctan\left(\frac{\langle c_s\rangle_w}{\langle v_{\rm rot}\rangle_w}\right), \tag{122}$$

where $v^2_{\rm rot} = v^2_\phi + v^2_\theta$. For a thin hydrostatic non-relativistic Keplerian (i.e. $v_{\rm rot} = |v_{\rm K}|$ with $v_{\rm K} \approx R/(a+R^{3/2})$) Gaussian disk, $\theta^d = c_s/v_{\rm rot}$ for c_s and $v_{\rm rot}$ at the disk plane. Also, $\theta^t_\rho \approx 0.93\theta^d$ for $\Gamma = 4/3$. Ram pressure forces (Beskin & Tchekhovskoy 2005) and magnetic forces (Cao 2011) can cause $\theta^d \ll \theta^t$. Note that ADAFs have $\theta^t \gtrsim 1$ (Narayan & Yi 1994).

6.7.4 BH, Disk, Jet, Magnetized Wind, and Entire Wind

Many quantities (Q) vs. r or vs. θ or vs. ϕ are considered for various weights and conditions. We define the superscript "f" (full flow) case as applies for weight $w = 1$ with no conditions, "fdc" (full flow except avoids highly magnetized jet where numerical floors are activated), "dc" (disk plus corona but no jet) case as applies for $w = 1$ with condition $b^2/\rho_0 < 1$, "dcden" (density-weighted average) with $w = \rho$ and no conditions, "θ^d" (within 1 disk half-angular thickness) case with $w = 1$ and condition of $|\theta-\theta_0| < \theta^d$, "eq" (within 3 cells around the equator) case with $w = 1$, and "jet" or "j" case (jet only) with $w = 1$ and the condition that density floors are activated (see Appendix 4). For quantities vs. θ or vs. ϕ, we radially average within $\pm 0.1r$ at radius r.

Fluxes, described in the next section, have integrals computed for a variety of (somewhat arbitrary) conditions. The subscript "BH" or "H" is for all angles on the horizon. The subscript "j" or "jet" is for the "jet" with condition $b^2/\rho_0 \geqslant 1$. When the jet is measured at a single radius, we use $r = 50r_g$ (except the MB09Q model that uses $r = 30r_g$ due to its limited radial range). The subscript "mw" is for the "magnetized wind" with conditions $b^2/\rho_0 < 1$ and $\beta < 2$ for all fluxes, except for the rest-mass flux that also has $-(\rho_0 + e_{\rm gas} + p_{\rm gas})\underline{u}_t/\rho_0 > 1$ (i.e. thermo-kinetically unbound). The "w" or "wind" subscript is for the "entire wind" with the condition of $b^2/\rho_0 < 1$ that includes all of the flow except the jet. The subscript is "in" ("out") for the condition $u_r < 0$ ($u_r > 0$).

6.7.5 Fluxes of Mass, Energy, and Angular Momentum

The gas rest-mass flux, specific energy flux, and specific angular momentum flux are respectively given by

$$\dot{M}_0 = \left|\int \rho_0\underline{u}^r dA_{\theta\phi}\right|, \tag{123}$$

$$\mathrm{e} \equiv \frac{\dot{E}}{[\dot{M}_0]_t} = -\frac{\int(T^r_t + R^r_t)dA_{\theta\phi}}{[\dot{M}_0]_t}, \tag{124}$$

$$\jmath \equiv \frac{\dot{J}}{[\dot{M}_0]_t} = \frac{\int(T^r_\phi + R^r_\phi)dA_{\theta\phi}}{[\dot{M}_0]_t}, \tag{125}$$

as computed in Table 6.12.

The net flow efficiency is given by

$$\eta = \frac{\dot{E} - \dot{M}_0}{[\dot{M}_0]_t} = \frac{\dot{E}^{\rm EM}(r) + \dot{E}^{\rm MAKE}(r) + \dot{E}^{\rm RAD}(r)}{[\dot{M}_{\rm H}]_t}. \quad (126)$$

Positive values correspond to an extraction of positive energy from the system at some radius. One can break-up the efficiency into contributions from each PAKE, EM, and RAD components to give $\eta_{\rm PAKE}$, $\eta_{\rm EM}$ and $\eta_{\rm RAD}$ as measured at various locations (horizon, jet, etc.) or radii. These η's are computed in Table 6.12.

The BH's dimensionless spin-up parameter is

$$s \equiv \frac{d(a/M)}{dt}\frac{M}{[\dot{M}_0]_t} = -\jmath - 2\frac{a}{M}(1-\eta), \quad (127)$$

(computed in Table 6.12). All θ and ϕ angles are integrated over. The BH is in "spin equilibrium" for $s = 0$ (Gammie et al. 2004).

6.7.6 Magnetic Flux

The radial magnetic flux vs. θ at any radius is

$$\Psi_r(r,\theta) = \int dA_{\theta\phi}\underline{B}^r. \quad (128)$$

The signed value of the maximum absolute value over all θ angles (smaxa$_\theta$) of the magnetic flux is

$$\Psi_{\rm t}(r) \equiv {\rm smaxa}_\theta \Psi_r, \quad (129)$$

and $\Psi_{\rm tH} \equiv \Psi_{\rm t}(r = r_{\rm H})$ is the horizon's magnetic flux. The half-hemisphere horizon flux is

$$\Psi_{\rm H} \equiv \Psi_r(r = r_{\rm H}), \quad (130)$$

as integrated from $\theta = \pi/2$ to π (negative compared to the integral from $\theta = 0$ to $\pi/2$). The θ magnetic flux vs. radius at angle θ is

$$\Psi_\theta(r,\theta) = \int_{r_{\rm H}}^{r} \sqrt{-g} d\underline{x}^{(1)} d\underline{x}^{(3)} \underline{B}^{\underline{x}^{(2)}}, \quad (131)$$

where the vertical magnetic flux threading the equator is

$$\Psi_{\rm eq}(r) \equiv \Psi_\theta(r, \theta = \pi/2). \quad (132)$$

The total magnetic flux along the equator is

$$\Psi(r) \equiv \Psi_{\rm H} + \Psi_{\rm eq}(r). \quad (133)$$

For all forms of Ψ, all ϕ-angles are integrated over.

The magnetic flux can be normalized in various ways (as computed in Table 6.12). Normalization by the initial flux at r_0 gives $\Psi(r)/\Psi(r_0)$. One type of field geometry we will use has multiple field loops of alternating polarity as a function of radius. So another normalization is by the initial i-th extrema vs. radius, which gives Ψ/Ψ_i that picks up the extrema in the magnetic flux over each field loop. Normalization by the initial value of an extrema gives $\Psi/\Psi_i(t = 0)$. We also need to form a measure that indicates how much flux is available to the BH. So we consider the normalization by the flux in the disk that is immediately available to the horizon of the same polarity. This measure is given by $\Psi_{\rm H}/\Psi_a$, where Ψ_a is the value where $\Psi(r)$ goes through its first extremum of the same sign of magnetic flux (i.e. out to the radius with the same polarity of dipolar-like field) as on the horizon. If the horizon value is itself an extremum, then $\Psi_{\rm H}/\Psi_a = 1$ implying that the region immediately beyond the horizon only has opposite polarity field.

The absolute magnetic flux (Φ) is computed similarly to Ψ, except one 1) inserts absolute values around the field (e.g. $\underline{B}^r$ and $\underline{B}^\theta$ in the integrals); 2) puts absolute values around the integral ; and 3) divides by 2 so that a dipolar field has $|\Psi_{\rm t}| = \Phi$. For example, $\Phi_r(r,\theta) = (1/2)\left|\int dA_{\theta\phi}|\underline{B}^r|\right|$. The quantity $\Phi/\Psi_{\rm t}$ (computed in Table 6.12, and which is the only flux ratio directly time-averaged as $[\Phi/\Psi_{\rm t}]_t$) is roughly the vector spherical harmonic multipole l of the ϕ-component of the magnetic vector potential:

$$\underline{A}_\phi = \int_{\theta'=0}^{\theta} \sqrt{-g}\underline{B}^r d\theta' \quad (134)$$

as integrated over all ϕ. For example, for $l = \{1 \ldots 8\}$ one gets $|\Phi/\Psi_{\rm t}| = 1, 2, 2.6, 3.5, 4, 5.6, 5.7$, and 6.7.

The Gammie (1999) model normalization gives

$$\Upsilon \approx 0.7\frac{\Phi_r}{\sqrt{[\dot{M}_0]_t}}, \quad (135)$$

which accounts for Φ_r being in Heaviside-Lorentz units (Penna et al. 2010). Compared to Gaussian units version of $\phi_{\rm H} \equiv \Phi_{\rm H}/\sqrt{\dot{M}_0 r_g^2 c}$ defined in Tchekhovskoy et al. (2011), $\Upsilon \approx 0.2\phi_{\rm H}$. $\Upsilon_{\rm H}$ and Υ_j are normalized by $\dot{M}_{\rm H}$, $\Upsilon_{\rm in}$ by $\dot{M}_{\rm in}$, and $\Upsilon_{\rm mw}$ and $\Upsilon_{\rm w}$ respectively by $\dot{M}_{\rm mw}$ and $\dot{M}_{\rm w}$. Υ is computed in Table 6.12.

The field line rotation frequency with respect to the BH spin (z) axis is computed various ways. We consider $\Omega_{\rm F}^a \equiv F_{tr}/F_{r\phi}$, $\Omega_{\rm F}^b \equiv F_{t\theta}/F_{\theta\phi}$, $\Omega_{\rm F}^c \equiv |\underline{v}^\phi| + {\rm sign}[\underline{u}^r](v_p/B_p)|\underline{B}^\phi|$ with $v_p = \sqrt{v_r^2 + v_\theta^2}$ and $B_p = \sqrt{B_r^2 + B_\theta^2}$, and

$$\Omega_{\rm F} \equiv \Omega_{\rm F}^d \equiv \underline{v}^\phi - \underline{B}^\phi\left(\frac{v_r B_r + v_\theta B_\theta}{B_r^2 + B_\theta^2}\right). \quad (136)$$

We also consider $\Omega_{\rm F}^e = [|F_{t\theta}|]_t/[|F_{\theta\phi}|]_t$. These $\Omega_{\rm F}$ are normalized by the BH rotation angular frequency $\Omega_{\rm H} = a/(2Mr_{\rm H})$.

6.7.7 Inflow Equilibrium and α Viscosity

Inflow equilibrium is defined as when the flow is in a complete quasi-steady-state and the accretion fluxes are constant (apart from noise) vs. radius and time. The inflow equilibrium timescale is

$$t_{\rm ie} = N\int_{r_i}^{r_{\rm ie}} dr\left(\frac{-1}{[\langle v_r\rangle_\rho]_t}\right), \quad (137)$$

for N inflow times from $r = r_{\rm ie}$ and $r_i = 12r_g$ to focus on the more self-similar flow. $t_{\rm ie}$ is used in Table 6.12, where $r_{\rm i}^{\rm dcden} = r_i$, $r_{\rm f}^{\rm dcden} = r_{\rm ie}$ with $N = 1$, and $r_{\rm o}^{\rm dcden}$ uses $r_{\rm ie}$ with $N = 3$.

Viscous theory gives a GR α-viscosity estimate for v_r of $v_{\rm visc} \sim -G\alpha(\theta^d)^2|v_{\rm rot}|$ (Page & Thorne 1974; Penna et al. 2010), with GR correction G ($\lesssim 1.5$ for $r \gtrsim 58r_g$) and (not the lapse)

$$\begin{aligned}
\alpha &= \alpha_{\rm PA} + \alpha_{\rm EN} + \alpha_{\rm M1} + \alpha_{\rm M2}, \quad (138)\\
\alpha_{\rm PA} &\approx \frac{\rho_0 \delta u_r(\delta\underline{u}_\phi\sqrt{g^{\phi\phi}})}{p_{\rm tot}},\\
\alpha_{\rm M2} &\approx -\frac{b_r(\underline{b}_\phi\sqrt{g^{\phi\phi}})}{p_{\rm tot}},\\
\alpha_{\rm mag} &\approx -\frac{b_r(\underline{b}_\phi\sqrt{g^{\phi\phi}})}{p_b},\\
\alpha_{\rm eff} &\equiv \frac{v_r}{v_{\rm visc}/\alpha},
\end{aligned}$$

$\alpha_{\rm eff2} \equiv \alpha_{\rm eff}(|v_{\rm rot}|/|v_{\rm K}|)$, and (small) $\alpha_{\rm EN} \approx (e_{\rm gas} + p_{\rm gas})\delta u_r(\delta\underline{u}_\phi\sqrt{g^{\phi\phi}})/p_{\rm tot}$ and $\alpha_{\rm M1} \approx b^2\delta u_r(\delta\underline{u}_\phi\sqrt{g^{\phi\phi}})/p_{\rm tot}$. Here, δu is the deviation of the velocity from its average (taken over all ϕ and over the time-averaging period). The α (e.g. in Table 6.12) is averaged as follows. The numerator and denominator are

separately volume averaged in θ, ϕ for each r. Weight $w = 1$ with condition $b^2/\rho_0 < 1$ gives α_a for the disk+corona, while $w = \rho$ gives α_b for the heavy disk. Notice $\alpha_{\rm M2} = \alpha_{\rm mag}/(1+\beta_{\rm mag})$ for some β denoted $\beta_{\rm mag}$, and $\sin(2\theta_b) = \alpha_{\rm mag}$ for tilt angle θ_b (Sorathia et al. 2012). These α's are accurate for $|v| \ll c$ as true for $r \gtrsim 2r_g$ in our models, while $\alpha_{\rm eff}$ is accurate far outside the inner-most stable circular orbit (ISCO).

6.7.8 *Optical Depth*

The optical depth of the flow is computed in two ways. One way is as the optical depth away from the polar axis:

$$\tau_a \approx \int_0^\theta \gamma\kappa_{\rm tot}\sqrt{g_{\theta\theta}}\,{\rm d}\theta', \tag{139}$$

which assumes the flow is mostly radial, relativistic, and the region near the polar axis is often optically thin at the radius this is computed. Another way we compute the optical depth is radially:

$$\tau_b \approx \int_{r_0}^r \kappa_{\rm tot}\sqrt{g_{rr}}/(2\gamma)\,{\rm dr}', \tag{140}$$

which assumes the flow is mostly radial, relativistic, and the region at large distance is optically thin or has no additional structure that would affect the optical depth. The flow's radiative photosphere is then defined as either $\tau_a = 1$ or $\tau_b = 1$.

The luminosity of the accretion system is computed as the radiative flux emerging from some chosen radius via

$$L_{\rm rad} = \int dA_{\theta\phi}R^r_t, \tag{141}$$

where we only include those angles where the gas is optically thin (i.e. only that gas that has $\tau_a < 1$).

6.8 Initial and Evolved Disk Structure

Fig. 17 and Fig. 18 show color plots of ρ_0 and field line contours (contours of $\underline{A}_\phi$ integrated over ϕ, so is axially symmetric) for the initial and quasi-steady-state evolved solution, respectively. The initial solution consists of a radially extended thick torus within which a single weak field loop (of single poloidal polarity) is embedded. The disk is geometrically thick with $\theta^d \sim 0.4$.

The evolved solution, shown in Fig. 18, show the simulation when the region within $r \sim 14r_g$ has become quasi-steady. The inner part of the poloidal field loop has accreted onto the black hole. A plot of the radiation energy density closely follows that for the rest-mass density.

Fig. 19 shows a 3D rendering of the flow's three main structural elements (hot radiation-dominated component, hot gas, and relativistic magnetized jet).

6.9 Overall Time Dependence

Fig. 20 shows a typical snapshot for the rest-mass density, field lines, and fluxes ($\dot{M}_0$, Υ, and η) on the BH, through $r = 50r_g$ in the jet, and at $r = 50r_g$ in the magnetized wind. The BH's magnetic flux dominates the mass influx with $\Upsilon_{\rm H} \approx 3$ during the quasi-steady-state period. Because $\Upsilon \gtrsim 1$, one expects the Blandford-Znajek (BZ) effect to be activated, and the energy extraction efficiency is moderate at $\eta \sim 20\%$. Much of the energy extracted from the BH reaches the jet at large radii (i.e. $\eta_{\rm j} \sim 0.3\eta_{\rm H}$).

Fig. 21 shows various quantities vs. time. All quantities are in a quasi-steady-state for $t \gtrsim 3000r_g/c$. The mass ejected in the circulating wind ($\dot{M}_{\rm w,o}$ dominates the magnetized wind ($\dot{M}_{\rm mw,o}$) and jet ($\dot{M}_{\rm j}$) at large radii ($r_{\rm o} = 50r_g$ here); see §6.7.4 for definitions of various outflow components. The MAKE term most often dominates the EM term in $\eta_{\rm H}$ and $_{\rm JH}$. The RAD term is always negative, indicating absorption of positive energy radiation into the BH. The flow has a moderate average total efficiency of $\eta_{\rm H} \sim 20\%$. Note that the MAKE term is composed of a particle term (i.e. $\eta^{\rm PAKE} = 1 + \underline{u}_t$) and an enthalpy term (i.e. $\eta^{\rm EN} = \underline{u}_t(e_{\rm gas} + p_{\rm gas})/\rho_0$).

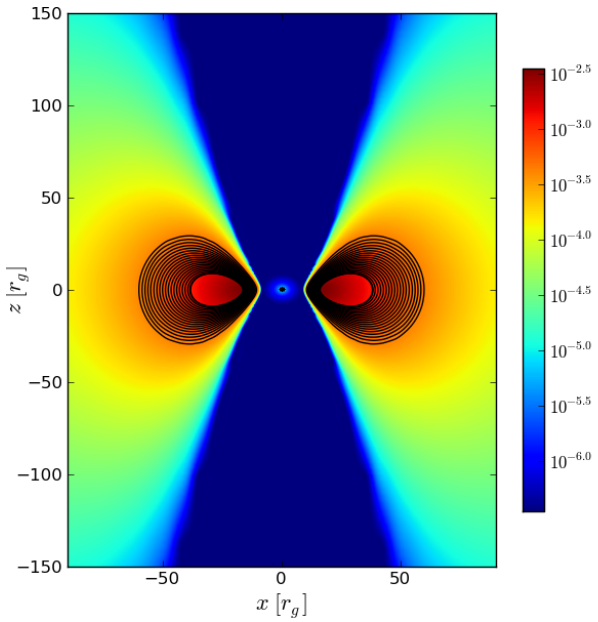

Figure 17. The fiducial model's initial ($t = 0$) state consists of a weakly magnetized geometrically thick torus around a spinning ($a/M = 0.9375$) BH. ρ_0 is shown as color with legend. Black lines show $\underline{A}_\phi$ (integrated over all ϕ) composed of a single set of field line loops with a single polarity.

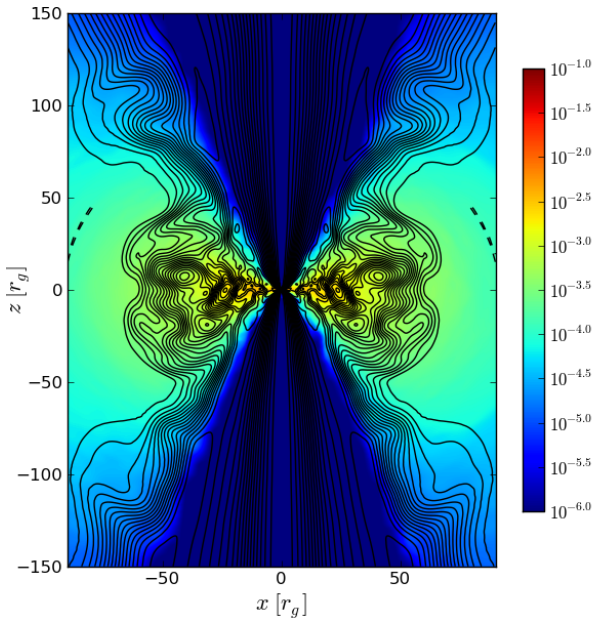

Figure 18. The evolved ($t \approx 5600r_g/c$) state of the fiducial model (otherwise similar to Fig. 17) consists of strongly magnetized gas near the BH that launches a jet.

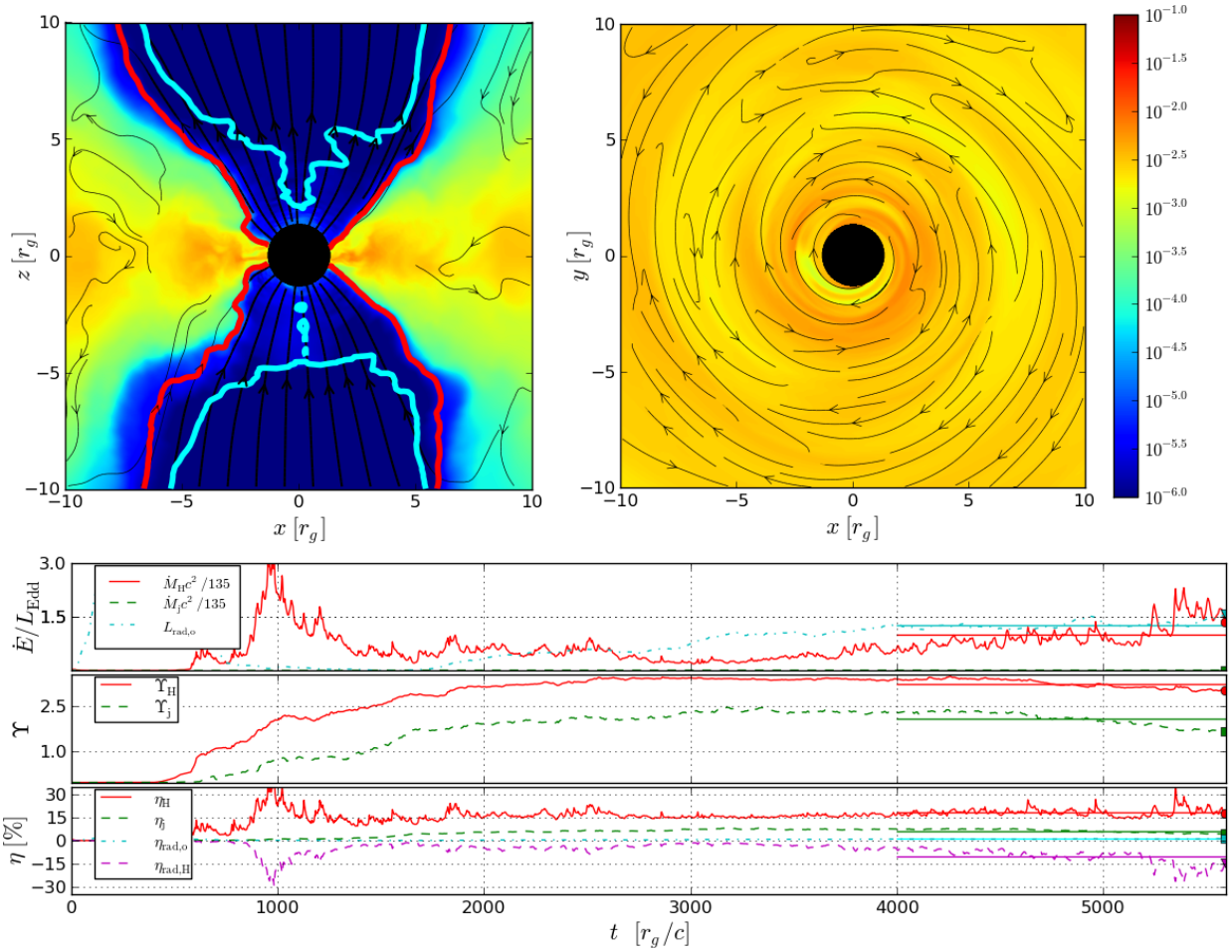

Figure 20. Evolved snapshot (see Supporting Information and this link for the movie) of the fiducial model at $t \approx 5600 r_g/c$ showing log of rest-mass density in color (see legend on right) in both the $z-x$ plane at $y=0$ (top-left panel) and $y-x$ plane at $z=0$ (top-right panel). Black lines trace field lines, where thicker black lines show where field is lightly mass-loaded. In the top-left panel, the thick red line corresponds to where $b^2/\rho_0 = 1$, while the thick cyan line corresponds to where the optical depth (away from the polar axis) reaches unity (i.e. $\tau_a = 1$ as given by Eq. (139)). The bottom panel has 3 subpanels. The top subpanel shows $\dot{M}_0$ through the BH ($\dot{M}_{\rm H}$), out in the jet ($\dot{M}_{\rm j}$, at $r = 50r_g$), and radiative luminosity ($L_{\rm rad,o}$, from optically thin region at $r = 50r_g$) with legend. All quantities have been normalized by the Eddington luminosity ($L_{\rm Edd}$), where in addition all mass fluxes are normalized by the time-averaged value of $\dot{M}_{\rm H}/L_{\rm Edd} \approx 135$ so that all quantities can be shown on a single panel. The middle subpanel shows Υ for similar conditions. The bottom subpanel shows the efficiency (η) for similar conditions, where $\eta_{\rm rad,o}$ corresponds to the radiative efficiency from the radiation escaping out of the optically thin regions at large radii, while $\eta_{\rm rad,H}$ is for the radiation that ends up trapped and absorbed by the black hole (so it is negative). Horizontal solid lines of the same colors show the averages over the averaging period, while square/triangle/circle tickers are placed at the given time and values. In summary, for super-Eddington accretion at $\dot{M}c^2/L_{\rm Edd} \sim 100$, the total BH efficiency is moderate at $\eta \sim 20\%$, while the radiative efficiency is quite low at $\eta_{\rm rad,o} \sim 1\%$.

The α-viscosity parameter holds steady at about $\alpha_b \sim 0.5$. $\Upsilon \sim 3$ in the pure inflow ($u_r < 0$ only) available at large radii. The value is similar to that on the black hole. This can be understood by looking at the value of $r_{\Psi_a} \sim r_{\rm H}$ by $t \sim 3000$, which shows that most of the magnetic flux that is available is already on the horizon. This is also evident by looking at $\Psi_{\rm H}(t)/\Psi_a(t)$ (i.e. ratio of time-dependent fluxes) corresponding to [the flux on the hole] per unit [flux on the hole plus available of the same polarity just beyond the hole]. $\Psi_{\rm H}(t)/\Psi_a(t) \sim 1$ is reached by $t \sim 3000$, after which there is no more magnetic flux available to feed the black hole or disk. Finally, $|\Psi_{\rm tH}(t)/\Phi_{\rm H}(t)| \sim 1$, which shows that the horizon's field is dipolar ($l \approx 1$).

6.10 Time-Averaged Radial (r) Dependence

Fig. 22 shows the time-averaged densities, 3-velocities, and comoving 4-fields vs. radius using a density-weighted average to focus on heavy disk material. The solution is in inflow equilibrium (3 inflow times; see section 6.7.7) only out to $r \sim 14r_g$. Beyond the BH, the rest-mass density is quite flat as expected for a flow supported by radiation pressure at super-Eddington accretion rates. The rotational velocity is very close to Keplerian.

The GR viscosity estimate for v_r denoted $v_{\rm visc}$ (see above Eq. (138)) overestimates the simulation v_r when using the α-viscosity with total pressure, where a better match is obtained using only magnetic pressure. If we set $\alpha(\theta^d)^2 \rightarrow 0.003$ at all radii, then $|v_{\rm visc}| \approx |v_r|$ outside the ISCO and inside the inflow equilibrium region.

Fig. 23 shows the fluxes (see section 6.7.5) vs. radius as well as the field line angular rotation frequency $\Omega_{\rm F}$ (using various def-

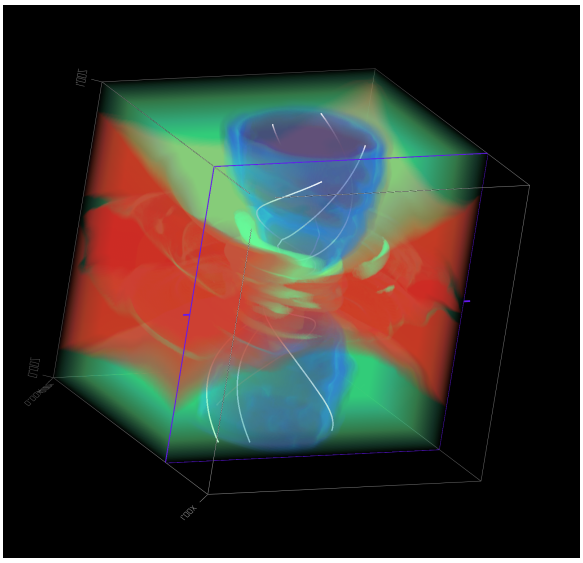

Figure 19. Three-dimensional rendering (with clipping near middle, shown as purple square) of three main structural elements of the flow from near the black hole out to $\pm 10 r_g$ in each direction of a Cartesian box for the evolved ($t \approx 5600 r_g/c$) state of the fiducial model. Figure shows the radiation-dominated disk component (orange-red volume rendering), the hot disk-corona gas component (green-cyan volume rendering) that comes into equipartition with the radiation energy density outside the disk, and the relativistic highly magnetized jet component (blue-purple volume rendering with white magnetic field lines).

initions defined in section 6.7.6). These quantities are associated with conserved quantities such that ratios of total fluxes would be constant along flow-field lines in stationary ideal MHD. The total fluxes are constant out to $r \sim 14 r_g$, the inflow equilibrium radius for this short duration simulations. Also shown are the components (inflow, jet, magnetized wind, and entire wind) of the mass and energy flow. The mass inflow and outflow at large radii somewhat follow power-laws after sufficient averaging over turbulent eddies. The jet efficiency is order 10% and is constant at large radii.

Power-law fits over the outer-radial domain (including the region not actually in inflow equilibrium) for the mass flow rates are $\dot{M}_0 \propto r^{1.7}$ for the inflow and entire wind, $\dot{M}_0 \propto r^{0.9}$ for the jet. A fit of $\dot{M}_0 \propto r^{0.4}$ is shown for the magnetized wind, but the radial range in equilibrium is not sufficient to check this fit.

The quantity $\dot{M}_{\rm w,unb,tavg}$ is the true unbound wind computed from time-ϕ-averaged versions of fluxes and the time-ϕ averaged value of $u_t(\rho_0 + e_{\rm gas} + p_{\rm gas})/\rho_0 < -1$, such that any circulation is eliminated from the calculation (Narayan et al. 2012; Sądowski et al. 2013b). This includes both ingoing and outgoing flow (i.e. we don't choose the flow component based upon u^r), so this gives a conservative estimate of how much (if any) net unbound mass is flowing out. This calculation works because most of the disk starts (and remains) thermally bound. A fit of $\dot{M}_{\rm w,unb,tavg} \propto r^1$ is shown for the true unbound wind, but the radial range in equilibrium is not sufficient to check this fit.

The field line angular frequency $\Omega_{\rm F} \sim \Omega_{\rm H}/4$ (as in BZ77's paraboloidal model) in the disk+corona+wind (i.e. "fdc" averaging, for full flow except the highly-magnetized jet).

Fig. 24 shows the time-averages for the disk's geometric half-angular thickness (θ^d), the thermal half-thickness (θ^t, using the density-weighted average), flow interface angular locations, resolution of the MRI wavelength, and approximate α viscosity pa-

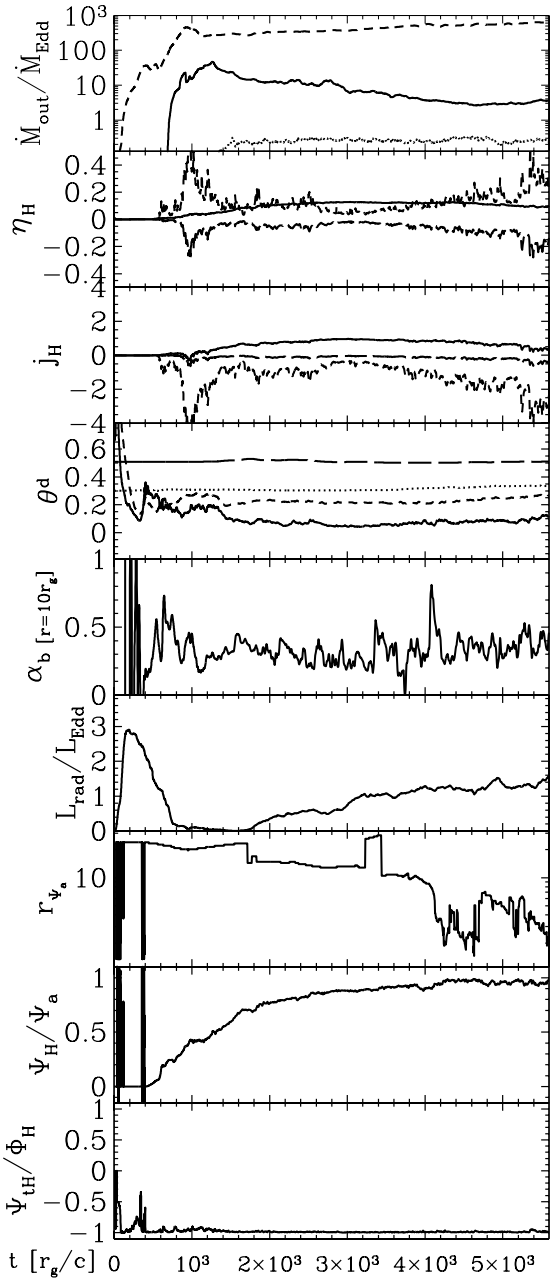

Figure 21. Quantities vs. time. Top Panel: $\dot{M}_{\rm out}$ for magnetized wind ($\dot{M}_{\rm mw,o}$, solid line, and mostly middle line), entire wind ($\dot{M}_{\rm w,o}$, short-dashed line, and upper-most line), and jet ($\dot{M}_{\rm j}$, dotted line, and lowest line). Next Panel: BH efficiency ($\eta_{\rm H}$) for EM (solid line, mostly middle line), MAKE (short-dashed line, mostly upper line) terms, RAD (long-dashed line, lower line) terms. Next Panel: BH specific angular momentum ($j_{\rm H}$) for EM (solid line, upper line), MAKE (short-dashed line, lower line) terms, and RAD (long-dashed line, middle line) terms. Next Panel: θ^d at $r = \{r_{\rm H}/r_g, 5, 20, 100\} r_g$ with, respectively, lines: {solid, short-dashed, dotted, long dashed} corresponding to the lowest to upper-most lines. Next panel: α_b at $r = 10 r_g$. Next Panel: Radiative luminosity at large distances ($L_{\rm rad,o}$, at $r = 50 r_g$ from the optically thin region). Next Panel: r_{Ψ_a} for the radius out to where there is the same magnetic polarity as on the hole (solid line). Next panel: Magnetic flux on the BH per unit flux available in the flow with the same polarity: $\Psi_{\rm H}(t)/\Psi_a(t)$. Bottom panel: $\Psi_{\rm tH}(t)/\Phi_{\rm H}(t) \sim 1/l$, for l mode of vector spherical harmonic multipole expansion of $\underline{A}_\phi$. In summary, the flow has reached a quasi-steady-state at late times. While the black hole efficiency is order 20%, the radiation emitted at large radius from the optically thin region only has an efficiency of order 1% and is of order the Eddington luminosity.

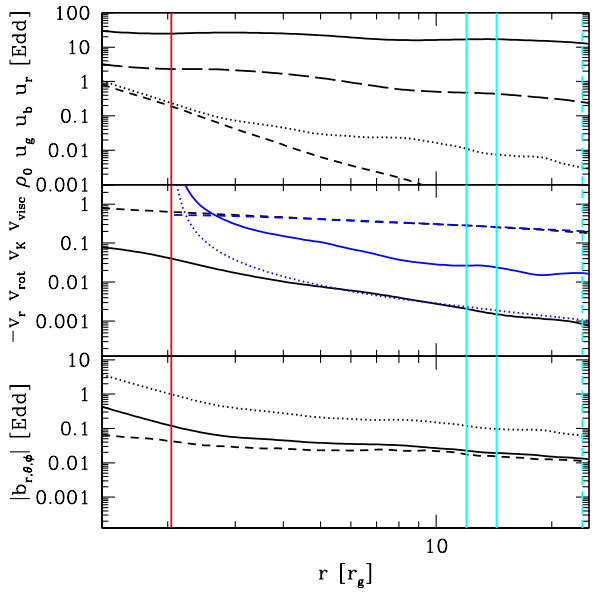

Figure 22. The time-angle-averaged densities, 3-velocities, and 4-field strengths using a density-weighted average. Top panel shows rest-mass density (ρ_0) as black solid line, internal energy density ($e_{\rm gas}$) as black short-dashed line, magnetic energy density (u_b) as black dotted line, and radiation energy density in the radiation frame ($\bar{E}$) as long-dashed line. Middle panel shows negative radial velocity ($-v_r$) as black solid line, rotational velocity ($v_{\rm rot}$) as black short-dashed line, Keplerian rotational velocity ($v_{\rm K}$) as blue short-dashed line, and α-viscosity theory radial velocity ($v_{\rm visc}$) when using $p_{\rm b}$ in denominator for $\alpha = \alpha_b$ (blue solid line) and when choosing a fixed $\alpha(\theta^d)^2 = 0.003$ (blue dotted line). Bottom panel shows comoving 4-field spatial components with r, θ, and ϕ components shows as solid, short-dashed, and dotted black lines, respectively. The vertical red line marks the ISCO. Vertical solid cyan lines show range from $r = 12r_g$ to 3 inflow times. The short-dashed vertical cyan line marks a single inflow time. In summary, the flow near the black hole has a flat rest-mass density profile, and the magnetic energy density and radiation energy density dominate the internal energy density. Also, the rotational velocity is very close to Keplerian.

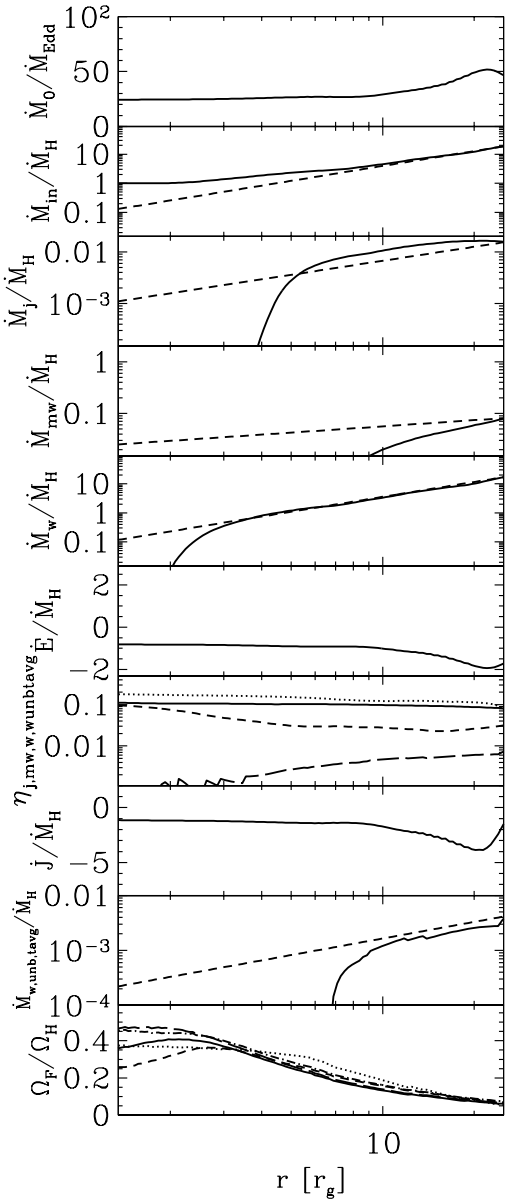

Figure 23. The time-averaged angle-integrated fluxes. From top to bottom, panels are: Total mass accretion rate ($\dot{M}_0$), inflow rate ($\dot{M}_{\rm in}$), jet outflow rate ($\dot{M}_{\rm j}$), magnetized wind outflow rate ($\dot{M}_{\rm mw}$), entire wind outflow rate ($\dot{M}_{\rm w}$), total specific energy accretion rate ($\dot{E}/\dot{M}_{\rm H}$), efficiency for the jet (solid line) magnetized wind (short-dashed line) and wind (dotted line) and true unbound wind (long-dashed line, lowest line), total specific angular momentum accretion rate ($\jmath = \dot{J}/\dot{M}_{\rm H}$), true unbound wind mass outflow rate $\dot{M}_{\rm w,unb,tavg}$ (solid line) and its power-law fit with power-law index 1.0 (short-dashed line), and field line angular rotation frequency per unit BH angular frequency ($\Omega_{\rm F}/\Omega_{\rm H}$) for time-averaged versions of $\Omega_{\rm F}^d$ (solid line), $\Omega_{\rm F}^c$ (short-dashed line), $\Omega_{\rm F}^e$ (dotted line), $|\Omega_{\rm F}^d|$ (long-dashed line), and $|\Omega_{\rm F}^c|$ (dot-short-dashed line). These $\Omega_{\rm F}$ are averaged within the disk+corona part of the flow. Power-law fits for mass inflow and outflow rates are shown as short-dashed lines. In summary, inflow equilibrium is achieved out to $r \sim 14r_g$, and there is a small true net mass outflow of unbound material.

rameter. The disk-corona and corona-jet interfaces trace the path of the well-collimated jet out to large radii. The $Q_{\theta,\rm MRI} \gtrsim 6$ and $Q_{\phi,\rm MRI} \gtrsim 10$ as required to marginally resolve the MRI (Sano et al. 2004). The value of $S_{d,\rm MRI} \sim 4$, indicating that the magnetic field has not reached the saturated state where a magnetically arrested disk (MAD) or magnetically choked accretion flow (MCAF, that occurs at high spin) would form.

6.11 Time-Averaged Angular (θ) Dependence

Fig. 25 is similar to Fig. 22 but for quantities vs. θ at four different radii. The time-averaged density is flatter than a Gaussian distribution. The figure also shows that the total pressure is roughly constant with angle as dominated by the radiation pressure.

Fig. 26 shows the horizon's values of quantities related to the BZ effect (Blandford & Znajek 1977). The simulation's fluxes are computed via Eq. (119). The "full BZ-type EM formula" referred to in the figure uses the EM energy flux computed from equation 33 in McKinney & Gammie (2004), which only assumes stationarity and axisymmetry (rather than also small spin in BZ77) and uses the simulation's $\Omega_{\rm F}(\theta)$ and $\underline{B}^r(\theta)$ on the horizon. This figure shows that most of the horizon is highly magnetized due to accretion occurring through a magnetically compressed inflow.

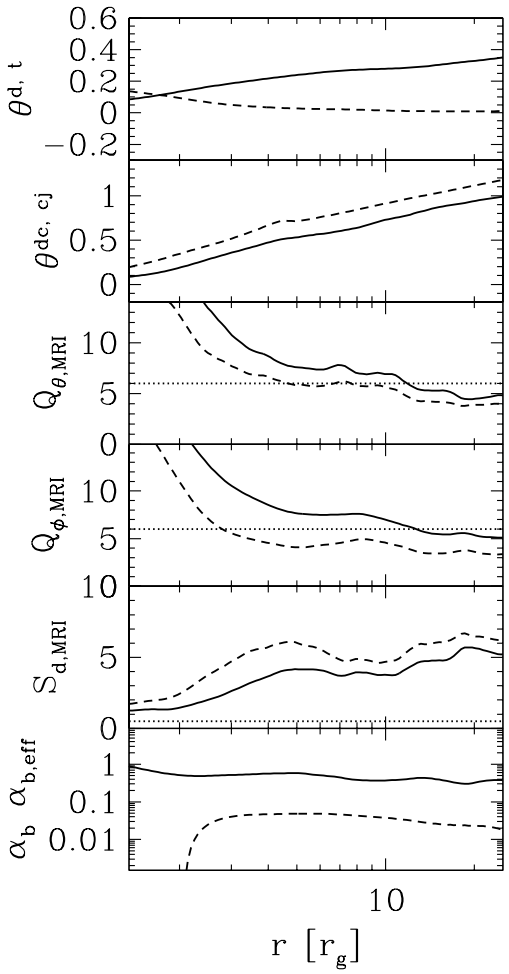

Figure 24. Other time-angle-averaged quantities. From top to bottom, panels are: density half-angular thickness (θ^d, solid line) and thermal half-angular thickness (θ^t, short-dashed line), disk-corona interface angle (θ^{dc}, solid line) and corona-jet interface angle (θ^{cj}, short-dashed line), number of cells per fastest growing MRI wavelength ($Q_{\theta,\rm MRI}$, solid line ; $Q_{\theta,\rm weak,MRI}$, short-dashed line) with $Q_{\theta,\rm MRI} = 6$ shown as dotted line above where the vertical (θ) MRI is resolved, number of cells per fastest growing MRI wavelength ($Q_{\phi,\rm MRI}$, solid line ; $Q_{\phi,\rm weak,MRI}$, short-dashed line) with $Q_{\phi,\rm MRI} = 6$ shown as dotted line above where the azimuthal (ϕ) MRI is resolved, number of fastest growing MRI wavelengths across the full disk thickness ($S_{d,\rm MRI}$, solid line ; $S_{d,\rm weak,MRI}$, short-dashed line) with $S_{d,\rm MRI} = 1/2$ shown as dotted line below where the MRI is suppressed, and viscosity parameter (α_b, solid line ; $\alpha_{b,\rm eff}$, short-dashed line). In summary, the linear MRI is active and numerically marginally resolved.

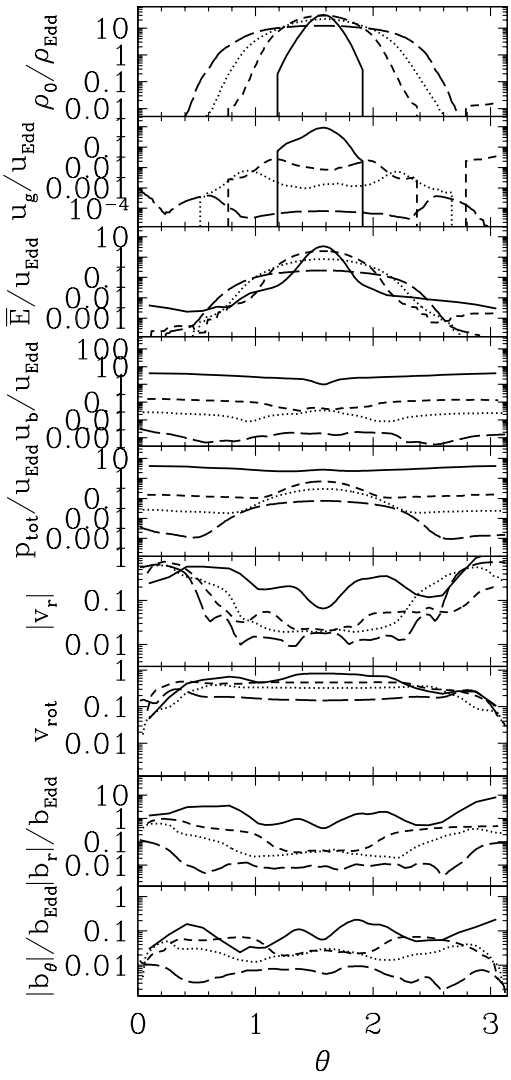

Figure 25. Similar quantities as in Fig. 22, except plotted vs. θ at $r = \{r_{\rm H}/r_g, 4, 8, 30\}r_g$ (respectively: solid, short-dashed, dotted, and long dashed lines). If numerical density floors were activated at some space-time point, then $\rho_0 = e_{\rm gas} = 0$ was set there. In summary, the disk is broader than Gaussian and is supported by radiation pressure.

The agreement between the simulations and the BZ picture is excellent for the highly magnetized regions, where roughly $\Omega_{\rm F} \sim \Omega_{\rm H}/2$ near the disk-jet interface (here, $\Omega_{\rm F}$ is the time-average of Eq. (136)). While the simulation is roughly consistent with BZ's paraboloidal solution, the equatorial $\Omega_{\rm F}$ is somewhat suppressed due to the disk inflow, as expected (Gammie 1999). Also, near the polar axes, $\Omega_{\rm F}$ is affected by ideal MHD effects and numerical floor mass injection.

6.12 Space-Time Averaged Fluxes, Viscosities, Numerical Quality Factors

Lastly, we show a summary of diagnostics computed as described in section 6.7, and a similar set of diagnostics were computed in McKinney et al. (2012) and can be compared. The diagnostics were taken from time-averages computed between $t = 4000M$ and $5596M$ for this model we identify as A0.94BpN100L20, which identifies it as having spin (A) approximately $a/M \approx 0.94$, a magnetic field (B) that is poloidal (p) and the field is normalized (N) to have $\beta_{\rm min} \approx 100$ at $t = 0$, and the mass accretion rate per unit Eddington (L) is of order $\dot{M}_0/\dot{M}_{\rm Edd} \sim 20$ (the $\dot{M}_0/L_{\rm Edd} \sim 100$). Quantities labelled i for "inner" are measured at $r \sim 10r_g$, while quantities labelled o are measured at $r \sim 50r_g$. The mass inflow ($\dot{M}_{\rm in,o}$) and total wind mass flow ($\dot{M}_{\rm mw,o}$) measurements at the outer radius are not in equilibrium due to the short duration of the sim-

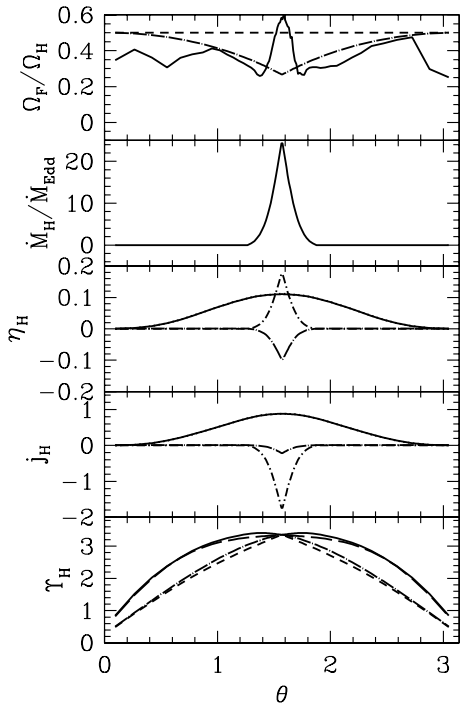

Figure 26. Time-ϕ-averaged quantities and flux integrals on the horizon as a function of θ. From top to bottom: 1) Field line rotational angular frequency (Ω_F/Ω_H) for simulation (solid line), 1st-order-in-spin accurate value for monopolar (short-dashed line) and paraboloidal (dot-long-dashed line) BZ solutions ; 2) Rest-mass flux ($\dot{M}_H$) ; 3) Electromagnetic (EM, solid line) and matter (MA, dot-short-dashed line, which rises at equator) efficiency and radiation (RAD, dot-long-dashed line, which drops at equator) efficiency (η_H), along with the full BZ-type EM formula without any renormalization (dotted line, which overlaps very well with solid line) ; 4) Electromagnetic (EM, solid line) and matter (MA, dot-short-dashed line, which drops the most at equator) and radiation (RAD, dot-long-dashed line, which drops the least at equator) specific angular momentum flux ($j_H = \dot{J}_H/\dot{M}_H$), along with the full BZ-type EM formula without any renormalization (dotted line, which overlaps very well with solid line); 5) Gammie parameter (Υ_H) for the simulation (solid line), and the BZ model for the cases: 0th-order-in-spin accurate monopolar field (short-dashed line), 0th-order-in-spin accurate paraboloidal field (dot-long-dashed line), and 2nd-order-in-spin accurate monopolar field (long-dashed line). These BZ versions are normalized so total magnetic flux is the same as in the simulation. Notice how the 2nd-order-in-spin accurate monopolar BZ model fits the simulation result quite well. For the last 3 panels, the divisor is (implicitly) $\dot{M}_H$ that has been fully angle-integrated to a single value. So, η_H, j_H, and Υ_H show the angular dependence of $\dot{E}_H$, $\dot{J}_H$, and Ψ_H, respectively. In summary, the agreement between the simulation and the BZ picture is excellent.

ulation, but we keep the measurements for comparison with tables in McKinney et al. (2012).

For the rest-mass fluxes and ejection rates, the rest-mass fluxes are normalized by $\dot{M}_{\rm Edd}$, while the luminosity in the last column is normalized by $\dot{L}_{\rm Edd}$. These values show that the mass flow is super-Eddington, while the radiative output at large distances (here measured at $r = 50r_g$ in the optically thin region) is only near the Eddington rate.

The wind quantities like $\dot{M}_{\rm mw,i}$ (magnetized unbound wind at $r = 10r_g$), $\dot{M}_{\rm mw,o}$ (magnetized unbound wind at $r = 50r_g$), $\dot{M}_{\rm w,i}$ (total wind at $r = 10r_g$), and $\dot{M}_{\rm w,o}$ (total wind at $r = 50r_g$) were computed based upon measurements of fluxes at each instant having $u^r > 0$. However, the flow circulates and much of that motion cancels-out.

So we also compute the quantities like $\dot{M}_{\rm w,unb,tavg,i}$ (unbound wind at $r = 10r_g$) and $\dot{M}_{\rm w,unb,tavg,o}$ (unbound wind at $r = 50r_g$) based upon first time-ϕ-averaging the fluxes, time-ϕ-averaging $u_t(\rho_0+e_{\rm gas}+p_{\rm gas})/\rho_0$ that is < -1 for an unbound flow, and only *then* computing the spatial integral. This avoids including any short-period circulations and measures the residual outflow from the accretion flow (Narayan et al. 2012; Sądowski et al. 2013b). This includes both ingoing and outgoing flow (i.e. we don't choose the flow component based upon u^r), so this gives a fairly conservative estimate of how much (if any) net unbound mass is flowing out. Not using $u^r > 0$ as a restriction works because most of the disk starts (and remains) thermally bound and so the disk does not contribute to this measurement.

The true unbound wind at $r \sim 50r_g$ is $\dot{M}_{\rm w,unb,tavg,o} \sim 0.1\dot{M}_{\rm Edd}$, which is only about 1% of the mass that reaches the black hole. This is probably an upper limit (see Narayan et al. 2012; Sądowski et al. 2013b).

The efficiency values show that the black hole has an efficiency of about $\eta_H \approx 19\%$, which is quite similar to expected for standard thin disk theory given by the Novikov-Thorne value of $\eta_{\rm NT} \approx 18\%$. Unlike the MCAF models in McKinney et al. (2012) and MAD models in Tchekhovskoy et al. (2011, 2012a,b), these models involve weak magnetic fields similar to many other models published in the literature (McKinney & Blandford 2009). Interestingly, in this simulation, the MA term dominates the EM term for energy extraction from the BH, with the radiation absorbed contributing to a significant decrement in efficiency. About half of the EM energy extracted goes into the EM jet driven by the BZ mechanism. The true unbound wind has an efficiency of $\eta_{\rm w,unb,tavg,o} \sim 1\%$ by $r \sim 50r_g$, which is as efficient as the radiation (but this is probably an upper limit, see Narayan et al. 2012; Sądowski et al. 2013b).

The spin-up rates show that the black hole is spinning down, but only mildly so compared to the extreme spin down occurring in MAD/MCAF simulations (McKinney et al. 2012). The spin-down is dominated by the EM, MA, PA terms with negligible contribution by the radiation absorbed by the BH. The spin-down for the spin chosen is comparable to those for weakly magnetized disks (McKinney & Gammie 2004; Gammie et al. 2004), which have a spin-equilibrium value of $a/M \sim 0.9$. So we would expect a similar spin-equilibrium for our models.

The α viscosities are order $\alpha \sim 0.03$, which is lower than those in MADs/MCAFs where $\alpha \sim 1$. The quality factors show that our simulation marginally resolves the turbulent structures in the disk in all directions and for both the mass and field components. The simulation marginally resolves the MRI with $Q_{\rm MRI} \gtrsim 10$. The field has not reached the MAD/MCAF state as indicated by $S_{d,\rm MRI} \gtrsim 1$ such that there are still about 4 full wavelengths that can fit vertically inside the disk. This is also consistent with the relatively low $\Upsilon \sim 3$. Even though the field is ordered and dipolar ($|\Phi_H/\Psi_{fH}| \sim 1$), it is relatively weak due to the limited available magnetic flux in the initial conditions (as often used by many researchers).

7 SUMMARY

We have incorporated the M1 closure for radiation into the code HARMRAD. Several radiative tests demonstrate the accuracy, robustness, and speed of the method in both the optically thin and thick regimes in both unmagnetized and magnetized regimes.

We also performed a relatively low-resolution short-duration

Table 5. Physical Diagnostics and Numerical Quality Measurements for model A0.94BpN100L20

Rest-Mass Accretion/Ejection Rates and Radiative Luminosity per unit Eddington

$\dot{M}_{\rm H}$	$\dot{M}_{\rm in,i}-\dot{M}_{\rm H}$	$\dot{M}_{\rm in,o}-\dot{M}_{\rm H}$	$\dot{M}_{\rm j}$	$\dot{M}_{\rm mw,i}$	$\dot{M}_{\rm mw,o}$	$\dot{M}_{\rm w,i}$	$\dot{M}_{\rm w,o}$	$\dot{M}_{\rm w,unb,tavg,i}$	$\dot{M}_{\rm w,unb,tavg,o}$	$L_{\rm rad,o}$
24	85	440	0.26	0.48	3.1	80	560	0.03	0.11	1.3

Percent Energy Efficiency: BH, Jet, Winds, Radiation, and NT

$\eta_{\rm H}$	$\eta_{\rm H}^{\rm EM}$	$\eta_{\rm H}^{\rm MAKE}$	$\eta_{\rm H}^{\rm PAKE}$	$\eta_{\rm H}^{\rm EN}$	$\eta_{\rm H}^{\rm RAD}$	$\eta_{\rm j}$	$\eta_{j}^{\rm EM}$	$\eta_{\rm j}^{\rm MAKE}$	$\eta_{\rm mw,o}$	$\eta_{\rm w,o}$	$\eta_{\rm w,unb,tavg,o}$	$\eta_{\rm o}^{\rm RAD}$	$\eta_{\rm NT}$
18.5	11	18	22.4	-4.42	-10.5	6.3	5.38	0.92	5.14	1.97	0.82	0.94	17.9

Spin-Up Parameter: BH, Jet, Winds, Radiation, and NT

$s_{\rm H}$	$s_{\rm H}^{\rm EM}$	$s_{\rm H}^{\rm MA}$	$s_{\rm H}^{\rm PA}$	$s_{\rm H}^{\rm EN}$	$s_{\rm H}^{\rm RAD}$	$s_{\rm j}$	$s_{j}^{\rm EM}$	$s_{\rm j}^{\rm MA}$	$s_{\rm mw,o}$	$s_{\rm w,o}$	$s_{\rm w,unb,tavg,o}$	$s_{\rm o}^{\rm RAD}$	$s_{\rm NT}$
-0.162	-0.448	0.255	0.245	0.01	0.031	-2.17	-0.269	-1.91	-2.35	-26.8	-0.2	0.016	0.411

Viscosities, Grid Cells per Correlation lengths and MRI Wavelengths, MRI Wavelengths per full Disk Height, and Radii for MRI Suppression

$\alpha_{b,\rm eff}$	$\alpha_{b,\rm eff2}$	α_{b}	$\alpha_{b,\rm M2}$	$\alpha_{b,\rm mag}$	$Q_{n,\rm cor,}$ $_{\{\rho_0,b^2\}}$	$Q_{l,\rm cor,}$ $_{\{\rho_0,b^2\}}$	$Q_{m,\rm cor,}$ $_{\{\rho_0,b^2\}}$	$Q_{\theta,\rm MRI,\{i,o\}}$	$Q_{\phi,\rm MRI,\{i,o\}}$	$S_{\rm d,MRI,\{i,o\}}$	$r_{\{S_{\rm d},S_{\rm d,weak}\}}$ $_{\rm MRI=1/2}$
0.029	0.029	0.42	0.28	0.28	21, 16	14, 10	8, 6	6, 6	12, 12	4, 4	-, -

Absolute Magnetic Flux per unit: Rest-Mass Fluxes, Initial Magnetic Fluxes, Available Magnetic Fluxes, and BH Magnetic Flux

$\Upsilon_{\rm H}$	$\Upsilon_{\rm in,i}$	$\Upsilon_{\rm in,o}$	$\Upsilon_{\rm j}$	$\Upsilon_{\rm mw,i}$	$\Upsilon_{\rm mw,o}$	$\Upsilon_{\rm w,i}$	$\Upsilon_{\rm w,o}$	$\left\lvert\frac{\Psi_{\rm H}}{\Psi_1(t=0)}\right\rvert$	$\left\lvert\frac{\Psi_{\rm H}}{\Psi_2(t=0)}\right\rvert$	$\left\lvert\frac{\Psi_{\rm H}}{\Psi_3(t=0)}\right\rvert$	$\left\lvert\frac{\Psi_{\rm H}}{\Psi_a}\right\rvert$	$\left\lvert\frac{\Psi_{\rm H}}{\Psi_s}\right\rvert$	$\left\lvert\frac{\Phi_{\rm H}}{\Psi_{\rm fH}}\right\rvert$
3.2	0.47	0.91	2.1	4.3	3.4	1.1	1.7	0.72	0	0	0.96	0.96	1

fully 3D simulation of super-Eddington accretion onto a rotating black hole with spin $a = 0.9375$ with $\dot{M}_0 \sim 100L_{\rm Edd}/c^2 \sim 20\dot{M}_{\rm Edd}$. The magnetic field was chosen to be sub-MAD levels to focus on the effects of radiative physics. The disk is essentially Keplerian, with a substantial negative matter energy flux through the horizon. There is no sign of the global Papaloizou-Pringle instability (Papaloizou & Pringle 1984), as likely due to turbulence (Blaes 1987), but the magneto-rotational instability (Balbus & Hawley 1998) drives turbulent accretion and winds. There is an electromagnetically-driven jet in the polar regions, which we show is powered by the Blandford-Znajek (BZ) mechanism. The radiative luminosity is essentially near Eddington, but both the electromagnetic jet and radiative emission are geometrically beamed in the polar regions, so the isotropic equivalent luminosity for the polar regions is super-Eddington.

As applied to the cosmological growth of black holes, as discussed in the introduction and given by Eq. (3), the fiducial 3D model with $a/M = 0.9375$ has a radiative efficiency of $\eta_{\rm rad} \approx 1\%$ while the accretion efficiency remains high at $\eta_{\rm acc} \approx 20\%$ near Novikov-Thorne values expected for an optically thick geometrically thin disk. Over cosmological times, this allows growth from $M = 10M_\odot$ to arbitrarily high M, which suggests that, even for modestly super-Eddington rates of $\dot{M}_0 \sim 100L_{\rm Edd}/c^2 \sim 20\dot{M}_{\rm Edd}$, the black hole spin does not limit black hole mass growth over cosmological times. In addition, while the spin-up parameter of $s \approx -0.16$ shows the BH of spin $a/M = 0.9375$ will spin down, this rate is similar to obtained in other comparable non-MAD GRMHD simulations (McKinney & Gammie 2004) for which the spin equilibrium is $a/M \sim 0.9$. So we expect the black hole to remain rapidly rotating during this super-Eddington accretion.

These simulations show that the GRRMHD code HARMRAD is capable of accurately simulating optically thick or thin problems, including accretion flows around rotating black holes. However, the adopted M1 closure assumes the radiation is isotropic in a single frame, which limits the ability of the closure to handle general anisotropic radiation distributions. Also, our current M1 scheme is based upon frequency integrated quantities. However, the M1 closure improves upon the flux-limited diffusion approximation. We also include no Componization (Younsi & Wu 2013).

In addition, while the code is stable, accurate, and fast even with our use of the high-resolution PPM scheme, in some cases PPM exhibits non-uniform (due to random grid-scale oscillations) convergence behavior as well as mild noise when the LAXF Riemann solver is used at sharp discontinuities. We plan to continue to improve PPM and the Riemann solve used to keep the high resolution of PPM while avoiding the oscillations and non-uniform convergent behavior. We also plan to explore the full higher-order IMEX methods provided in section 4.1, which are presented for easy implementation into HARM/HARMRAD.

ACKNOWLEDGMENTS

We thank James M. Stone and Omer Blaes for useful discussions. RN and AS were supported in part by NSF grant AST1312651. AT was supported by NASA through the Einstein Fellowship Program, grant PF3-140115. We acknowledge NSF support via XSEDE resources, NICS Kraken and Nautilus under grant numbers TG-PHY120005 (JCM), TG-AST100040 (AT), TG-AST080026N (RN and AS), and NASA support via High-End Computing (HEC) Program through the NASA Advanced Supercomputing (NAS) Division at Ames Research Center (JCM, AS, and RN) that provided access to the Pleiades supercomputer.

SUPPORTING INFORMATION

Additional Supporting Information may be found in the online version of this article: Movie file. Movie of the fiducial model A0.94BpN100L20 showing the animated version of Fig. 20 (see caption alongside movie file for more detail) available at http://www.youtube.com/watch?v=q2DeKxUHae4.

REFERENCES

Abramowicz M., Jaroszynski M., Sikora M., 1978, A&A, 63, 221
Abramowicz M. A., Chen X., Granath M., Lasota J., 1996, ApJ, 471, 762
Abramowicz M. A., Chen X., Kato S., Lasota J., Regev O., 1995, ApJ, 438, L37
Abramowicz M. A., Czerny B., Lasota J. P., Szuszkiewicz E., 1988, ApJ, 332, 646
Anninos P., Fragile P. C., Salmonson J. D., 2005, ApJ, 635, 723
Balbus S. A., Hawley J. F., 1998, Reviews of Modern Physics, 70, 1
Barth A. J., Martini P., Nelson C. H., Ho L. C., 2003, ApJ, 594, L95
Beckwith K., Armitage P. J., Simon J. B., 2011, MNRAS, 416, 361
Beckwith K., Hawley J. F., Krolik J. H., 2008a, ApJ, 678, 1180
Beckwith K., Hawley J. F., Krolik J. H., 2008b, MNRAS, 390, 21
Beckwith K., Hawley J. F., Krolik J. H., 2009, ApJ, 707, 428
Begelman M. C., 2012, MNRAS, 420, 2912
Berti E., Volonteri M., 2008, ApJ, 684, 822
Beskin V., Tchekhovskoy A., 2005, A&A, 433, 619
Blaes O., Hirose S., Krolik J. H., 2007, ApJ, 664, 1057
Blaes O., Krolik J. H., Hirose S., Shabaltas N., 2011, ApJ, 733, 110
Blaes O. M., 1987, MNRAS, 227, 975
Blandford R. D., Begelman M. C., 1999, MNRAS, 303, L1
Blandford R. D., Znajek R. L., 1977, MNRAS, 179, 433
Bloom J. S., Giannios D., Metzger B. D., et al., 2011, Science, 333, 203
Boscarino S., 2011, in American Institute of Physics Conference Series, edited by T. E. Simos, G. Psihoyios, C. Tsitouras, Z. Anastassi, vol. 1389 of American Institute of Physics Conference Series, 1315–1318
Boscarino S., Russo G., 2009, SIAM J. Scientific Computing, 31, 3, 1926
Boscarino S., Russo G., 2013, ArXiv e-prints/1306.4926
Burrows D. N., Kennea J. A., Ghisellini G., et al., 2011, Nature, 476, 421
Cao X., 2011, ApJ, 737, 94
Colella P., Woodward P. R., 1984, Journal of Computational Physics, 54, 174
Collin S., Boisson C., Mouchet M., et al., 2002, A&A, 388, 771
Coughlin E. R., Begelman M. C., 2013, ArXiv e-prints
Davis S. W., Stone J. M., Jiang Y.-F., 2012, ApJS, 199, 9
De Villiers J.-P., Hawley J. F., Krolik J. H., 2003, ApJ, 599, 1238
Del Zanna L., Zanotti O., Bucciantini N., Londrillo P., 2007, A&A, 473, 11
Di Matteo T., Springel V., Hernquist L., 2005, Nature, 433, 604
Dibi S., Drappeau S., Fragile P. C., Markoff S., Dexter J., 2012, arXiv:1206.3976, 3976–3976,
Done C., Gierliński M., Kubota A., 2007, A&AR, 15, 1
Dubroca B., Feugeas J. L., 1999, CRAS, 329, 915
Esin A. A., McClintock J. E., Narayan R., 1997, ApJ, 489, 865
Esin A. A., Narayan R., Cui W., Grove J. E., Zhang S.-N., 1998, ApJ, 505, 854
Fabian A. C., 2012, ARA&A, 50, 455
Fan X., Strauss M. A., Becker R. H., et al., 2006, AJ, 132, 117
Farris B. D., Li T. K., Liu Y. T., Shapiro S. L., 2008, Phys. Rev. D, 78, 4023, 0223.
Fender R., Belloni T., 2004, ARA&A, 42, 317
Fragile P. C., Blaes O. M., Anninos P., Salmonson J. D., 2007, ApJ, 668, 417
Fragile P. C., Gillespie A., Monahan T., Rodriguez M., Anninos P., 2012, ApJS, 201, 9
Fragile P. C., Meier D. L., 2009, ApJ, 693, 771
Frank J., King A., Raine D. J., 2002, Accretion Power in astrophysics, Cambridge Univ. Press
Fryxell B., Olson K., Ricker P., et al., 2000, ApJS, 131, 273
Gammie C. F., 1999, ApJ, 522, L57
Gammie C. F., McKinney J. C., Tóth G., 2003, ApJ, 589, 444
Gammie C. F., Shapiro S. L., McKinney J. C., 2004, ApJ, 602, 312
Ghasemnezhad M., Khajavi M., Abbassi S., 2013, Ap&SS, 346, 341
Giacomazzo B., Rezzolla L., 2006, 464, 429, Audit, E. and & Huynh, P. 2007, *A&A*
Hawley J. F., Balbus S. A., 2002, ApJ, 573, 738
Hawley J. F., Balbus S. A., Stone J. M., 2001, ApJ, 554, L49
Hawley J. F., Krolik J. H., 2001, ApJ, 548, 348
Hawley J. F., Smarr L. L., Wilson J. R., 1984, ApJ, 277, 296
Hayes J. C., Norman M. L., 2003, ApJS, 147, 197
Hirose S., Blaes O., Krolik J. H., 2009a, ApJ, 704, 781
Hirose S., Blaes O., Krolik J. H., 2009b, ApJ, 691, 16
Hirose S., Krolik J. H., Blaes O., 2009, ApJ, 691, 16
Ichimaru S., 1977, ApJ, 214, 840
Igumenshchev I. V., Narayan R., 2002, ApJ, 566, 137
Igumenshchev I. V., Narayan R., Abramowicz M. A., 2003, ApJ, 592, 1042
Jiang Y.-F., Stone J. M., Davis S. W., 2012, ApJS, 199, 14
Jiang Y.-F., Stone J. M., Davis S. W., 2012, ApJS, 199, 14
Jiang Y.-F., Stone J. M., Davis S. W., 2013, ApJ, 778, 65
Kawakatu N., Ohsuga K., 2011, MNRAS, 417, 2562
Kawashima T., Ohsuga K., Mineshige S., et al., 2012, ApJ, 752, 18
Krolik J. H., Hirose S., Blaes O., 2007, ApJ, 664, 1045
Krumholz M. R., Klein R. I., McKee C. F., Bolstad J., 2007, ApJ, 667, 626
Kumar H., 2011, Implicit-explicit Runge-Kutta methods for the two-fluid MHD equations, Tech. Rep. 2011-26, Seminar for Applied Mathematics, ETH Zürich, Switzerland
Levan A. J., Tanvir N. R., Cenko S. B., et al., 2011, Science, 333, 199
Levermore C. D., 1984, J. Quant. Spec. Radiat. Transf., 31, 149
Lightman A. P., Eardley D. M., 1974, ApJ, 187, L1
Machida M., Hayashi M. R., Matsumoto R., 2000, ApJ, 532, L67
Margon B., 1984, ARA&A, 22, 507
Margon B., Ford H. C., Katz J. I., et al., 1979, ApJ, 230, L41
Martí J. M., Müller E., 2003, Living Reviews in Relativity, 6, 7
McClintock J. E., Narayan R., Davis S. W., Gou L., et al., 2011, 28, 4009, Class. Quant. Gravity 1109.
McClintock J. E., Remillard R. A., 2006, Compact Stellar X-ray Sources, eds. W. Lewin & M. van der Klis, Cambridge Univ. Press
McKinney J. C., 2006, MNRAS, 367, 1797
McKinney J. C., Blandford R. D., 2009, MNRAS, 394, L126
McKinney J. C., Gammie C. F., 2004, ApJ, 611, 977
McKinney J. C., Tchekhovskoy A., Blandford R. D., 2012, MNRAS, 423, 3083
Mignone A., McKinney J. C., 2007, MNRAS, 378, 1118
Mihalas D., Mihalas B. W., 1984, New York, Oxford University Press,, (). title. 731 p.
Miller M. C., Colbert E. J. M., 2004, Int. J. Mod. Phys. and D13, 1
Mineshige S., Ohsuga K., Takeuchi S., 2012, in European Physical Journal Web of Conferences, vol. 39 of European Physical Journal Web of Conferences, 6005
Mortlock D. J., et al., 2011, Nature, 474, 616
Mościbrodzka M., Gammie C. F., Dolence J. C., Shiokawa H., 2011, ApJ, 735, 9
Narayan R., Igumenshchev I. V., Abramowicz M. A., 2000, ApJ, 539, 798
Narayan R., SÄ dowski A., Penna R. F., Kulkarni A. K., 2012, MNRAS, 426, 3241
Narayan R., Sadowski A., Penna R. F., Kulkarni A. K., 2012, MNRAS, in press (arXiv:1206.1213)
Narayan R., Yi I., 1994, ApJ, 428, L13
Narayan R., Yi I., 1995, ApJ, 452, 710
Narayan R., Yi I., Mahadevan R., 1995, Nature, 374, 623
Nobili L., Turolla R., Zampieri L., 1991, ApJ, 383, 250
Noble S. C., Gammie C. F., McKinney J. C., et al., 2006, ApJ, 641, 626
Noble S. C., Krolik J. H., Hawley J. F., 2009, ApJ, 692, 411
Noble S. C., Krolik J. H., Hawley J. F., 2010, ApJ, 711, 959

Noble S. C., Krolik J. H., Schnittman J. D., Hawley J. F., 2011a, D. and & Thorne, K. S. 1973, Black Holes (Les Astres Occlus), 343
Noble S. C., Krolik J. H., Schnittman J. D., Hawley J. F., 2011b, ApJ, 743, 115
Novikov I. D., Thorne K. S., 1973, in Black Holes, (Eds C De Witt, B S De Witt) (London: Gordon and Breach, 1973)
Ohsuga K., 2006, ApJ, 640, 923
Ohsuga K., Mineshige S., 2007, ApJ, 670, 1283
Ohsuga K., Mineshige S., 2011, ApJ, 736, 2
Ohsuga K., Mineshige S., Mori M., Umemura M., 2002, ApJ, 574, 315
Ohsuga K., Mineshige S., Mori M., Yoshiaki K., 2009, PASJ, 61, L7
Ohsuga K., Mineshige S., Watarai K.-y., 2003, ApJ, 596, 429
Ohsuga K., Mori M., Nakamoto T., Mineshige S., 2005, ApJ, 628, 368
Page D. N., Thorne K. S., 1974, ApJ, 191, 499
Palenzuela C., Lehner L., Reula O., Rezzolla L., 2009, MNRAS, 394, 1727
Pang B., Pen U.-L., Matzner C. D., Green S. R., Liebendörfer M., 2011, MNRAS, 415, 1228
Papaloizou J. C. B., Pringle J. E., 1984, MNRAS, 208, 721
Pareschi L., Russo G., 2000, Journal of Scientific Computing, 3, 269
Pareschi L., Russo G., 2005, Journal of Scientific Computing, 25, 1-2, 129
Pen U.-L., Matzner C. D., Wong S., 2003, ApJ, 596, L207
Penna R. F., McKinney J. C., Narayan R., et al., 2010, MNRAS, 408, 752
Penna R. F., McKinney J. C., Narayan R., Tchekhovskoy A., Shafee R., McClintock J. E., 2010, MNRAS, 408, 752
Pessah M. E., Psaltis D., 2005, ApJ, 628, 879
Piran T., 1978, ApJ, 221, 652
Popham R., Gammie C. F., 1998, ApJ, 504, 419
Quataert E., Gruzinov A., 2000, ApJ, 539, 809
Remillard R. A., McClintock J. E., 2006, ARAA, 44, 49
Reynolds C. S., Fabian A. C., 2008, ApJ, 675, 1048
Reynolds C. S., Miller M. C., 2009, ApJ, 692, 869
Roedig C., Zanotti O., Alic D., 2012, arXiv:1206.6662
Sądowski A., 2009, ApJS, 183, 171
Sano T., Inutsuka S., Turner N. J., Stone J. M., 2004, ApJ, 605, 321
Sądowski A., Narayan R., McKinney J. C., Tchekhovskoy A., 2013a, ArXiv e-prints
Sądowski A., Narayan R., Penna R., Zhu Y., 2013b, MNRAS, 436, 3856
Sądowski A., Narayan R., Tchekhovskoy A., Zhu Y., 2013c, MNRAS, 429, 3533
Schnittman J. D., Krolik J. H., Hawley J. F., 2006, ApJ, 651, 1031
Shafee R., McKinney J. C., Narayan R., Tchekhovskoy A., et al., 2008, ApJ, 687, L25
Shakura N. I., Sunyaev R. A., 1973, A&A, 24, 337
Shapiro S. L., Teukolsky S. A., 1983, Black holes, white dwarfs, and neutron stars: The physics of compact objects
Shcherbakov R. V., Penna R. F., McKinney J. C., 2010, arXiv:1007.4832
Shibata M., Sekiguchi Y., 2012, Progress of Theoretical Physics, 127, 535
Shiokawa H., Dolence J. C., Gammie C. F., Noble S. C., 2012, ApJ, 744, 187
Shu C.-W., Osher S., 1988, Journal of Computational Physics, 77, 439
Sorathia K. A., Reynolds C. S., Armitage P. J., 2010, ApJ, 712, 1241
Sorathia K. A., Reynolds C. S., Stone J. M., Beckwith K., 2012, ApJ, 749, 189
Springel V., Di Matteo T., Hernquist L., 2005, MNRAS, 361, 776
Stone J. M., Pringle J. E., 2001, MNRAS, 322, 461
Straub O., Bursa M., Sadowski A., Steiner J. F., et al., 2011, å533, A67
Takahashi H. R., Ohsuga K., 2013, ApJ, 772, 127
Takahashi H. R., Ohsuga K., Sekiguchi Y., Inoue T., Tomida K., 2013, ApJ, 764, 122
Takeuchi S., Mineshige S., Ohsuga K., 2009, PASJ, 61, 783
Takeuchi S., Ohsuga K., Mineshige S., 2010, PASJ, 62, L43
Takeuchi S., Ohsuga K., Mineshige S., 2013, PASJ, 65, 88
Tchekhovskoy A., McKinney J. C., 2012, MNRAS, 423, L55
Tchekhovskoy A., McKinney J. C., Narayan R., 2007, MNRAS, 379, 469
Tchekhovskoy A., McKinney J. C., Narayan R., 2012a, JPCS, 372, 1, 012040
Tchekhovskoy A., McKinney J. C., Narayan R., 2012b, Journal of Physics Conference Series, 372, 1, 012040
Tchekhovskoy A., Metzger B. D., Giannios D., Kelley L. Z., 2013, MNRAS, doi:10.1093/mnras/stt2085 (ArXiv:1301.1982)
Tchekhovskoy A., Narayan R., McKinney J. C., 2011, MNRAS, 418, L79
Thorne K. S., 1974, ApJ, 191, 507
Trenchea C., 2014, Appl. Math. Lett., 27, 97
Turner N. J., Stone J. M., Krolik J. H., Sano T., 2003, ApJ, 593, 992
Vitello P., 1984, ApJ, 284, 394
Volonteri M., Madau P., Quataert E., Rees M. J., 2005, ApJ, 620, 69
Watarai K., Mizuno T., Mineshige S., 2001, ApJ, 549, L77-L77.
Watarai K.-Y., Ohsuga K., Takahashi R., Fukue J., 2005, PASJ, 57, 513
Willott C. J., Delorme P., Reylé C., et al., 2010, AJ, 139, 906
Willott C. J., Percival W. J., McLure R. J., et al., 2005, ApJ, 626, 657
Yang X.-H., Yuan F., Ohsuga K., Bu D.-F., 2013, ArXiv e-prints
Younsi Z., Wu K., 2013, MNRAS, 433, 1054
Yuan F., Quataert E., Narayan R., 2003, ApJ, 598, 301
Zanotti O., Roedig C., Rezzolla L., Del Zanna L., 2011, MNRAS, 417, 2899
Zauderer B. A., Berger E., Soderberg A. M., et al., 2011, Nature, 476, 425